

박사학위논문

햅틱 증강현실:
실제 물체의 강도 변경

전석희(全碩熙)

전자컴퓨터공학부(컴퓨터공학 전공)

포항공과대학교 대학원

2010

햅틱 증강현실:
실제 물체의 강도 변경

**Haptic Augmented Reality:
Modulating Real Object Stiffness**

Haptic Augmented Reality: Modulating Real Object Stiffness

by

Seokhee Jeon

Division of Electrical and Computer Engineering
(Computer Science and Engineering)
POHANG UNIVERSITY OF SCIENCE AND TECHNOLOGY

A thesis submitted to the faculty of Pohang University of Science and Technology in partial fulfillment of the requirements for the degree of Doctor of Philosophy in the Division of Electrical and Computer Engineering (Computer Science and Engineering)

Pohang, Korea

June 21, 2010

Approved by


Seungmoon Choi, Major Advisor

햅틱 증강현실: 실제 물체의 강도 변경

전석희

위 논문은 포항공대 대학원 박사 학위 논문으로 학위 논문 심사
위원회를 통과하였음을 인정합니다.

2010년 6월 21일

학위논문 심사위원회 위원장

위 원

위 원

위 원

위 원

최승문 (인)

김정현 (인)

이승용 (인)

한준희 (인)

유지환 (인)



DECE 20032007 전 석 희, Seokhee Jeon, Haptic Augmented Reality: Modulating Real Object Stiffness. 햅틱 증강현실: 실제 물체의 강도 변경, Division of Electrical and Computer Engineering (Computer Science and Engineering), 2010, 126 P, Advisor: Seungmoon Choi. Text in English

Abstract

Haptic Augmented Reality (AR) enables a user to feel a real environment augmented with synthetic haptic stimuli. For instance, medical students can palpate a virtual tumor inside a real mannequin using a haptic AR system to practice cancer detection. To realize such functionalities, we need to alter the haptic attributes, such as stiffness and friction of a real object by means of virtual haptic feedback. Despite its potential, attempts to develop systematic and general computational algorithms for such functionalities of haptic AR have been scanty. This dissertation aims at developing a systematic and sophisticated methodology for haptic AR, i.e., a “haptic AR toolKit.” Towards this goal, the author begins with establishing a new taxonomy for haptic AR based on a composite visuo-haptic reality-virtuality continuum extended from the conventional continuum for vision. Previous studies related to haptic AR are reviewed and classified using the composite continuum, and associated research issues are discussed. Second, the feasibility of haptically modulating the feel of a real object with the aid of virtual force feedback is investigated, with the stiffness as a goal haptic property. A commercial haptic interface is extended with a force sensor, and all required algorithms for contact detection, stiffness modulation, and force control are developed for 1D interaction of tapping. Their individual performances are thoroughly evaluated. The resulting haptic AR system is also assessed in a psychophysical experiment, demonstrating its competent perceptual performance for stiffness modulation. Third, the initial system is extended so that a user can interact with a real object in any 3D exploratory patterns while perceiving its augmented stiffness. A series of new algorithms

for 3D interaction of tapping, stroking, and contour following are developed for contact detection, deformation estimation, force rendering, and force control. A particular focus has been on minimizing the amount of preprocessing such as geometry modeling while preserving reasonable perceptual performance. The physical and perceptual performances of algorithms are also thoroughly evaluated with real samples. Our haptic AR system can provide convincing stiffness modulation for real objects of relatively homogeneous deformation properties. Fourth, to demonstrate the potential of haptic AR, a case study is presented for physical training of breast cancer palpation. A real breast model made of soft silicone is augmented with a virtual tumor rendered inside. Haptic stimuli for the virtual tumor are generated based on a contact dynamics model identified via real measurements. A subjective evaluation confirmed the realism and fidelity of our palpation system. Finally, the haptic AR system is combined to the state-of-the-art visual AR framework, enabling the augmentation of both the real visual and haptic environment seamlessly with virtual information.

Contents

1	Introduction	1
1.1	Augmented Reality for Haptics	1
1.2	Research Goal	2
1.3	Contributions	2
1.4	Organization	3
2	Haptic Augmented Reality	5
2.1	Concept and Taxonomy	5
2.2	Classification and Review of Related Work	7
2.2.1	Haptic Reality	7
2.2.2	Haptic Virtuality	8
2.2.3	Haptic Mixed Reality	9
2.3	Remarks	10
3	Stiffness Modulation: 1D Interaction	13
3.1	Interaction Modeling	13
3.2	Contact Detection	15
3.2.1	Algorithm	16
3.2.2	Performance Evaluation	17

3.3	Force Control	22
3.3.1	Algorithm	23
3.3.2	Performance Evaluation	25
3.4	Psychophysical Experiment	28
3.4.1	Methods	28
3.4.2	Results	33
3.4.3	Discussion	34
3.5	General Discussion	37
4	Stiffness Modulation: 3D Interaction	39
4.1	Interaction Modeling	40
4.2	Performance Requirements	42
4.3	Contact Detection	44
4.3.1	Algorithm	44
4.3.2	Performance Evaluation	46
4.4	Estimation of Deformation Direction	48
4.4.1	Friction Model Acquisition	49
4.4.2	Rendering	56
4.4.3	Performance Evaluation	58
4.5	Estimation of Deformation Displacement	60
4.5.1	Contact Dynamics Model Acquisition	62
4.5.2	Rendering	63
4.5.3	Performance Evaluation	64
4.6	Force Control	67
4.6.1	Algorithm	67
4.6.2	Performance Evaluation	69
4.7	Psychophysical Experiment	73
4.7.1	Methods	73
4.7.2	Results	77

4.7.3	Discussion	79
4.8	General Discussion	82
5	A Case Study: Haptic Simulation of Breast Cancer Palpation	86
5.1	Interaction Model	87
5.2	Preprocessing Tumor Response	89
5.3	Rendering	90
5.4	Physical Performance Evaluation	92
5.5	Assessing Realism	94
5.5.1	Methods	94
5.5.2	Results	97
5.5.3	Discussion	98
5.6	General Discussion	99
6	Visuo-Haptic Augmented Reality	101
6.1	Visuo-Haptic AR System at ETH	101
6.2	System Integration	103
6.3	Example of Breast Cancer Palpation	104
6.4	Discussion	107
7	Conclusions	108
	한글 요약문	110
	Bibliography	112

List of Figures

2.1	Reality-virtuality continuum for augmented reality.	6
3.1	Definitions of forces and displacement for stiffness modulation.	15
3.2	PHANToM premium instrumented with a 3D force/torque sensor for haptic AR.	16
3.3	Response characteristics of the four real objects.	19
3.4	False alarm rate and time delay of contact detection measured for various thresholds.	20
3.5	Measured variables for contact detection.	21
3.6	Contact detection delays measured with $\epsilon_f = 0.015$ N. The sampling rate for contact detection was 1 kHz.	22
3.7	Histogram of contact velocities (mean=416.2 mm/s and median=372.3 mm/s).	23
3.8	Feasible stiffness ranges obtained using (3.8) with $k(t) = 1.0$ N/mm. Note that the range of Ω includes those of PHANToM 1.0 and 1.5, and the range of PHANToM 1.5 high-force model also includes those of PHAN- ToM 1.0 and 1.5, and Ω . Regions above 15 N/mm are not shown for space.	25

3.9	Displacement-force curves of stiffness modulation. The original stiffness of real objects (the slope of the grey dashed curves) was modulated to have desired stiffness (the slope of the colored solid curves). Note that the non-linear visco-elastic responses of real samples were changed to follow linear elastic models used in our algorithm.	26
3.10	Ranges of stiffness values stably modulated in our haptic AR system.	27
3.11	Experimental environment. The blurred scene inside the white paper box is for illustration, and was not seen by the subjects in the experiment.	29
3.12	Results of the psychophysical experiment averaged across the subjects. (a) PSEs. (b) Differences between the PSEs and the desired stiffness values of the reference stimuli computed from the data in (a) for better visibility. The difference thresholds taken from [39] are also shown in (b). Each experimental condition is denoted by combining the kind of a real object and the desired stiffness value for stiffness modulation used in the condition.	34
3.13	The force command and the actual force generated by the PHANToM 1.0. A user pressed a virtual wall for the measurement.	35
4.1	Definitions of variables for 3D stiffness modulation.	41
4.2	PHANToM augmented for 3D stiffness modulation.	45
4.3	Four real objects used in the experiment.	47
4.4	Distributions of contact detection delays. The small squares represent the averages.	47
4.5	Ball bearing tool tip.	50
4.6	Identification results of the ball bearing friction. (a) Identified friction parameters for ten real objects. The objects are sorted in the decreasing order of stiffness. (b) Comparison of the measured and estimated frictions for rubber mat 1.	52
4.7	Aluminum rod tool tip.	53

4.8	Identification results of the friction between solid rod tool tip and the foam ball.	57
4.9	Distributions of the deformation direction estimation errors for each object using the ball bearing tool tip. Small squares represent the mean values. . .	58
4.10	Estimated and true deformation directions collected from the foam ball using the ball bearing tool tip.	59
4.11	Distributions of the deformation direction estimation errors using the solid rod tool tip.	61
4.12	Measured and estimated displacement-force curves of the four real objects. Insets are magnified graphs around zero displacement for a detailed view. .	64
4.13	Distribution of the deformation displacement estimation errors for each object and for each deformation direction estimation method.	66
4.14	Tool tip positions and object surfaces reconstructed using the estimated displacements. Object surfaces without deformation obtained in preprocessing are also shown in the dashed lines.	67
4.15	Displacement-force curves. Displacements for plotting are derived from the displacement estimation algorithm.	70
4.16	Ranges of stiffness values stably modulated in our 3D stiffness modulation system.	71
4.17	Experimental environment. The blurred scene inside the paper box is for illustration, and was not seen by the subjects in the experiment. The haptic interface point and the wire-frame models for the two objects were visualized in 3D on the monitor in order to guide the subject's interaction. They were disappeared when the tool is in contact with one of the two objects. . .	74
4.18	Sample results of the foam ball - 0.3 N/mm condition.	78

4.19 Experimental results averaged across the subjects. (a) PSEs for the four conditions. (b) Differences between the PSEs in (a) and the stiffness values of the reference stimuli. The dotted-lines in (b) represents difference thresholds taken from [39]. Each experimental condition is denoted by combining the kind of a real object and the desired stiffness value for stiffness modulation used in the condition. 79

4.20 An example showing the effect of underestimated or overestimated dynamics model on the rendered stiffness. 81

4.21 The displacement-force curves for measured values and estimated values. 82

5.1 System configuration. 88

5.2 Definition of variables. 89

5.3 Hardware configuration. 90

5.4 Displacement-force curves at the user’s hand. Curves were measured by vertically pressing the hard-tumor-embedded breast model (upper row) and the soft-tumor-embedded breast model (lower row). The pressing locations also varied by the closest surface point from the tumor (left column), 10 mm left from the tumor (middle column), and 20 mm left from the tumor (right column). In each graph, red solid-curve represents data measured from the breast model augmented with a virtual tumor, and the black dotted-curves from the breast with real tumor model. 93

5.5 Experimental environment. The blurred paper box is for illustration, and the subject could not see the scene inside during the experiment. To guide the subject’s interaction, the haptic interface point and the 2D circles locating the two breast models were shown in the monitor. 95

5.6 Similarity scores averaged across the subjects. The error bars represent the standard errors. The shades of the bars indicate the result of the Student-Newman-Keuls grouping test. Bars with the same shade were grouped together. 97

5.7	The time taken to find tumor for each tumor presenting method. The error bars represent the standard errors.	98
6.1	System configuration of ETH's visuo-haptic framework.	102
6.2	Haptic system for the haptic augmentation.	103
6.3	Terms for tumor visualization.	105
6.4	Visualizing tumor movement. The image sequence is directly displayed through the head-mounted display. Two images in a row are for stereoscopic vision.	106

List of Tables

2.1	Computational procedures of visual and haptic AR.	12
-----	---	----

Chapter 1

Introduction

1.1 Augmented Reality for Haptics

Augmented reality (AR) provides the mixed sensations of real and virtual objects to a user, thereby transforming a real space to a semi-virtual space. The current technology for visual AR is relatively mature, and has been applied to practical applications including surgical training, industrial manufacturing, and entertainment [4, 109, 28]. Another emerging area in AR is haptic AR, where the user can touch a real object, a virtual object, or a real object augmented with virtual touch. For example, suppose that a user is holding a pen-shaped “magic” tool in the hand. With the tool, the user can touch and explore a virtual vase overlaid on a real table. In addition, a user can draw a picture on the table with an augmented feel of using a paint brush on a smooth piece of paper, or using a marker on a stiff white board. Besides, medical students can palpate a virtual tumor inside a real mannequin using a haptic AR system to practice cancer detection. Creating such haptic illusions belongs to the realm of haptic AR. AR with both sensory modalities, visuo-haptic AR, can create simulations of great realism, immersion, and presence, which is not easily realized by a pure virtual environment.

Owing to the enormous potentials of haptic AR, it has received increasing attention in the haptics and AR community. Most of previous studies on haptic AR have showed interests in using real props in a visually mixed environment, or creating purely virtual haptic objects

embedded in an real environment (see Chapter 2). In this dissertation, the author moves on one step further, by demonstrating that the feel of a real object can be modulated by force feedback of a haptic interface in a systematic manner. Mixing real haptic stimuli with virtual haptic stimuli adequately allows to make a soft object feel harder, or a rough surface feel smoother, similarly to changing a yellow real tennis ball to a white augmented base ball in visual AR. Even though such functionality for haptic AR requires a unique methodology quite different from that of virtual haptic rendering, relatively a small amount of studies have been devoted to it (see Chapter 2).

1.2 Research Goal

The author speculates that one of the most necessary capabilities for a haptic AR system is general and systematic methods for modulating haptic properties of a real object with the aid of a sensor and haptic interface, similarly to changing the color of a real object in visual AR. A software package analogous to the ARToolKit for visual AR [60] is essential in order for haptic AR to fully realize its potential in various applications, and the author believes that this will enable the haptic illusions introduced in Section 1.1. This dissertation focuses on how to modulate the haptic properties of a real object with the aid of a force-feedback haptic interface and what the user perceive from such a haptically augmented object.

1.3 Contributions

The contribution of the work can be summarized as follows:

- Clarification of the research field of haptic AR
 - Establishment of a new taxonomy for haptic AR based on a composite visuo-haptic reality-virtuality continuum.
 - Review and classification of previous studies related to haptic AR using the new taxonomy.
 - Discussion of associated research issues.

- Proof-of-concept of haptic AR - The modulation of real object stiffness in 1D interactions
 - Development of all required algorithms for contact detection, stiffness modulation, and force control.
 - Evaluation of the physical and perceptual performance of the algorithms.
- Extension of the initial work - Stiffness modulation in 3D interactions
 - Development of all required algorithms for contact detection, deformation direction estimation, deformation displacement estimation, and force control.
 - Physical and perceptual evaluation of the algorithms.
- Application of haptic AR to medical training.
 - Effective physical simulation of a breast with a tumor, and physical and perceptual evaluation.
- Integration of haptic AR into a visuo-haptic AR framework.

1.4 Organization

The author's research for the haptic AR has begun with clarifying the research field and establishing a new taxonomy for haptic AR using a *composite visuo-haptic reality-virtuality continuum* extended from Milgram's continuum for visual AR [82] (Chapter 2). A number of studies related to haptic AR are reviewed and classified based on the composite continuum, and associated research issues are elucidated. In particular, the survey showed the lack of fundamental knowledge on augmenting the haptic attributes of a real object with the aid of a force-feedback haptic interface, which is analogous to augmenting the color of a real object using a Head-Mounted Display (HMD) in visual AR. Such functionality is required to implement the latter example (paint brush and tumor palpation) described in Section 1.1.

Second, the feasibility of modulating the feel of a real object by virtual force feedback is demonstrated, with the stiffness as a goal haptic property (Chapter 3). Complete algorithms

for the stiffness modulation including interaction modeling, contact detection between the real object and the device tool, and stiffness control were proposed for 1D interaction. The whole haptic AR system was evaluated in a psychophysical experiment, showing competent performance for stiffness augmentation. To the author's knowledge, this is among the first efforts in haptic AR for systematic augmentation of real object attributes with virtual force. In addition, several important research issues identified during the feasibility study are presented.

Third, the proof-of-concept system was extended to a 3D stiffness modulation that allows for arbitrary exploration patterns such as tapping, stroking, and contour following (Chapter 4). With the system for 3D interaction, a user can perceive the shape of a real object with altered stiffness, which is the most fundamental requirement for practical applications such as the example of a paint brush. Besides, this extension is a prerequisite for the modulation of other haptic attributes including friction and texture. Effective algorithms are proposed and thoroughly evaluated for physical and perceptual performance. A particular focus has been on minimizing the need of prior knowledge and preprocessing for the haptic properties and geometric information of real objects, while maintaining convincing perceptual quality. This aspect is in agreement with the general advantages of AR; unlike a VR system, an AR system usually does not require the full model of an entire environment.

Fourth, the potential of haptic AR is demonstrated by developing a practical application in medical training area, i.e., physical training system for breast cancer palpation (Chapter 5). A real silicone breast model is augmented with a virtual tumor rendered inside. Haptic stimuli for the virtual tumor are generated based on a contact dynamics model identified via real measurements, without the need of geometric information on the breast. In addition, a subjective evaluation confirmed the realism and fidelity of our palpation system.

In the final chapter, the haptic AR system is combined to the state-of-the-art visual AR framework, enabling the augmentation of both the real visual and haptic environment seamlessly with virtual information.

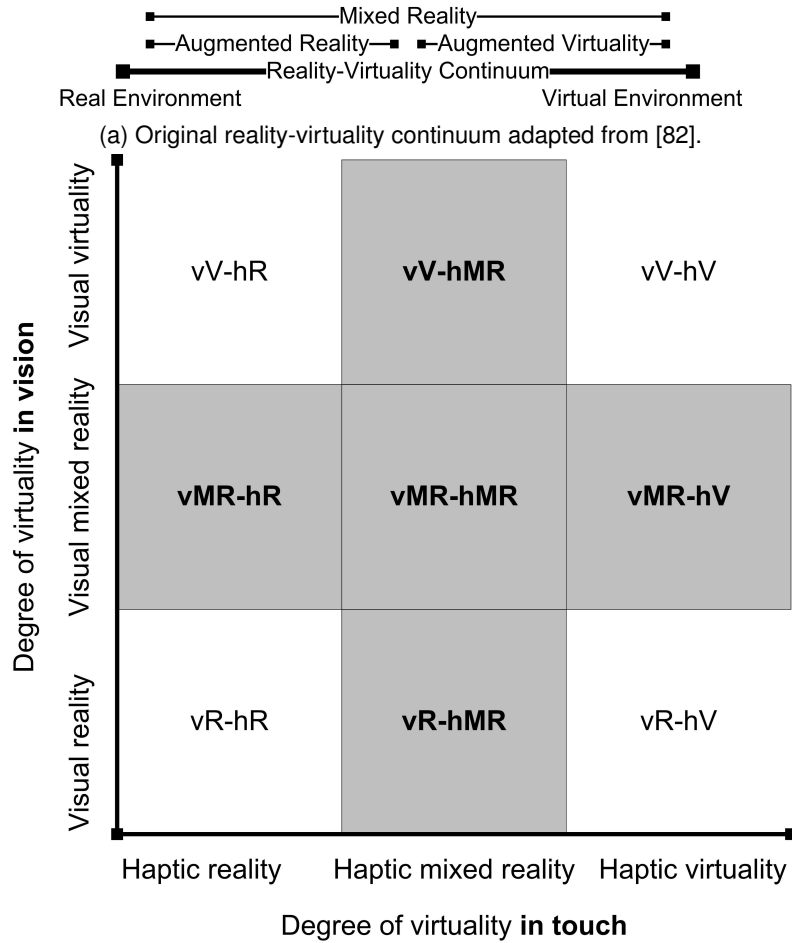
Chapter 2

Haptic Augmented Reality

2.1 Concept and Taxonomy

About a decade ago, concepts associated with AR, or more generally, Mixed Reality (MR) were defined by [82] using the reality-virtuality continuum shown in Fig. 2.1a. The continuum includes all possible combinations of purely real and virtual environments, with the intermediate area corresponding to MR. Whether an environment is closer to reality or virtuality depends on the amount of knowledge that the computer needs to manage for the environment; the more knowledge required, the closer to virtuality. This criterion allows MR to be further classified into augmented reality (e.g., the heads-up display in an aircraft cockpit) and augmented virtuality (e.g., a computer game employing a virtual dancer with the face image of a famous actress). We, however, note that the current literature does not strictly discriminate the two terms, and uses AR and MR interchangeably.

Extending the concept, we can define a similar reality-virtuality continuum for the sense of touch and construct a visuo-haptic reality-virtuality continuum by compositing the two unimodal continua as in Fig. 2.1b. This continuum can be valuable for building the taxonomy of haptic MR. In Fig. 2.1b, the whole visuo-haptic continuum is classified into nine categories, and each category is named in an abbreviated form. The shaded regions belong to the realm of mixed reality. In what follows, the author reviews the concepts and instances associated with each category, with more attention to those of MR. Note that the continuum



(b) Extension of (a) to include the sense of touch. Shaded areas correspond to the realm of mixed reality.

Fig. 2.1 Reality-virtuality continuum for augmented reality.

for touch includes all kinds of haptic feedback and does not depend on the specific types of haptic sensations (e.g., kinesthetic, tactile, or thermal) or interaction paradigms (e.g., tool-mediated or bare-handed).

2.2 Classification and Review of Related Work

2.2.1 Haptic Reality

In the composite continuum, the left column has the three categories of *haptic reality*: vR-hR, vMR-hR, and vV-hR, where the corresponding environments provide only real haptic sensations. Among them, the simplest category is vR-hR, which represents purely real environments without any synthetic stimuli. The other end, vV-hR, refers to the conventional visual virtual environments with real touch, e.g., using a tangible prop to interact with virtual objects. Environments between the two ends belong to vMR-hR wherein a user sees mixed objects but still touches real objects. A typical example is the so-called tangible AR that has been actively studied in the visual AR community. In tangible AR, a real prop held in the hand is usually used as a tangible interface for visually mixed environments (e.g., the MagicBook in [15]), and its haptic property is regarded unimportant for the applications. Another example is the projection augmented model. A computer-generated image is projected on a real physical model to create a realistic-looking object, and the model can be touched by the bare hand (e.g., see [10]). Since the material property (e.g., texture) of the real object may not agree with its visually augmented model, haptic properties are usually incorrectly displayed in this application.

Recently, there have been several attempts to apply vMR-hR into a simulator for medical training [19]. One example is the ProMIS laparoscopic surgery simulator [18], wherein a trainee experiences various laparoscopic procedures using real instruments and real physical anatomic models while annotative visual feedback is overlaid on a real scene. Their system provides ‘real’ haptic feedback, and the trainee can get a more realistic and valid learning experience. An experiment with real surgical students confirmed that the ProMIS simulator could provide better realism than a VR-based simulator in a basic surgery skill task and a suturing task [17]. On the other hand, [69] developed a medical training system for forceps delivery. In their system, a user can practice, using real instruments, the forceps placement and the mechanical effects of it on the fetus, while a virtual fetus is visually overlaid on a real pelvic mock-up. A similar system [94] visualized a virtual uterus and a virtual fetal

head on a real physical mock-up of the female torso, and a trainee interacts with the virtual models with a real forceps. Note that the three systems only provide real force feedback, but the positions of the instruments were tracked to assess the performance of the training.

2.2.2 Haptic Virtuality

The categories in the right column of the composite continuum, vR-hV, vMR-hV, and vV-hV, are for *haptic virtuality*, corresponding to environments with purely virtual haptic sensations only, and have received the most attention from the haptics research community. Robot-assisted motor rehabilitation can be an example of vR-hV where synthetic haptic feedback is provided in a real visual environment, and an interactive virtual simulator is an instance of vV-hV where the sensory information of both modalities is virtual. In the intermediate category, vMR-hV, purely virtual haptic objects are placed in a visually mixed environment, and are rendered using a haptic interface based on the conventional haptic rendering methods for virtual objects. Earlier attempts in this category focused on how to integrate haptic rendering of virtual objects into the existing visual AR framework, and identified precise registration between the haptic and visual coordinate frames as a key issue [101, 1]. For this topic, [61] applied an adaptive low-pass filter to reduce the trembling error of a low-cost vision-based tracker using ARToolkit, and upsampled the tracking data to be used for 1 kHz haptic rendering. [13] and [12] further improved the registration accuracy via intensive calibration of a haptic interface, and optical and landmark trackers. They also explored the potential of visuo-haptic AR technology for medical training with their highly stable and accurate AR system [46]. Their last work improved the fidelity of visual augmentation by including virtual shadow casted on real scene, occlusion of real-virtual object, and stereoscopic display [63]. Another example is [85], which applied the HMD-based visuo-haptic framework to training processes in industry and demonstrated its potential. [81] used the similar system to teach the hand-writing skill to children by providing virtual guidance force, and [89] applied similar system to a dental training simulator incorporated with volumetric tooth models. On the other hand, a half mirror was also popularly used for the visuo-haptic collocation, e.g., ImmersiveTouch [76], Reachin Display

[88], PARIS display [56], and SenseGraphics 3D-IW [93]. The framework was applied to cranial implant design [92] and MR painting application [91]. In medical applications, there have been several attempts to apply vMR-hV systems to minimally invasive surgery procedure (see [67] for overview). Among them, an ongoing project by the ARIS*ER European consortium has been trying to construct an AR-based visual guidance methodology and virtual haptic systems incorporated with radiological data of the patient to improve minimally invasive interventions and surgery [36].

2.2.3 Haptic Mixed Reality

The last categories for *haptic mixed reality*, vR-hMR, vMR-hMR, and vV-hMR, which the rest of this article is concerned with, lie in the middle column of the composite continuum. A common characteristic of haptic MR is that synthetic haptic signals generated from a haptic interface modulate or augment stimuli occurring due to a contact between a real object and a haptic interface tool. The VisHap system [107] can be an instance of vR-hMR that provides mixed haptic sensations in a real environment. In this system, some information about a virtual object (e.g., shape and stiffness) is generated by a haptic device, and other properties (e.g., texture and friction) are supplied by a real prop attached at the end-effector of the device. Other examples in this category are the SmartTool [83] and SmartTouch systems [58]. They utilized various sensors (i.e., optical and electrical conductivity sensors) to capture real signals that could hardly be perceived by the bare hand, and then translated the signal into haptic information and delivered it to the user in order to facilitate certain tasks (e.g., peeling off the white from the yolk in an egg). The MicroTactus system [106] is another example of vR-hMR, which detects and magnifies acceleration signals caused by the interaction of a pen-type probe with a real object. The system was shown to improve the performance of tissue boundary detection in arthroscopic surgical training. A similar pen-type haptic AR system, Ubi-Pen [66], embedded miniaturized texture and vibrotactile displays in the pen, adding realistic tactile feedback for interaction with a touch screen in mobile devices. [65] introduced a simple haptic AR concept for creating realistic visco-elastic feedback, wherein virtual visco-elastic object rendering was assisted by a real base

object that has the similar visco-elastic property to desired object. On the other hand, environments in vV-hMR use synthetic visual stimuli. For example, [16] investigated the utility of haptic MR in a visual virtual environment by adding synthetic force to a passive haptic response for a panel control task. Their results showed that mixed force feedback was better than synthetic force alone in terms of task performance and user preference. In vMR-hMR, both modalities rely on mixed stimuli. [43] installed a vibrator in a real tangible prop to produce virtual vibrotactile sensations in addition to the real haptic information of the prop in a visually mixed environment. They demonstrated that the virtual vibrotactile feedback enhances immersion for an AR-based hand-held game. [8] and [7] introduced a teleoperation framework where force measured at the remote site is presented at the master side with additional virtual force and mixed imagery. In particular, they tried to *modulate* a certain real haptic property with virtual force feedback for a hole patching task and a painting application, in contrast to the most of related studies introduced earlier.

2.3 Remarks

Several remarks need to be made. First, the vast majority of related work, except [83], [16], [65], and [7], has used the term “haptic augmented reality” without distinguishing vMR-hV and hMR, although research issues associated with the two categories are fundamentally different. Second, haptic MR can be further classified as *haptic augmented reality* and *haptic augmented virtuality* based on the same criterion used in visual MR. All of the research instances of hMR introduced earlier correspond to haptic augmented reality, since little knowledge regarding an environment is managed by the computer for haptic augmentation. However, despite its potential, attempts to develop systematic and general computational algorithms for haptic AR have been scanty. An instance of haptic augmented virtuality can be haptic rendering systems that use haptic signals captured from a real object (e.g., see [84, 86, 48]) in addition to virtual object rendering, although such a concept has not been formalized before. Third, although the taxonomy is defined for composite visuo-haptic configurations, a unimodal case (e.g., no haptic or visual feedback) can also be mapped to the corresponding 1D continuum on the axes in Fig. 2.1b. Fourth, [9] also suggested a

simple taxonomy for haptic AR based on the functional aspect of a system. They termed a haptic AR application as “enhanced haptic” if haptic data from an information source are modulated or extrapolated in the application (e.g., providing active haptic guidance to sensorimotor skills; see [8]). In contrast, in applications for “haptic enhancing,” fundamentally new information obtained from sources different from a haptic data source is added to the haptic data (e.g., haptizing non-haptic attributes such as weather variables on a geological map; see [72]). This criterion can be useful for contemplating on the benefits of haptic AR applications.

We further discuss possible application areas that can maximize the advantage of haptic AR. Owing to the basic motivation of AR—augmenting a focused area only while adapting real environment for the surroundings—haptic AR can take advantages of both real and virtual environment. Utilizing a real environment reduces the effort required to construct a target environment. This aspect can be advantageous to the application having frequent environment changes, such as virtual prototyping. Moreover, real environments allows us to efficiently provide high realism and immersion of environments, which is hard to be achieved by current haptics technology for virtual reality. Thus, haptic AR is a perfect candidate for application areas requiring high realism, such as medical training. On the other hand, virtuality makes an environment more flexible. Desired sensory signal can be easily modeled and rendered via software and hardware technology for virtuality. This advantage, together with the advantages of reality, enables haptic AR to be effectively applied to a skill transfer system using virtual haptic guidance.

In addition, the computational procedures and the associated technical issues necessary for visual and haptic AR are summarized and compared in Table 2.1. Moreover, in most AR applications, visual and haptic feedback should be combined, and registration between visual and haptic coordinate frames is an important technical challenge. Interested readers may refer to recent methods for visual-haptic registration (e.g., one in [46]) using a vision-based tracker and careful calibration procedures.

In the rest of this article, we present a haptic AR system that includes all of the computational procedures in Table 2.1 for stiffness modulation.

Table 2.1: Computational procedures of visual and haptic AR.

Procedure	Visual AR	Haptic AR
Sensing a real environment	Captures real information needed for visual augmentation (via camera, range finder, tracker, etc.)	Senses real information needed for haptic augmentation (via position encoder, accelerometer, force sensor, thermometer, etc.)
Constructing stimuli for augmentation	<ol style="list-style-type: none"> 1. Real-virtual registration 2. Overlay of a virtual object on the real scene 	<ol style="list-style-type: none"> 1. Contact detection between the tool (or bare hand) and a real object 2. Modulation of real haptic stimuli
Displaying augmented stimuli	Uses a visual display (head-mounted display, projector, mobile phone, etc.)	Uses a haptic display (force-feedback interface, tactile display, thermal display etc.)

Chapter 3

Stiffness Modulation: 1D Interaction

In this chapter, we present the proof-of-concept study of modulating the haptic attribute of a real object by virtual force feedback, with the stiffness as a goal haptic property. The haptic AR system begins with a measurement of reaction force between a haptic interface tool and a real object in Section 3.1. A contact between the real object and the device tool is then detected using an effective algorithm based on the reaction force in Section 3.2. If a contact is declared, a stiffness control algorithm adapted from robotics is applied for stiffness augmentation in Section 3.3. The whole haptic AR system was evaluated in a psychophysical experiment, showing competent performance for stiffness augmentation in Section 3.4.

3.1 Interaction Modeling

The research towards a general software framework for haptic AR has begun with developing computational algorithms for altering the stiffness of a real object with virtual force generated by a force-feedback haptic interface. Stiffness, the relation between the force applied to an object and the resulting deformation of the object surface, is one of the fundamental properties of any elastic object, and is closely related to the hardness of an object

perceived by a user.

As an initial study, the following three simplifications are made. First, we consider real objects in an elastic state with moderate stiffness. Objects made from plastic (e.g., clay) or brittle materials (e.g., glass) are excluded due to their complicated responses. In addition, objects made from highly stiff materials such as steel cannot be handled since such objects are hardly deformed by the force that current haptic devices can generate. Second, among several sensory cues that affect the hardness perceived by the user, we focus on the modulation of stiffness, a displacement-force relation. Compared to other haptic cues such as tactile contact cues and pressure distribution cues [37], stiffness can be an important sensory cue for objects with moderate stiffness. Third, it is assumed that a haptic interface used for haptic AR is ideally rigid, which allows using simple and intuitive relationships for stiffness augmentation.

The approach for stiffness modulation is derived using notations depicted in Fig. 3.1. The stiffness of a real object being pressed at time t is denoted by $k(t)$. This is the stiffness of the object to be perceived by the user without additional virtual force feedback. The goal is to change the user-perceived stiffness from $k(t)$ to a desired stiffness value, $\tilde{k}(t)$, by providing adequate virtual force to the user's hand. Let forces generated by the haptic device and the hand be $f_d(t)$ and $f_h(t)$, respectively. Due to the two force components, the object surface is deformed by displacement $x_r(t)$ with reaction force $f_r(t)$. Thus, the forces at the tool are in an equilibrium state such that:

$$f_r(t) = k(t)x_r(t) = f_h(t) + f_d(t). \quad (3.1)$$

For the hand to feel the desired stiffness $\tilde{k}(t)$,

$$f_h(t) = \tilde{k}(t)x_r(t). \quad (3.2)$$

Then the force that the device needs to exert is:

$$\tilde{f}_d(t) = f_r(t) - \tilde{k}(t)x_r(t). \quad (3.3)$$

Therefore, the task of stiffness modulation is reduced to controlling the device force $f_d(t)$ to be a desired force $\tilde{f}_d(t)$.

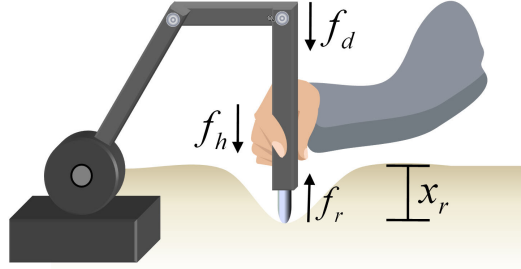


Fig. 3.1 Definitions of forces and displacement for stiffness modulation.

Equation (3.3) indicates that for stiffness modulation, the haptic AR system must be able to sense the reaction force $f_r(t)$ from the surface of a real object (requirement 1) and control the haptic device to generate the desired force $\tilde{f}_d(t)$ (requirement 2). In addition, the system is required to detect the time instant at which the haptic tool touches the object to begin stiffness modulation (requirement 3). For requirement 1, we attached a 3D force/torque sensor (ATI Industrial Automation, Inc.; model Nano 17) at the distal link of a PHANToM premium model (SensAble Technologies, Inc.) to directly measure the reaction force at the tool tip (see Fig. 3.2). Force sensor outputs were sampled via a data acquisition card (National Instruments; model USB 6251) in a PC. A plastic grip was also installed for the operator's convenience. A cylindrical rod of 3-mm diameter with a round tip was fastened to the force sensor, and used as a contact point between the device and objects. The force sensing range was from -35 to 35 N with the resolution of 1.5625 mN along the vertical direction. For requirements 2 and 3, we have adapted the traditional stiffness control algorithm from robotics (see Section 3.3), and developed an efficient contact detection algorithm (see Section 3.2), respectively.

3.2 Contact Detection

To determine when to begin stiffness modulation, the haptic AR system needs an algorithm for detecting a contact between the haptic device tool and a real object. A simple and effective algorithm for contact detection is introduced and its performance is evaluated in this section.

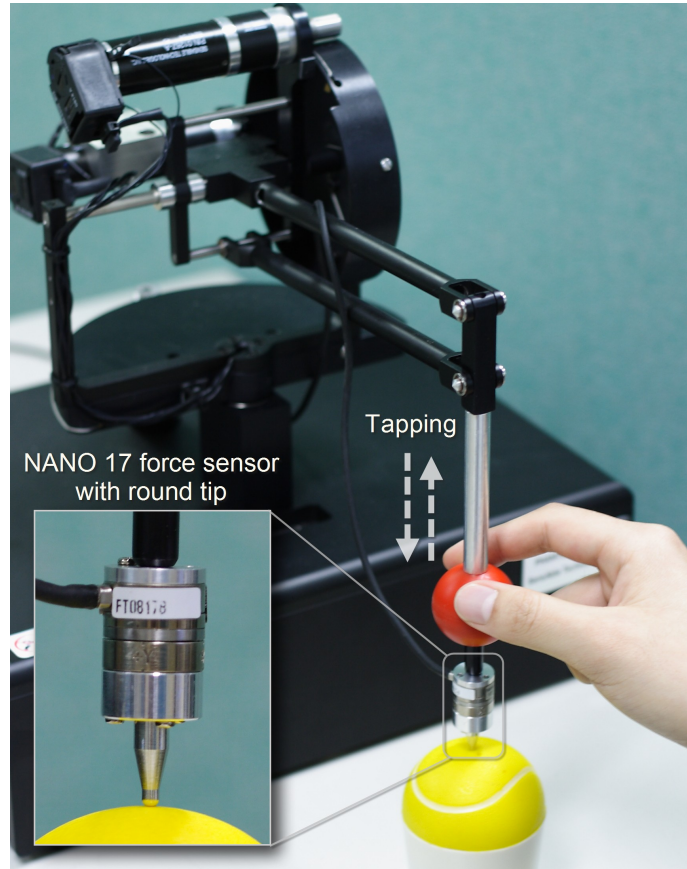


Fig. 3.2 PHANTOM premium instrumented with a 3D force/torque sensor for haptic AR.

3.2.1 Algorithm

A straightforward way for contact detection is to monitor the acceleration of a haptic interface tool held by the user, $a(t)$, and declare that a contact has occurred if $|a(t)| > \epsilon_a$ where ϵ_a is a predetermined threshold. This acceleration-based contact detection can be used for any force-reflecting haptic interface, since all of them have sensors to measure their joint angles (e.g., the optical encoders) and the acceleration of the tool tip can be estimated from joint angle measurements in software. This method, however, has a fundamental drawback. Since acceleration also occurs during free movements of the tool tip, the threshold ϵ_a must be set relatively high in order to avoid false alarms (declaring a contact for the non-contact

movements). Higher thresholds decrease the sensitivity of contact detection, making the time that the algorithm identifies a contact lags behind the actual instant of the contact.

An improved approach is to estimate the response force $f_r(t)$ and examine whether its absolute values show an abrupt rise. Let $f_s(t)$ be a force sensor reading at time t . To obtain $f_r(t)$, the effect of contactor assembly inertia, $f_i(t)$, must be compensated from $f_s(t)$, since a force sensor is usually installed between the last link of a haptic interface and the contactor assembly. Thus,

$$f_r(t) = f_s(t) - f_i(t), \quad (3.4)$$

where given the mass of the tip assembly, m_t (= 9.35 g in our configuration),

$$f_i(t) = m_t a(t). \quad (3.5)$$

We consider that a contact has occurred if $|f_r(t)| > \epsilon_f$, where ϵ_f is a decision threshold that requires careful selection based on the noise level of the force sensor. In this algorithm, a dominant term is $f_s(t)$ that is the force sensor output responding immediately to a contact. The effect of the tip assembly inertia on the reaction force during free motions is compensated by subtracting $f_i(t)$. This allows us to choose ϵ_f such that ϵ_f is robust to the noise of the force sensor only, without paying much attention to false alarms during free movements. Thus, this method includes much less estimation delay than the acceleration-based approach. Note that no prior knowledge of the haptic attributes of real objects and of the geometric relations between real objects and the haptic interface is required in the contact detection algorithm.

3.2.2 Performance Evaluation

Two implementation issues, how to estimate force sensor output $f_s(t)$ and acceleration $a(t)$ in (3.4), can critically affect the performance of contact detection. To obtain an estimate of $f_s(t)$, a low-pass filter of force sensor readings sampled at 1 kHz (= force rendering rate of our haptic AR system) is the usual way in closed-loop force control. This, however, inevitably introduces a delay in filtered force values which adversely affects the delay of contact detection. We selected an alternative of reading force sensor outputs at 10 kHz

and then down-sampling to 1 kHz by averaging ten consecutive samples. This technique effectively suppresses noise in force sensor output as well as substantially decreasing the delay in contact detection. Note that such high-rate sampling was possible owing to the use of the dedicated data acquisition card. To estimate $a(t)$, the double discrete differentiation of digital position measurements is used. Since this method usually results in very noisy estimates, we employed filters in two steps, once to obtain velocity from position data sampled at 1 kHz using the first-order adaptive windowing filter [53], and again to estimate acceleration from the velocities using a second-order Butterworth low-pass filter with 50-Hz cutoff frequency.

For performance evaluation, four real objects were used; sponge block, foam ball, rubber ball, and rubber eraser. They had different stiffness characteristics as shown in Fig. 3.3. The displacement-force curve of each object was obtained in a computer-controlled tapping experiment where the PHANToM applied a contact force to the object from 0 N to 4 N and then to 0 N at a rate of 0.5 N/s and the resulting tip displacements were measured. The figure shows that the rubber eraser exhibited the most linear response, whereas the sponge block shows the most nonlinear response with significant hysteresis. Their representative stiffness values, which were taken at 4 N from the corresponding displacement-force curves, ranged from 0.38 to 2.26 N/mm.

Two measures, the detection accuracy and the time delay of contact detection, were used for performance assessment. If the threshold, ϵ_f , is increased, the probability of false alarms for contact detection is decreased, but the time delay is increased. An optimal ϵ_f was selected as follows. The initial value of ϵ_f was set to the jitter level of the force sensor measured to be 0.01 N. Then, ϵ_f was increased under computer-simulated fast free movements of the PHANToM generated by sinusoidal force commands with 5 Hz frequency and 1 N amplitude and the false alarm rates were recorded. The time delay for contact detection was also measured for each ϵ_f value when a user tapped the foam ball that showed a mild stiffness curve in Fig. 3.3. To pinpoint the exact instant of contact, a very thin copper wire was laid on the surface of the foam ball, and voltage was applied between the tool tip and the wire so that current began to flow on contact. The contact time was precisely measured

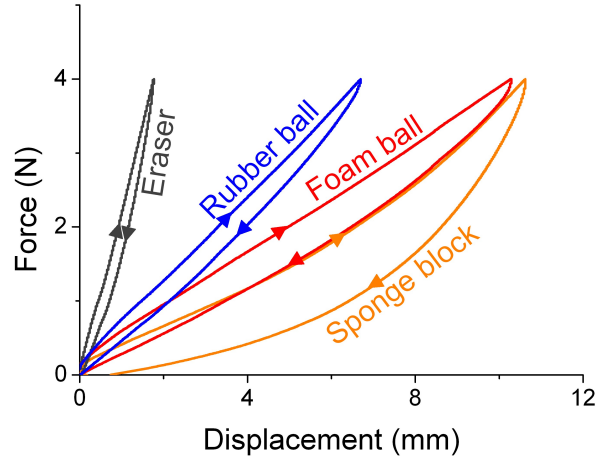


Fig. 3.3 Response characteristics of the four real objects.

by finding a rapid change in the measured current. The results are shown in Fig. 3.4 that clearly illustrates the trade-off between the false alarm rate and the detection delay. Based on these data, we selected $\epsilon_f = 0.015$ N which is the smallest threshold with zero false alarm rate.

Fig. 3.5a shows the examples of $x(t)$, $f_s(t)$, $f_i(t)$, and $f_r(t)$ measured around a contact. When the tool tip was freely moved in space by the user ($0 \text{ ms} \leq t \leq 316 \text{ ms}$ in the figure), the measurements of $f_s(t)$ and $f_i(t)$ were in agreement, making $f_r(t)$ near zero within the jitter level of the force sensor in the loaded condition ($= 0.01$ N). In the figure, we can compare the position of the tool measured with the PHANToM joint encoders, $x(t)$, to the position of the surface of a real object placed at $x = 0$, and find the exact point of a contact at $t = 316$ ms. As expected, $f_s(t)$ and $f_r(t)$ showed rapid increases around the time as magnified in Fig. 3.5b. In the figure, we can confirm that the delay of contact detection was as low as 1 ms.

The criterion for selecting ϵ_f that minimizes the false-alarm rate inevitably lengthens the detection delays. Thus, we further investigated whether the delays were small enough to be insignificant for the perception of modulated stiffness. To collect data, a user tapped on each real object with different contact velocities, and the delay of each tap was calculated

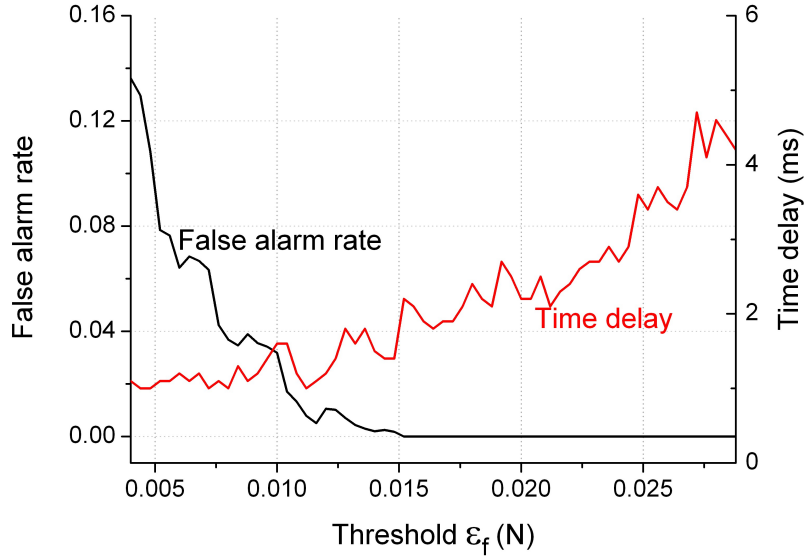
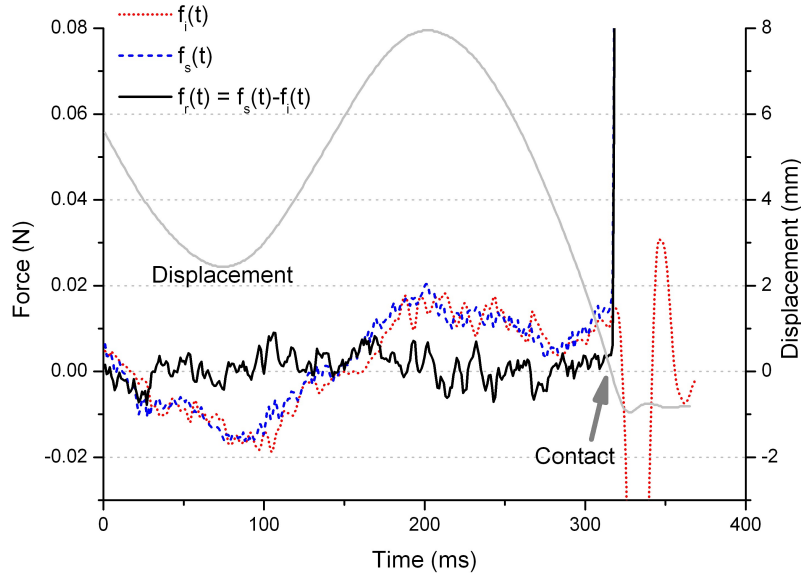


Fig. 3.4 False alarm rate and time delay of contact detection measured for various thresholds.

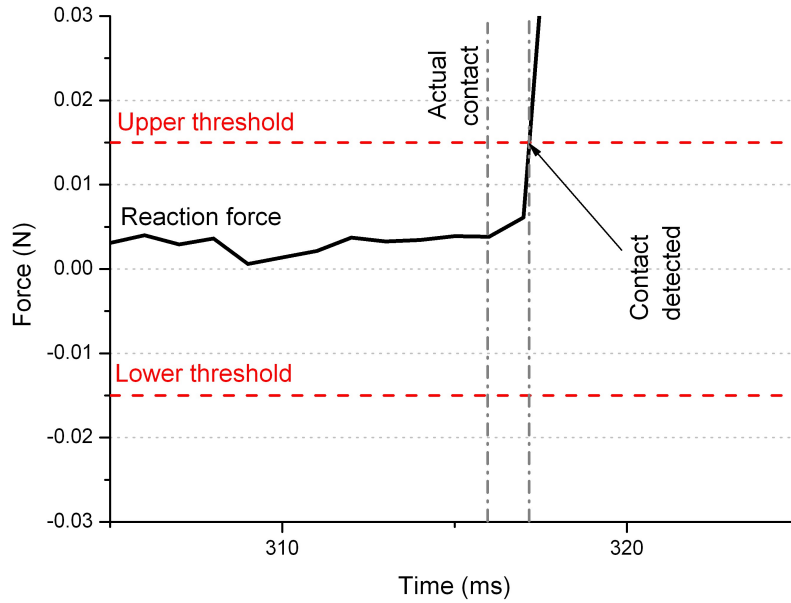
with $\epsilon_f = 0.015$ N. The results are summarized in Fig. 3.6 that shows functions fitted to the measured delays under each condition in the form of $f(v) = a - bc^v$ where v is contact velocity. Raw data are shown only for the foam ball for visibility (red points in the figure). Overall, the delay decreases as contact velocity increases or object stiffness increases.

Since the detection delay was shown to be a function of contact velocity, we needed to find a range of contact velocities of the human's general tapping motion. For stiffness perception, the human tends to keep the contact velocity relatively high in order to obtain sufficient tactile and kinesthetic sensory information from a contact. We collected tapping profiles with three human subjects, and computed tapping velocities at a contact. The results are shown in Fig. 3.7 as a histogram of the contact velocities. The tapping velocities varied from 100 to 1000 mm/s with the average of 416 mm/s. In Fig. 3.6, the detection delays were less than 3 ms when contact velocity was over 100 mm/s, even for the softest object.

With such small delays, the time that a user touches a real object with the haptic device tool and the subsequent time that the haptic interface begins stiffness modulation are perceived to be simultaneous. Although situations are not identical, the contact detection delay



(a) Measured variables.



(b) Magnified graph of (a) around the contact for a detailed view.

Fig. 3.5 Measured variables for contact detection.

of our AR system is much smaller than previously published thresholds for tactile simultaneity. For instance, research showed that for two tactile pulses applied on the index and

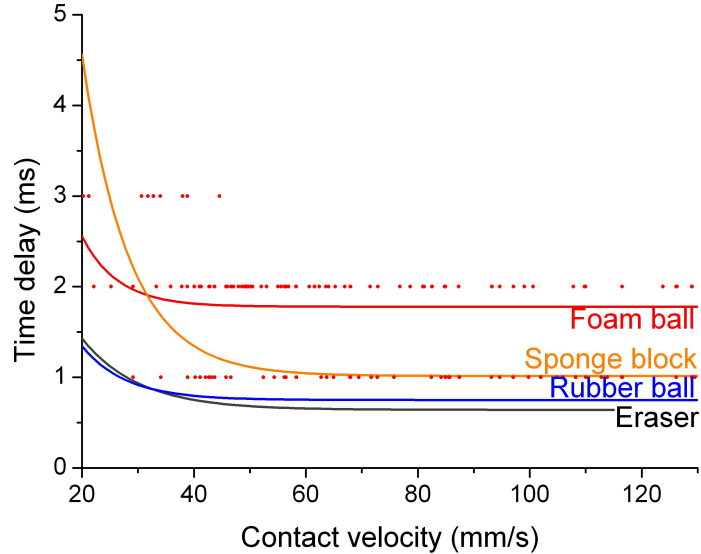


Fig. 3.6 Contact detection delays measured with $\epsilon_f = 0.015$ N. The sampling rate for contact detection was 1 kHz.

middle fingers to be perceived as different events, onset time difference between them needs to be larger than 30 ms [38], 75 ms [102], and 53 ms for old adults and 21 ms for young adults [20]. The insignificance of the contact detection delay was also confirmed from the comments of the subjects who participated in the experiment. As a result, the author can conclude that such small detection delays do not incur any perceptible abnormalities.

In addition, the author acknowledges that using other sensors such as an accelerometer and a contact switch in addition to the force sensor may further improve contact detection. Further improvements, however, would probably be perceptually insignificant or marginal, given the sufficiently small time delay of contact detection in our current system, despite increases in the system cost and complexity.

3.3 Force Control

After a contact between the haptic device tool and a real object is detected, we need to control the device-generated force for stiffness modulation. This section is devoted to a

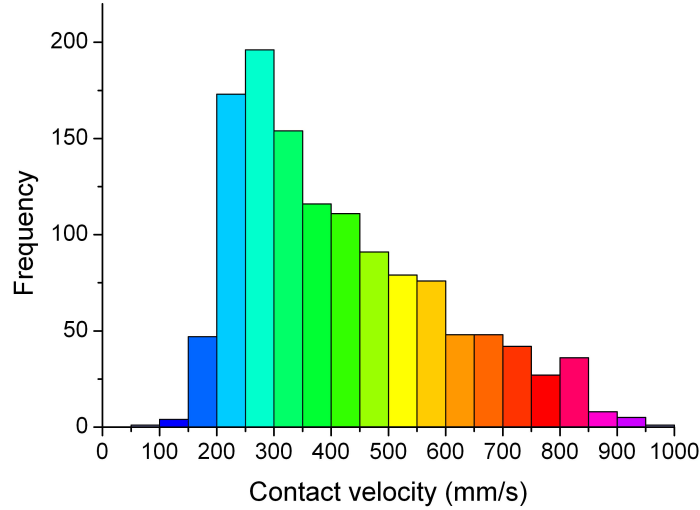


Fig. 3.7 Histogram of contact velocities (mean=416.2 mm/s and median=372.3 mm/s).

force control algorithm for this purpose, along with its performance evaluation.

3.3.1 Algorithm

Real objects often have complex dynamic responses that are generally nonlinear (even with hysteresis and inhomogeneity), which makes their precise identification time-consuming and impractical. Thus, our force control algorithm only uses the force sensor output to estimate the reaction force $f_r(t)$ without considering the object dynamics.

After a contact between an object and the haptic tool is detected, the desired device force $\tilde{f}_d(t)$ is determined using (3.3). To control the force produced by a haptic interface, $f_d(t)$, to be $\tilde{f}_d(t)$, the traditional closed-loop stiffness controller based on the PD control was used [74], such that:

$$f_c(t) = f_c(t-1) + K_p f_e(t) + K_d \frac{df_e(t)}{dt}, \quad (3.6)$$

where $f_c(t)$ is a force command to be sent to the haptic interface, $f_e(t) = \tilde{f}_d(t) - f_d(t)$ is a force error term, and K_p and K_d are proportional and derivative gains, respectively.

A delicate issue in the above rule is that to measure $f_d(t)$, an additional force sensor needs to be added to the haptic interface, e.g. between the third joint of the PHANTOM

and the ball grip in Fig. 3.2. To avoid it, it was estimate by $f_d(t) = f_c(t - 1)$, which is a heuristic observer that regards the force generated by the haptic interface as the command sent one sampling period before. The estimation rule works quite well due to the fast haptic update rate when the user motion is stabilized (e.g., see [23]). However, $f_d(t)$ can be delayed from $f_c(t - 1)$ by a few milliseconds when the PHANToM moves quickly, e.g., for tapping. Using an additional force sensor can remove the error, but the consequent performance improvement is likely to be insignificant in terms of perception. Indeed, our psychophysical experiment to be presented in Section 3.4 showed that the lag does affect the perceived magnitude of object stiffness, but the perceptual difference can be ignored negligible compared to the discriminability of human stiffness perception.

The range of stiffness that can be obtained via the stiffness control is contingent upon haptic interface performance, especially maximum output force, and force applied by the user. Consider the limited force output of a haptic interface, such that $f_{d,min} \leq f_d(t) \leq f_{d,max}$ where $f_{d,min} < 0$ and $f_{d,max} > 0$ in the setup shown in Fig. 3.1. Given the force applied by the user's hand, $f_h(t)$, (3.1) can be rewritten as

$$\frac{f_h(t) + f_{d,min}}{k(t)} \leq x_r(t) \leq \frac{f_h(t) + f_{d,max}}{k(t)}. \quad (3.7)$$

Then, using (3.2) results in

$$k(t) \frac{f_h(t)}{f_h(t) + f_{d,max}} \leq \tilde{k}(t) \leq k(t) \frac{f_h(t)}{f_h(t) + f_{d,min}}. \quad (3.8)$$

Using this equation, the ranges of feasible stiffness for four kinds of commercial haptic interfaces are illustrated in Fig. 3.8 as a function of $f_h(t)$ when $k(t) = 1.0$ N/mm. $f_{d,min}$ and $f_{d,max}$ are taken from the maximum forces along the vertical directions of the device listed in the product data sheets. Note that increasing $f_h(t)$ diminishes the effect of stiffness modulation by the haptic interface.

In practice, the feasible stiffness range is further limited by the stability requirement of haptic interaction. The stability of a haptic AR system depends on several factors, such as an algorithm used to control $f_d(t)$ to $\tilde{f}_d(t)$, the response characteristics of real objects, and the dynamics of a haptic interface.

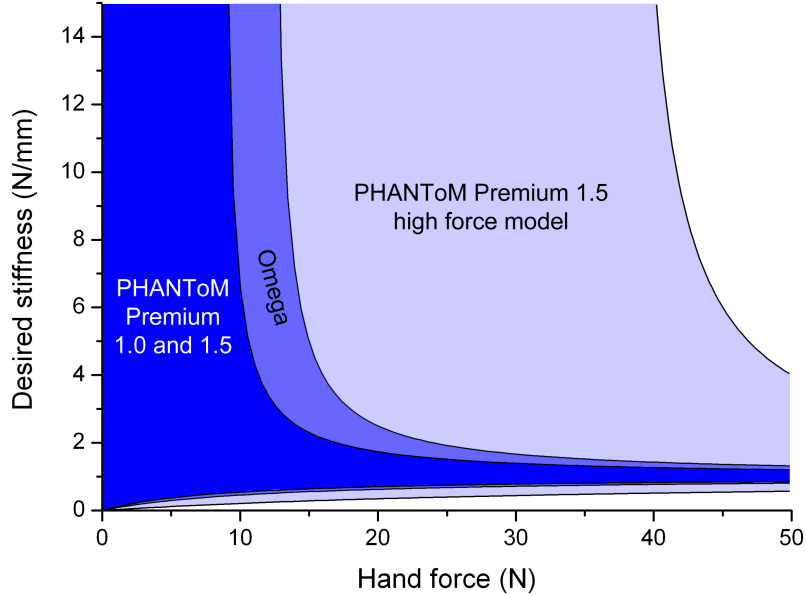


Fig. 3.8 Feasible stiffness ranges obtained using (3.8) with $k(t) = 1.0$ N/mm. Note that the range of Omega includes those of PHANToM 1.0 and 1.5, and the range of PHANToM 1.5 high-force model also includes those of PHANToM 1.0 and 1.5, and Omega. Regions above 15 N/mm are not shown for space.

3.3.2 Performance Evaluation

The force control ability of our AR system was tested with the four real objects used in Section 3.2.2. The user tapped each object with the PHANToM, and the resulting tip displacement and reaction force were measured. The whole system was controlled at 1 kHz. Force sensor readings were processed in the same way for contact detection. The force sensor read values at 10 kHz, and each 10 readings were averaged for feedback control of one period. The PD control gains were carefully tuned taking into account both force tracking error and contact stability using the Ziegler-Nichols method [108] followed by manual tuning. In the Zeigler-Nichols method, K_d is initially set to zero, and then K_p is increased until it reaches the critical gain, K_c , where the output of the control loop begins to oscillate. The final K_p is set to $0.6K_c$ and K_d to $K_p T_c/8$, where T_c is the oscillation period. The gains were further tuned manually. Actual stiffness values were computed from the displacement

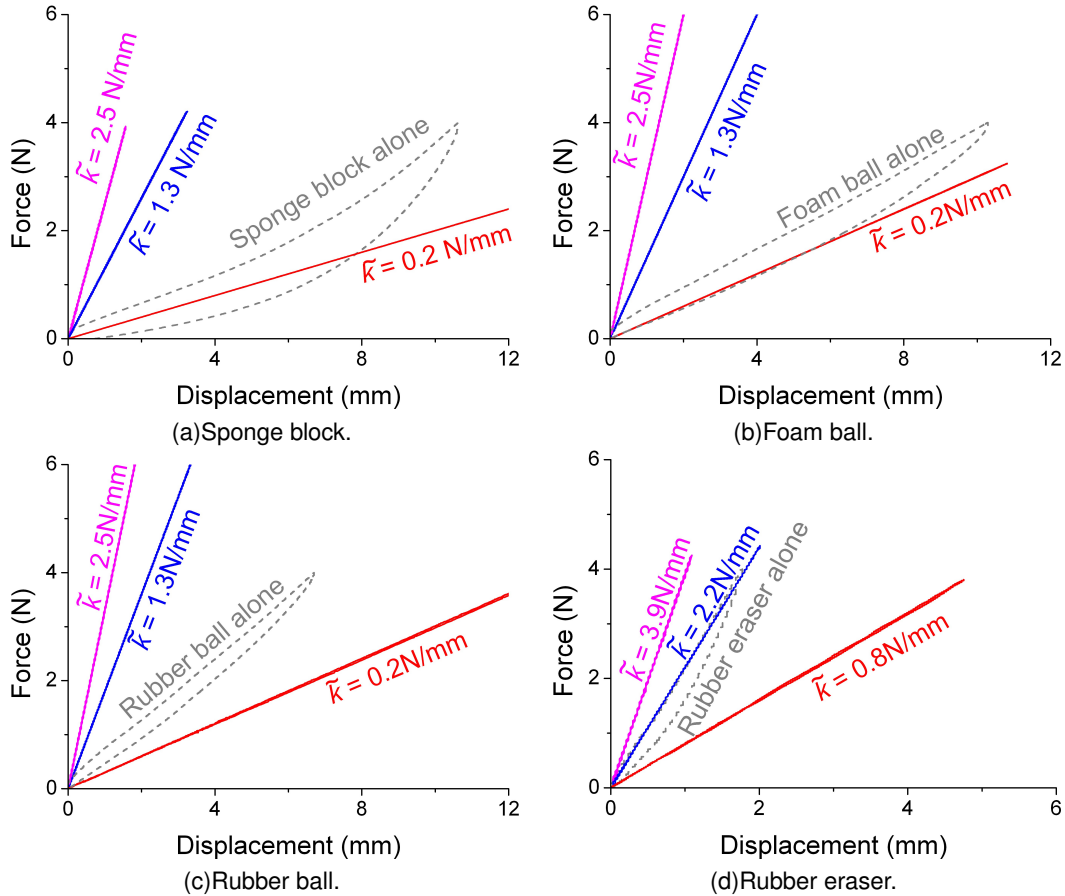


Fig. 3.9 Displacement-force curves of stiffness modulation. The original stiffness of real objects (the slope of the grey dashed curves) was modulated to have desired stiffness (the slope of the colored solid curves). Note that the non-linear visco-elastic responses of real samples were changed to follow linear elastic models used in our algorithm.

and force data and compared to the desired stiffness. For all of the real objects, the stiffness modulation was shown to be very effective with almost negligible stiffness errors, as demonstrated in Fig. 3.9.

The range of achievable stiffness was also examined using the four real objects and two haptic interfaces, PHANToM Premium 1.0 and PHANToM Premium 1.5 high-force model. A weight (408 g for 4 N gravity) was firmly attached on the hand grip of the PHANToM to simulate a stable and passive hand force. This weight was chosen based on the average

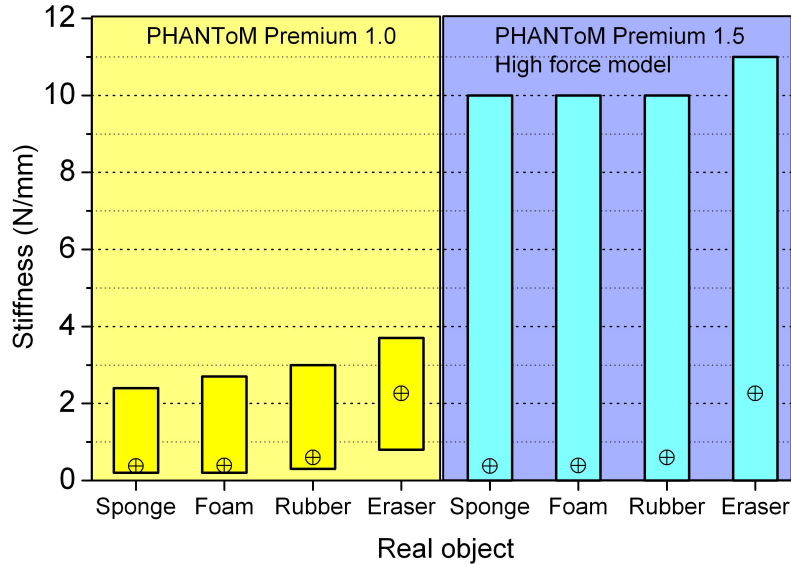


Fig. 3.10 Ranges of stiffness values stably modulated in our haptic AR system.

pressing forces of several participants in pilot studies. Note that whereas the user's hand holding the PHANToM stylus improves stability due to its physical damping in haptic AR, its absence in this simulated hand impedance would make a more challenging situation for the PHANToM to maintain stability. The PD control gains were tuned separately for each object and haptic interface. The desired stiffness, $\tilde{k}(t)$, was systematically changed within the feasible stiffness range; it was increased until unstable oscillations began, and decreased until the lower bound was met. The results are represented in the box plots in Fig 3.10. The circled crosses in the figure mark the representative stiffness of the corresponding real objects. As expected, the achievable stiffness ranges of the PHANToM high-force model are much larger than those of the PHANToM 1.0. The greater exertable force, higher damping, and higher apparent mass at the tool tip of the PHANToM high-force model seem to contribute to the more stable results.

It is interesting that the upper bounds of achievable stiffness tended to be higher than the sum of the stiffness of a real object and the maximum stiffness of the usual open-loop virtual wall rendering (about 1.0 N/mm for the PHANToM 1.0 and 8.0 N/mm for the PHANToM

1.5 high force). We speculate that two factors positively affected the rendering stability of our haptic AR system. Real objects usually contain damping in their dynamics, as indicated by the displacement-force curves that are convex downward in Fig. 3.9. It is a well known fact that such physical damping enhances haptic rendering stability [27]. The carefully tuned closed-loop force controller in our system also improved the rendering stability. We empirically confirmed that the maximum stiffness for stable virtual wall rendering increased to 1.3 N/mm for the PHANToM 1.0 if the closed-loop control was used.

In the experiment, the PD gains were tuned for each combination of haptic interface and real object to find the maximum stiffness range for stable rendering. Note that the gains differ significantly for the haptic interface, but not for the real object ($K_p = 0.4 - 0.5$ and $K_d = 0.01 - 0.02$ for the PHANToM 1.0, and $K_p = 1.0 - 1.1$ and $K_d = 0.02 - 0.03$ for the PHANToM 1.5 high force). This allows us to use fixed gains regardless of real objects to be tapped, maintaining our assumption of no prior knowledge on an environment.

The system was also tested using a wood plate, but the response was unstable over the entire range of \tilde{k} . This result indicates the need of a fundamentally different technique for highly stiff objects, such as playing tactile transients at a contact [90, 68, 64].

3.4 Psychophysical Experiment

We perceptually evaluated the approach, algorithms, and implementations presented in the previous sections for haptic AR in a psychophysical experiment. The experiment measured the Points of Subjective Equality (PSEs) of perceived stiffness altered by our system under various conditions, and compared them to desired stiffness values.

3.4.1 Methods

Apparatus

For a haptic interface, the experiment used a PHANToM model 1.0 instrumented with the force sensor and the contactor assembly as in Fig. 3.2. A real object to touch was placed on a custom-built rigid turn-table (see inside the semi-transparent white box in Fig. 3.11), and



Fig. 3.11 Experimental environment. The blurred scene inside the white paper box is for illustration, and was not seen by the subjects in the experiment.

was rotated appropriately by the computer during the experiment.

Subjects

Eight subjects (S1 – S8; 18 – 29 years old with the average of 23.9) participated in the experiment, and were compensated for their help. All subjects were right-handed by self-report, and only S1 was a female. S1, S3, and S5 had participated in haptic perception experiments prior to the present experiment but were not experienced users of a force-feedback device. The other subjects had not been exposed to any haptic interfaces prior to the present experiment. No subject was informed of the goals of the experiment.

Stimuli

In each trial, the subject was presented with reference and comparison stimuli in pairs. For the reference stimulus, a real object on the turn table was rotated to the predetermined position under the PHANToM interaction tool, and its stiffness was modulated to be a desired value by our haptic AR system. For the comparison stimulus, the real object was moved away, and the usual elastic virtual wall was rendered by the PHANToM only. The task given to the subject was to feel both stimuli and select a harder one.

Since the current haptic AR framework only uses the displacement-force relationship for stiffness alteration, the effect of contact transient cues had to be minimized in the experiment. For this, our experiment program automatically guided the interaction tool held by the subject to the contact position *very slowly* (velocity limit = 15 mm/s). The subject was instructed to just follow the tool during the guidance. After the tool reached the contact position, the guidance force was withdrawn, and the tool stopped moving. The subject was then allowed to begin pressing the tool along the vertical direction of the tool (downward in Fig. 3.11) for stiffness perception. To prevent the subject from repeatedly tapping the real object, which may produce tactile contact cues, tool movements above the contact point were constrained during pressing via active position control applied to the PHANToM. Tool movements in the lateral directions were also subject to the same position control.

In order for the subjects to use only the haptic cue, no visual or auditory information was provided, but text was displayed on the monitor indicating the progress of the experiment. A white paper box, shown semi-transparently in Fig. 3.11, enclosed the PHANToM and a real object, eliminating any visual cues. Auditory cues were also precluded by white noise played through headphones worn by the subjects.

Experimental Conditions

The experiment had two independent variables. One variable was the kind of real objects used for a reference stimulus. The sponge block (representative stiffness = 0.37 N/mm) and the rubber ball (representative stiffness = 0.59 N/mm) were selected, representing real objects with low and medium stiffness values, respectively. The other variable was the target

stiffness of a reference stimulus, i.e., the desired stiffness of a real object to be modulated by the haptic AR system. It was either 0.3 N/mm (lower than the representative stiffness of both real objects) or 0.7 N/mm (higher). The factorial combinations of the two independent variables led to four experimental conditions.

Procedures

As a psychophysical method, we used the method of limits that has balanced accuracy and efficiency for threshold estimation [40]. Under each experimental condition, four descending and four ascending series were repeated in a randomized order. Each series consisted of a number of trials. Since the two series were exactly symmetric, detailed procedures are provided only for the descending series in the following.

In a descending series, the initial stiffness of a comparison stimulus (virtual wall) was much higher ($\simeq 0.9$ N/mm for target stiffness 0.7 N/mm; note that the PHANToM 1.0 can render a stable virtual wall for stiffness less than 1.0 N/mm [24]) than the desired stiffness of a reference stimulus for stiffness modulation. The initial stiffness was varied by some degree in each series to minimize the habituation and expectation errors that could otherwise bias threshold estimation in the method of limits [40]. As the series progressed, the stiffness of the comparison stimulus was decreased by a predetermined step size ($= 0.02$ N/mm) until the series was terminated.

In each trial of the series, the subject was presented with a pair of reference and comparison stimuli in a random order. To initiate a trial, the subject pressed a space bar in the keyboard. Then the interaction tool was automatically guided to the contact position, and the subject pressed the tool vertically to perceive the stiffness of the first stimulus, as described earlier in Section 3.4.1. To perceive the second stimulus, the subject pushed the space bar again and followed the same procedure. The maximum velocity and the trajectory of the tool were recorded during the pressing. In order to keep the consistency of pressing, the subject was instructed to maintain the pressing velocity at a moderate speed, and a trial that contained tool movements with abnormally large vertical velocity (150 mm/s) or in lateral directions (15 mm) was discarded and repeated again. After perceiving both stim-

uli, the subject was asked to enter one of three answers: “the first stimulus felt harder” by pressing the ‘1’ key, “the two stimuli had the same stiffness” by pressing the ‘2’ key, and “the second stimulus felt harder” by pressing the ‘3’ key. This completed one trial, and a next trial followed immediately with the stiffness of comparison stimuli decremented by a predetermined step size.

In the descending series, the subject’s responses were initially that the comparison stimulus felt harder than the reference stimulus. As trials continued, the responses were changed to that they had the same stiffness, and then to that the comparison stimulus felt softer. The series was terminated if the last answer was encountered in three consecutive trials. Ten to fifteen trials were usually required to finish each series.

Prior to the experiment, each subject went through a training session to become familiar with the experimental procedures. The subject also learned to maintain appropriate pressing velocity (40 – 150 mm/s) and moderate pressing force in order to prevent any device errors. One experimental condition took 30 – 40 minutes to complete, and the whole experiment about 3 hours. The subjects were required to take a rest after finishing one experimental condition, and could take a break whenever needed.

Data Analysis

Under each experimental condition, eight series (four ascending and four descending) were repeated per subject. The following procedure was applied to the recorded data of each subject. In the data of each series, upper and lower thresholds were computed first. For a descending series, the upper and lower thresholds were the means of the stiffness values of the comparison stimuli in two consecutive trials where the subject’s responses changed from “the comparison stimulus was harder” to “they had the same stiffness” and from “they had the same stiffness” to “the comparison stimulus was softer,” respectively. The PSE in the stiffness of the comparison stimuli of the series was the mean of the upper and lower thresholds. Similar procedures were used to find the PSEs of ascending series. The PSE of the experimental condition was then determined by averaging the PSEs of all of the eight series. The PSE computed in this way represents the stiffness of a comparison stimulus (vir-

tual wall) perceived to be equally stiff to the reference stimulus (real object with modulated stiffness).

3.4.2 Results

The PSEs and the differences between the PSEs and the desired stiffness values of the reference stimuli, both averaged across the subjects, are shown in Fig. 3.12 for the four experimental conditions. The standard errors represented by the error bars indicate little individual variations in the results. In Fig. 3.12a, it is evident that the PSEs were very different from the stiffness values of the real objects (0.37 N/mm for the sponge and 0.59 N/mm for the rubber ball) and close to the desired stiffness values of stiffness modulation, demonstrating the effectiveness of our haptic AR system. However, the PSEs were slightly larger than the desired values in all experimental conditions, as magnified in Fig. 3.12b. This suggests that the real objects augmented by our haptic AR system felt stiffer than the desired stiffness to some degree.

Whether the errors in stiffness modulation are significant in terms of perception can be tested by comparing the errors to the difference thresholds (or difference limens; DLs) of stiffness perception under the corresponding conditions. The haptics literature showed that the Weber fractions of stiffness perception were 0.23 for contra-limb motion [57], 0.22 for actively pinching finger motion [100], 0.2 for rotation at the metacarpophalangeal joint with open-loop force control [59], and 0.036 for the same motion with closed-loop force control [42]. In particular, [39] measured Weber fractions for stiffness discrimination using a desktop force feedback interface (PHANToM Premium 1.5) in a very similar posture to our experiment. The only difference is that whereas they used the precision grip to hold the PHANToM stylus, the subject in our experiment grabbed a ball-shaped tool with the thumb and index finger. The Weber fractions ranged from 0.08 – 0.12 for reference stiffness values in 0.3 – 1.2 N/mm. For our reference stiffness values (0.3 and 0.7 N/mm), we took the corresponding Weber fractions (= 0.09 both), computed DLs, and specified them in Fig. 3.12b. The PSE errors were smaller than or comparable to the corresponding DLs, except for the rubber ball with desired stiffness 0.7 N/mm which showed PSE error larger

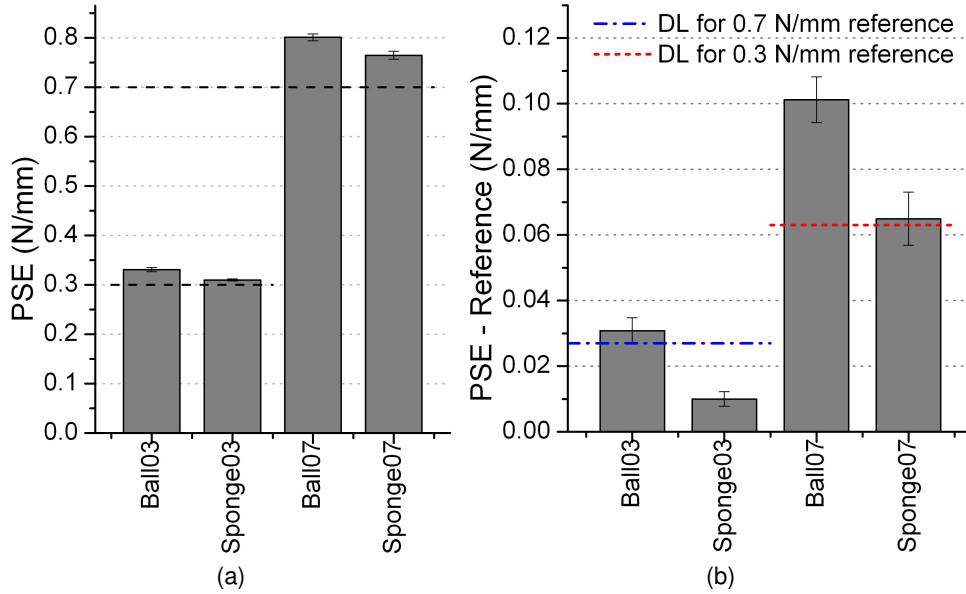


Fig. 3.12 Results of the psychophysical experiment averaged across the subjects. (a) PSEs. (b) Differences between the PSEs and the desired stiffness values of the reference stimuli computed from the data in (a) for better visibility. The difference thresholds taken from [39] are also shown in (b). Each experimental condition is denoted by combining the kind of a real object and the desired stiffness value for stiffness modulation used in the condition.

than DL by about 0.04 N/mm. Such small stiffness differences are negligible in practice considering that the DLs were measured in a laboratory with extremely attentive subjects. Therefore, we can state that the stiffness modulation errors in our haptic AR system were marginally perceptible if not imperceptible.

3.4.3 Discussion

The results of the psychophysical experiment showed that our haptic AR system can adequately alter the stiffness of a real object with perceptually negligible modulation errors. Nonetheless, it is beneficial to identify the sources that bias the stiffness modulation since the modulation errors appear to be systematic in Fig. 3.12b. Note that the earlier interpretations of the experimental results were based on the assumption that the force-feedback device used in the experiment was a perfect force transducer. In reality, however, there

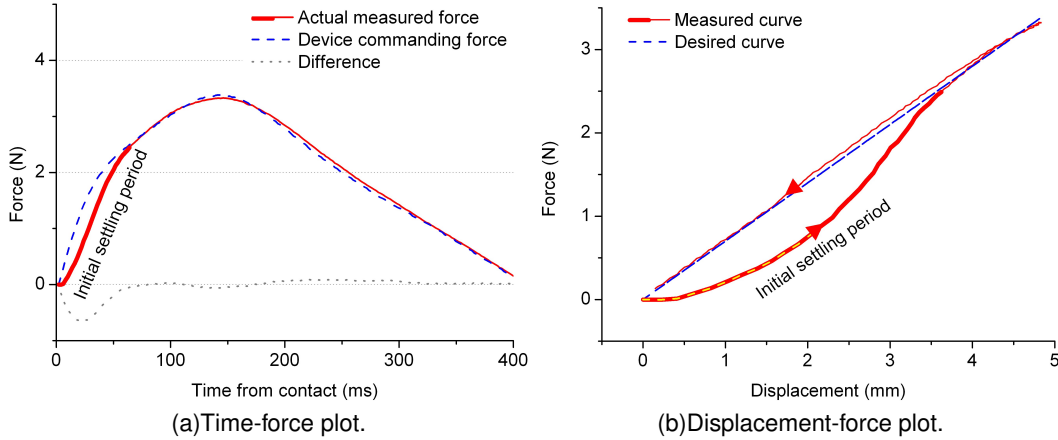


Fig. 3.13 The force command and the actual force generated by the PHANToM 1.0. A user pressed a virtual wall for the measurement.

always exists a difference between a force command and the force output of the device, especially due to the electromechanical dynamics of the device. In particular, in the pressing movement used in the experiment, the force generated by the device generally lags behind commanding force. An example is given in Fig. 3.13a where the actually measured force exerted to the hand holding the tool is shown for a virtual wall rendered using the PHANToM 1.0 with 0.7 N/mm stiffness. Over the entire period, the force command (blue dashed line) leads the actual force (red solid line). The difference between them usually grows with the changing rate of force command (see the grey dotted line). In particular, the lags are pronounced in the initial settling period (the thick part of the red solid line from 0 to 60 ms), making the actual force substantially smaller than the command. This phenomenon introduces an undesired counter-clockwise hysteresis in the displacement-force curve shown in Fig. 3.13b. It can be seen that the slope in the beginning of the curve (the yellow dashed part of the thick line) is less than the desired stiffness. Since the human relies more on the initial force change rate for stiffness perception [70], the lag may make the virtual wall feel softer than it should.

In the psychophysical experiment, the force lag existed in both of the comparison and reference stimuli. Since the comparison stimulus only used a virtual wall, its perceived

stiffness was likely to be less than the commanded stiffness. The reference stimulus had two different cases. If the haptic AR system attempts to make a real object stiffer, the haptic interface renders resistive force to the user's hand and adds it to that of the real object (acting upward in Fig. 3.2). Thus, it is suspected that the counter-clockwise hysteresis similar to one in Fig. 3.13b also affected the reference stimuli. However, its effect on the stiffness decrease must have been less significant than for the comparison stimulus, since the PHANToM rendered much larger and faster-changing force for the comparison stimuli. It follows that given a desired stiffness value, the reference stimulus was apt to render a stiffer object than the comparison stimulus, which biased the PSEs measured in the experiment to be higher than their true values.

To make a real object feel softer, the haptic interface adds force to the direction of the user-applied force (downward in Fig. 3.2). Thus, the force command for the reference stimulus points to the opposite direction of the reaction force of the real object. In this case, unlike Fig. 3.13b, the actuation lag creates a clockwise hysteresis in a displacement-force curve. This may increase the perceived stiffness of the reference stimulus, whereas the comparison stimulus was still perceived softer for the same desired stiffness value.

The above discussion strongly suggests that the actuation delay present in the haptic interface biased the PSEs measured in the psychophysical experiment to be higher than their true values. This was also supported by statistical analysis conducted for the two independent variables, the kind of a real object and the desired reference stiffness. Two-way within-subject ANOVA showed that both factors had statistically significant influences on the PSE errors ($F_{1,7} = 44.53$, $p = 0.0003$ for the kind of a real object and $F_{1,7} = 16.16$, $p = 0.005$ for the desired reference stiffness). For the reference and comparison stimuli to reach a desired stiffness value, the comparison stimulus needs to make more effort commensurate to the stiffness of a real object used in the reference stimulus. Thus, using a stiffer real object exacerbates the actuation lag in the comparison stimulus, which led to the larger PSE errors of the rubber ball than the sponge block in Fig. 3.12b. On the other hand, increasing the desired reference stiffness for the same real object also induces a larger force delay in the comparison stimulus, resulting in larger PSE errors, as confirmed in Fig. 3.12b.

As a consequence, we can conclude that the imperfect performance of the haptic interface caused the structural bias that increased the PSE errors in the psychophysical experiment. This further reduces the perceptual significance of the PSE errors discussed earlier based on the DLs of stiffness perception.

3.5 General Discussion

The psychophysical experiment confirmed that our haptic AR system can adequately modulate the stiffness real objects. Nevertheless, this work is our initial proof-of-concept study, and many remaining issues should be investigated.

For a practical application, a haptic AR system must be able to provide 3D interaction that enables a user to interact with real objects using any exploratory movements such as contour following and lateral motion. Since our goal is not to manage the geometric information of real environment, the 3D interaction will need to estimate (local) geometry of a real object such as surface normal and tangent plane at a contact point for force rendering. In addition, interface tool should be improved to support natural 3D interaction. Our efforts for these issues will be addressed in the next chapter.

Second issue is related to the structural stiffness of a haptic interface. Recall that one of our simplifying assumptions made in Sec. 3.1 was that a haptic interface is ideally rigid. In practice, the haptic interface deforms, and the amount of deformation is expressed by the structural stiffness of the device. The structural deformation cannot be seen by joint encoders in the haptic interface, causing errors in the displacement measurement. This problem becomes more apparent as more force is applied at the tool tip. For instance, the PHANToM 1.5 high force model has the structural stiffness of 3.5 N/mm, but with its maximum force (= 37.5 N), the displacement error can be as high as 10.7 mm. This significantly lowers actually rendered stiffness, and the amount of decrease grows with commanding stiffness. Thus, relatively high stiffness may not be rendered properly in our current haptic AR system. Note that this is an inherent problem of haptic rendering also present for virtual environments. Using parallel-linkage haptic interfaces (e.g., Omega and Delta from Force Dimension, Inc.) that have much higher structural stiffness can mitigate the problem, but

their much smaller workspace imposes a practical limitation on the usability of haptic AR applications. Developing a force-feedback haptic interface with large structural stiffness and large workspace can be a very challenging task. In the next chapter, we introduce a simpler and software-based approach for this issue.

Chapter 4

Stiffness Modulation: 3D Interaction

In this chapter, the author reports new haptic AR system of stiffness modulation for 3D interactions. The new system allows for arbitrary exploration patterns such as tapping, stroking, and contour following [71]. With this system, a user can perceive the shape of a real object with altered stiffness, which is the most fundamental requirement for practical applications such as the example of a virtual tumor inside of a real mannequin in Section 1.1. Besides, this work is a prerequisite for augmenting other haptic attributes including friction and texture. A particular focus has been on maximizing the usability of the system, while maintaining convincing perceptual quality. To balance the trade-off between the rendering quality and usability, we establish performance requirements that ensure the perceptual quality for each computational module and find a reasonable amount of preprocessing that satisfies the requirements.

The rest of this chapter begins with modeling of 3D interaction between the tool of a haptic interface held by the user and a real object being explored via the tool (Section 4.1). This model leads to the desired force that the haptic interface should exert to provide a desired stiffness to the user as well as required computational modules to make the desired force. We then establish physical performance requirements for each module that are needed to maintain an acceptable perceptual quality of the system (Section 4.2). Considering these re-

quirements, an efficient and accurate algorithm is developed for detecting a contact between the device tool and the real object (Section 4.3). What follows are effective algorithms for estimating the direction of the desired device force (Section 4.4) and its magnitude (Section 4.5). To ensure that a force produced by the haptic interface faithfully tracks the desired force, we also use a stiffness control algorithm adapted from robotics with explicit consideration of the device structural stiffness (Section 4.6). The performances of each algorithm are thoroughly evaluated with real samples. In addition, perceptual performance of the whole system is evaluated through a psychophysical experiment (Section 4.7).

4.1 Interaction Modeling

Our 3D haptic AR system is fully operational with real objects that satisfy the following two assumptions. First, analogous to the 1D haptic AR system, we only consider real objects in the elastic state with moderate stiffness. Objects made of plastic (e.g., clay) or brittle materials (e.g., glass) are excluded due to their highly complex responses. Objects made of highly stiff materials (e.g., steel) cannot be handled due to the limited position sensing resolution and force output of the current haptic device. In addition, we prefer to use a commercial haptic interface to maximize the applicability of our work. Second, our system assumes real objects of homogeneous dynamic responses. This simplification was required for a model-based estimation of real object deformations. Even though no real objects are strictly homogenous, our system shows acceptable performance for a large class of objects.

We denote the stiffness of a real object being pressed by a user at time t by $k(t)$. This is the stiffness perceived by the user if no virtual force is rendered. The goal is to alter the user-perceived stiffness from $k(t)$ to a desired stiffness value, $\tilde{k}(t)$, by providing an adequate virtual force to the user's hand. Variables necessary to model the interaction are defined in Fig. 4.1. Let the forces acting at the tool tip by the haptic interface and the user's hand be $\mathbf{f}_d(t)$ and $\mathbf{f}_h(t)$, respectively. The two force components deform the object surface and result in the reaction force $\mathbf{f}_r(t)$ in a steady state such that

$$\mathbf{f}_r(t) = -\{\mathbf{f}_h(t) + \mathbf{f}_d(t)\}. \quad (4.1)$$

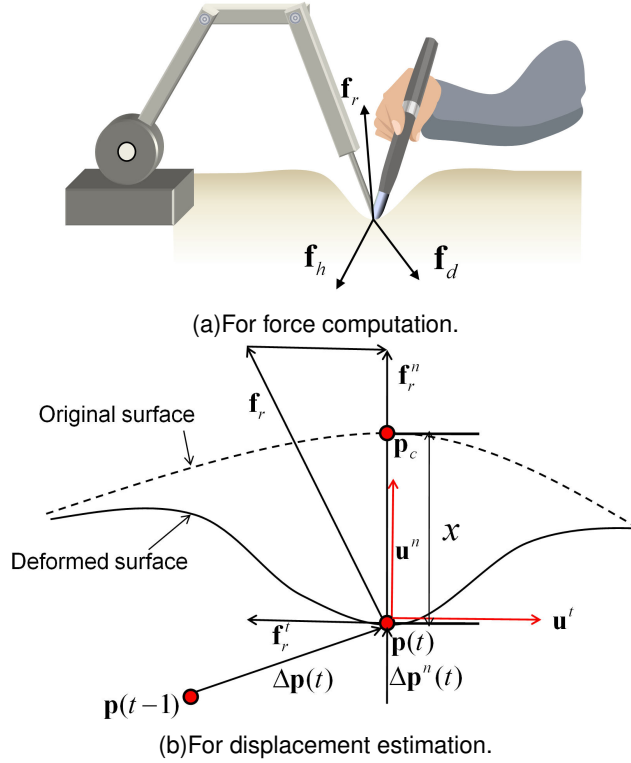


Fig. 4.1 Definitions of variables for 3D stiffness modulation.

On the other hand, $\mathbf{f}_r(t)$ during a contact can be decomposed into two perpendicular force components:

$$\mathbf{f}_r(t) = \mathbf{f}_r^n(t) + \mathbf{f}_r^t(t), \quad (4.2)$$

where as illustrated in Figure 4.1b, $\mathbf{f}_r^n(t)$ and $\mathbf{f}_r^t(t)$ are force components resulted from the object elasticity and the friction between the tool tip and the object surface, respectively. Let the position of the haptic interface tool tip be $\mathbf{p}(t)$, which is also the position of a particle contacting the tool tip on the object boundary. Then, the elastic force component $\mathbf{f}_r^n(t)$ makes a deformation of displacement $x(t)$, which is the distance between $\mathbf{p}(t)$ and the original non-deformed position of the contacted particle, $\mathbf{p}_c(t)$ (Personal communication with Sangyul Ha, an expert on continuum mechanics). Let a unit vector representing the direction of $\mathbf{f}_r^n(t)$ be $\mathbf{u}^n(t)$. Then, for the hand to feel $\tilde{\mathbf{k}}(t)$,

$$\tilde{\mathbf{f}}_h(t) = \tilde{k}(t)x(t)\mathbf{u}^n(t). \quad (4.3)$$

Using (4.1), the force that the haptic device needs to exert is

$$\tilde{\mathbf{f}}_d(t) = -\mathbf{f}_r(t) - \tilde{k}(t)x(t)\mathbf{u}^n(t). \quad (4.4)$$

Equation (4.4) indicates that in order to modulate the object stiffness, we need to measure the reaction force $\mathbf{f}_r(t)$ and estimate the direction, $\mathbf{u}^n(t)$, and magnitude, $x(t)$, of the resulting deformation. Furthermore, to initiate stiffness modulation, the time instance at which the haptic tool touches the real object must be accurately detected. After the contact detection, the device force $\mathbf{f}_d(t)$ should be controlled to exert a desired force $\tilde{\mathbf{f}}_d(t)$. The following section describes the physical performance requirements for these issues to ensure the acceptable perceptual qualities.

4.2 Performance Requirements

For the aforementioned issues, we can adapt conventional haptic rendering algorithms for virtual objects to haptic AR if the entire geometries of real objects are available. However, such geometry modeling of real objects requires a large amount of preprocessing using dedicated hardware such as a 3D laser scanner and a robotic 3D digitizer. This aspect seriously reduces the usability of a system and is not in agreement with the general advantages of AR. Thus, our algorithm aims at minimizing such impracticality with minimal perceptual performance degrade.

Nevertheless, partial information on real objects greatly facilitates the computational procedure in our haptic AR system. For example, local geometry information around the contacting position is very helpful for estimation of deformation direction and magnitude. This information can be estimated either in an on-line process or in an off-line preprocess. The on-line process is preferable to the usability of the system, whereas some of the information needs a dedicated off-line preprocess. Establishing minimum performance requirements for each module is beneficial for balancing this trade-off relation. Although

the performance requirements are certainly dependent on applications, they can be used as a guideline for developers. We first build the requirements for the static performance and discuss the requirements for the dynamic performance.

The reaction force measurement, $\mathbf{f}_r(t)$, directly affects the desired force calculation according to (4.4). Thus, the static error of the force measurement should be lower than the human detection threshold for the force magnitude. The literature reported that the JND (just noticeable difference) of force magnitude perception is around 8 % [87].

For the contact detection algorithm, the detection accuracy and the time delay between the detected contact time using the algorithm and the actual contact time can be performance measures. The false alarm (declaring a contact for the non-contact movements) would critically deteriorate the quality of the rendering, and thus it must be avoided. The detection delay also should be no more than the threshold for the tactile simultaneity of human in order to ensure that the time that a user touches a real object with the haptic device tool and the subsequent time that the haptic interface begins stiffness modulation are perceived to be simultaneous. Literatures has shown that for two tactile pulses applied on the index and middle fingers to be perceived as different events, the onset time difference between them must be larger than 30 ms [38], 75 ms [102], and 53 ms for older adults and 21 ms for young adults [20]. Although the situations are not the same, we can guess that the delay should be bounded by around 20–30 ms.

The deformation direction, $\mathbf{u}^n(t)$, directly determines the direction of the stiffness rendering based on our stiffness rendering model in (4.3). If static errors (the angle difference between true and estimated direction) are present in the estimate, a user is delivered mis-directed force as the result of the modulation. Whether the static errors are perceivable to the user or not can be determined by comparing it with the human discriminability of the force direction. In the literature, it was reported that the JND of force direction perception is 18.4° regardless of a reference force direction when haptic and visual information is congruent [6]. We can take this threshold as an upper limit of the absolute angle error incurred by the inaccurate estimation of $\mathbf{u}^n(t)$.

For the deformation magnitude estimation, there exist no directly applicable perceptual

data to predict the perceptual effects of the errors. Instead, we can indirectly induce its effect on the stiffness rendering. Equation (4.3) indicates that errors in the displacement estimate, $x(t)$, make errors in the finally rendered force at a user's hand, consequently resulting in errors in rendered stiffness. The rendered stiffness is linearly related to the displacement error. This linear relation allows to compare the Weber fraction of the stiffness perception with the ratio of the displacement errors to the true displacement for testing whether the errors are perceptually significant. As aforementioned in Section 3.4.2 the reported Weber fraction ranged from 0.08 – 0.12. In the deformation magnitude estimation, the error ratio should be lower than this value for perceptually sound stiffness rendering.

In addition to the static errors in the above three issues, presumably more important factor for perception is dynamic abnormalities such as high frequency oscillation of the rendered force. Human is quite sensitive to such vibration [25]. They result from various sources; jitter in force sensor reading, inaccurate and unstable estimation of the deformation direction and magnitude, self-exciting oscillation in the closed-loop force controller, and instability of the hardware. However, isolating and identifying the error sources are quite hard task without extensive analysis of the hardware dynamics, algorithms, and system stability. Thus, we focus on the perceptual soundness of the finally rendered force to assess the dynamic performance of the system. Using various techniques such as low-pass filtering and fine tuning of closed-loop controller, the dynamic abnormalities should be reduced to the degree that they are not perceivable to a user in a reasonable range of desired stiffness.

In the following sections, our approaches for the issues are described and evaluated with the consideration of the requirements and usability.

4.3 Contact Detection

4.3.1 Algorithm

The first step of rendering is to detect a contact between the tool tip and a real object. If a contact is declared, we begin stiffness modulation using the algorithms described in the next sections. Otherwise, the haptic interface renders no forces.

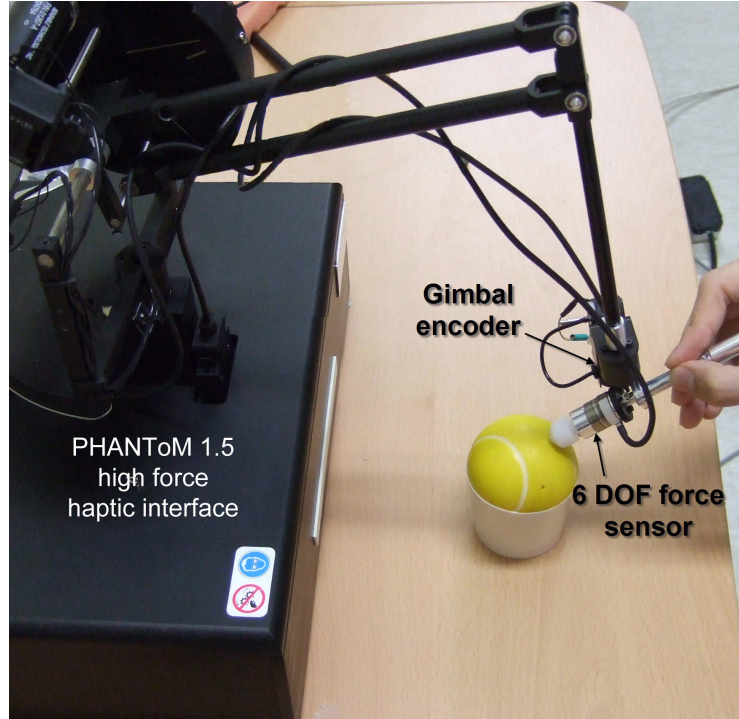


Fig. 4.2 PHANTOM augmented for 3D stiffness modulation.

Our approach for contact detection is to estimate the response force $\mathbf{f}_r(t)$ from a force sensor reading $\mathbf{f}_s(t)$ and catch the time instant when its absolute values show an abrupt rise. For this, we attached a 6D force/torque sensor (ATI Industrial Automation, Inc.; model Nano 17) at the tip of the stylus of a PHANTOM (model 1.5 High Force; see Fig. 4.2). In addition to $\mathbf{f}_r(t)$, $\mathbf{f}_s(t)$ responds to the inertia and gravity forces of the contactor assembly, $\mathbf{f}_i(t)$ and $\mathbf{f}_g(t)$, respectively. It follows that

$$\mathbf{f}_r(t) = \mathbf{f}_s(t) - \mathbf{f}_g(0) - \mathbf{f}_i(t) + \mathbf{f}_g(t). \quad (4.5)$$

At the beginning of rendering at $t = 0$, the joint encoders and the force sensor are initialized at a predetermined configuration ($\mathbf{f}_i(0) = \mathbf{0}$) without a contact ($\mathbf{f}_r(0) = \mathbf{0}$). Let $\mathbf{f}_g(0)$ be an initial gravity force of the contact assembly such that

$$\mathbf{f}_g(0) = Gm_t\mathbf{u}^g(0), \quad (4.6)$$

where G is the gravity acceleration (9.807 m/s^2), m_t is the mass of the tip assembly (12.59 g in our system), and $\mathbf{u}^g(0)$ is the direction of gravity at the initialization. Since $\mathbf{f}_s(t)$ includes the initial gravity component thereafter, it must be compensated to find $\mathbf{f}_r(t)$.

The inertia force $\mathbf{f}_i(t)$ can be derived by

$$\mathbf{f}_i(t) = m_t \mathbf{a}(t), \quad (4.7)$$

where $\mathbf{a}(t)$ is the acceleration of the tool tip. To estimate $\mathbf{a}(t)$, we use the double discrete differentiation of $\mathbf{p}(t)$. Filters are used twice to obtain velocity $\mathbf{v}(t)$ from $\mathbf{p}(t)$ using the first-order adaptive windowing filter [53] and then to estimate $\mathbf{a}(t)$ from $\mathbf{v}(t)$ using a second-order Butterworth low-pass filter with a 50-Hz cutoff frequency. This results in quite accurate and smooth estimates [55].

Lastly, the gravity force $\mathbf{f}_g(t)$ is computed by

$$\mathbf{f}_g(t) = G m_t \mathbf{T}_s(t) \mathbf{u}^g(0), \quad (4.8)$$

where $\mathbf{T}_s(t)$ is a 3×3 rotation matrix of the contactor tip obtained from the joint angles and the kinematics of the haptic device. Using (4.6), (4.7), (4.8), $\mathbf{f}_r(t)$ in (4.5) can be determined.

We declare a contact if $|\mathbf{f}_r(t)| > \epsilon_f$, where ϵ_f is a decision threshold that depends on the accuracy of $\mathbf{f}_r(t)$ estimation. To find ϵ_f , we increase it until no false alarms (declaring a contact for non-contact movements) are observed for many real objects. In order to take into account the gravity of the rotating tip assembly, this contact detection algorithm for 3D interaction is extended from a simpler algorithm for 1D interaction in Chapter 3 where the tip assembly had a fixed orientation for 1D interaction. Note that the algorithm requires no prior knowledge on the geometric relations between real objects and the haptic interface.

4.3.2 Performance Evaluation

For all experimental evaluations in this chapter, we used four real objects with different geometries and stiffness characteristics shown in Fig. 4.3. The representative stiffness of each object was measured at a loading force of 4 N and specified in the figure. In particular,

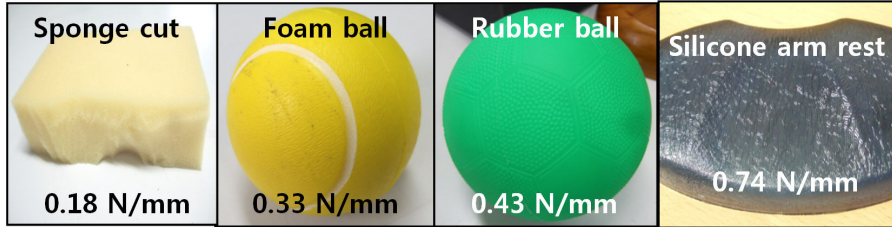


Fig. 4.3 Four real objects used in the experiment.

the sponge cut had a rugged surface, and this surface was used for all experiments. The experimental results are compared to the performance requirements defined in Section 4.2.

The decision threshold for contact detection, ϵ_f , determined by the procedure described in the previous section, was 0.06 N. This value was used for all experiments reported in this section.

We experimentally measured time differences between the true and detected instances of a contact while repeatedly tapping on the four real objects with various velocities in several movement directions. To pinpoint the exact time of contact, the coordinates of points on an object surface were gathered using the PHANTOM, and the time instance when the tool tip passed through these points was taken as the true contact time. The results are summarized

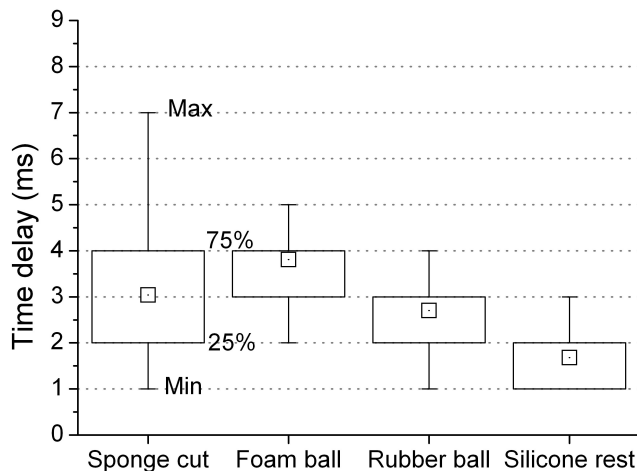


Fig. 4.4 Distributions of contact detection delays. The small squares represent the averages.

in Fig. 4.4. The means of the contact delays were less than 4 ms. Even for the softest object (sponge cut), the largest time delay was 7 ms, which is quite smaller value than the thresholds for the tactile simultaneity mentioned in Section 4.2. Such small contact delays do not incur any perceptual abnormality in stiffness modulation.

4.4 Estimation of Deformation Direction

Once a contact between a real object and the haptic tool has been detected, the force $\tilde{\mathbf{f}}_d(t)$ in (4.4) needs to be rendered for stiffness augmentation. In addition to $\mathbf{f}_r(t)$ determined in (4.5), we further need to find $\mathbf{u}^n(t)$ and $x(t)$. For this, one may adapt conventional haptic rendering algorithms for virtual objects if the entire geometry of the real object is available. Suppose that the tool tip makes an initial contact at particle $\mathbf{p}(0)$ on the surface of the real object. If a contacting particle remains the same as $\mathbf{p}(0)$ thereafter, then $\mathbf{p}_c(t) = \mathbf{p}(0)$, and $\mathbf{u}^n(t)$ and $x(t)$ can be easily found from $\mathbf{p}_c(t) - \mathbf{p}(t)$ (see Fig. 4.1b). However, as soon as the tool tip begins to move on the surface, $\mathbf{p}_c(t)$ ceases to be the same as $\mathbf{p}(0)$. In this case, $\mathbf{p}_c(t)$ cannot be clearly identified without the object geometry information. Geometry modeling, however, greatly reduces the usability of AR system where real objects can be frequently changed. This section explains our algorithm that aims at minimizing such impracticality in our framework, and reports their physical evaluation results.

We first estimate the deformation direction $\mathbf{u}^n(t)$ as follows. $\mathbf{f}_r(t)$ during a contact consists of two force components:

$$\mathbf{f}_r(t) = \mathbf{f}_r^n(t) + \mathbf{f}_r^t(t), \quad (4.9)$$

where as illustrated in Fig. 4.1b, $\mathbf{f}_r^n(t)$ and $\mathbf{f}_r^t(t)$ are force components resulted from the object elasticity and the friction between the tool tip and the object surface, respectively. Given $\mathbf{f}_r^t(t)$, the direction of $\mathbf{f}_r(t)$, $\mathbf{u}^n(t)$, can be determined by

$$\mathbf{u}^n(t) = \frac{\mathbf{f}_r(t) - \mathbf{f}_r^t(t)}{|\mathbf{f}_r(t) - \mathbf{f}_r^t(t)|}. \quad (4.10)$$

Equation (4.10) indicates that to determine the response force direction, estimating the friction force is sufficient instead of the geometric information of a real object. Thus, the

problem reduces to how to estimate $\mathbf{f}_r^t(t)$.

In general, a frictional response between a deformable object and a rigid tip cannot be easily formulated and identified due to large nonlinearity of the friction and difficulties in measuring the related physical signals [3]. Although large numbers of different friction models and identification methods have been introduced since 1960s, discovering a general and effective model that can be used for any two arbitrary objects is still an on-going research issue in tribology, physics, and robotics [104]. Building a new friction model is out of scope of this research, and it is desired to seek an optimal model among the existing friction models and their identification methods in terms of the accuracy, usability, and the perceptual goal for our haptic AR. Our effort for this is reported in the author's technical report [54]. As the result of this effort, we introduce two efficient and effective approaches for the friction estimation. Our approaches first identify the frictional response in an off-line process (Section 4.4.1), and use it to estimate $\mathbf{f}_r^t(t)$ in rendering (Section 4.4.2).

4.4.1 Friction Model Acquisition

We explain the model identification for a relatively simple yet effective approach using a ball bearing as a tool tip, and move on to more complicate but general approach using a rigid tool tip.

First Approach Using Ball Bearing Tool Tip

One way to greatly facilitate the friction identification is to use a tool tip with a very low friction, such as a ball bearing shown in Fig. 4.5. The ball bearing has negligible static friction and small kinetic friction with very low viscosity. This allows us to use a simple linear friction model for the identification. More importantly, changes in the friction response between the ball bearing and a real object surface remain fairly small for different objects. Once we obtain a friction model in an off-line process, we can use the model for stiffness modulation regardless of real objects with acceptable performance, as demonstrated in Section 4.4.3. Note that using a ball bearing also can be a reasonable validation of the assumption of the negligible friction between the tool tip and the surface defined for (4.3).

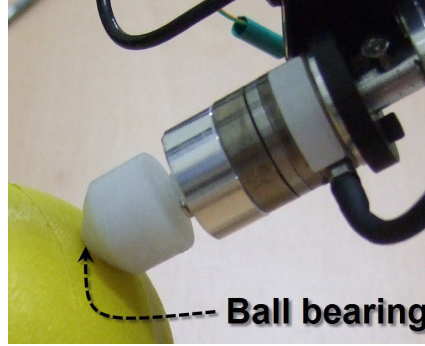


Fig. 4.5 Ball bearing tool tip.

As a friction model, we use the traditional Coulomb viscous model. Due to the extremely small static friction of the ball bearing, we can ignore the stick part, such that

$$f_r^t(t) = \mu_k f_r^n(t) + \mu_b v^t(t), \quad (4.11)$$

where $f_r^n(t)$ is the magnitude of the normal force component of $\mathbf{f}_r(t)$, $v^t(t)$ is the velocity of the haptic tool along the tangential direction, and μ_k and μ_b are the kinetic and viscous friction coefficients, respectively. The two model parameters cannot be identified in an on-line process since the true values of $f_r^t(t)$ are not available. The two coefficients are identified in an off-line process using the ARX model [75] with reliable data gathered in well-controlled strokes.

To determine the coefficients of the slip friction model in (4.11), we prepared ten flat real objects with various surface textures and stiffness values. For accurate friction measurement, the force sensor was firmly fixed to the last link of the PHANToM without the gimbal encoder, and exactly aligned to be perpendicular to an object surface. Data for normal force, lateral force, and lateral tip velocity were collected while stroking each object with different velocities and normal forces. The lateral force was taken as the friction force. The coefficients of the friction model were identified for each object using the measured data.

The identified coefficients are shown in Fig. 4.6a. For validation, we also compared the measured friction with the model output for all objects. An example is provided for rubber

mat 1 in Fig. 4.6b. The estimation errors were quite small with an average of 7%. This indicates that the simple friction model well explained the friction responses, in spite of the various sources of measurement noises such as the textures of real objects and the slightly irregular rotations of the ball bearing (see the noisy friction measurements in Fig. 4.6b). We averaged the friction coefficients of the five softer objects in Fig. 4.6a, and used them for friction estimation in the subsequent experiments ($\mu_k = 0.0643$ and $\mu_b = 0.000244$ Ns/mm).

When this algorithm is applied, a dominant error source is the friction model in (4.11), since one pair of friction coefficients are commonly used regardless of real objects. Despite this, the evaluation in Section 4.4.3 demonstrated that the errors in force direction during stiffness modulation remain unnoticeable, particularly due to the poor human discriminability of force direction [6].

Second Approach Using Solid Rod Tool Tip

The ball bearing significantly deteriorates the friction perception by removing the response of the real friction. It would be problematic when stiffness modulation is combined to friction modulation in the future. Only haptic virtuality would be possible since all feedback should be synthetically constructed instead of mixing the real and virtual friction.

Instead, in the second approach we use an aluminum rod with a round tip as shown in Fig. 4.7, which is more general form of the interaction tool tip. However, all the benefits of ball bearing are lost. In particular, a linear model such as used in (4.11) is not applicable due to relatively large nonlinear static friction. Also, we can no longer apply constant parameters for every object due to the large differences in friction characteristics of different real objects. In addition, large friction of a solid tool tip breaks our assumption defined for (4.3), e.g., negligible friction between the tool tip and the surface. But this does not make serious errors on the direction estimation, which is confirmed through our performance evaluation in Sec. 4.4.3.

We use the Dahl model for our friction identification [29]. The Dahl model shows reasonable performance with relatively low complexity for the identification (see [54] for review

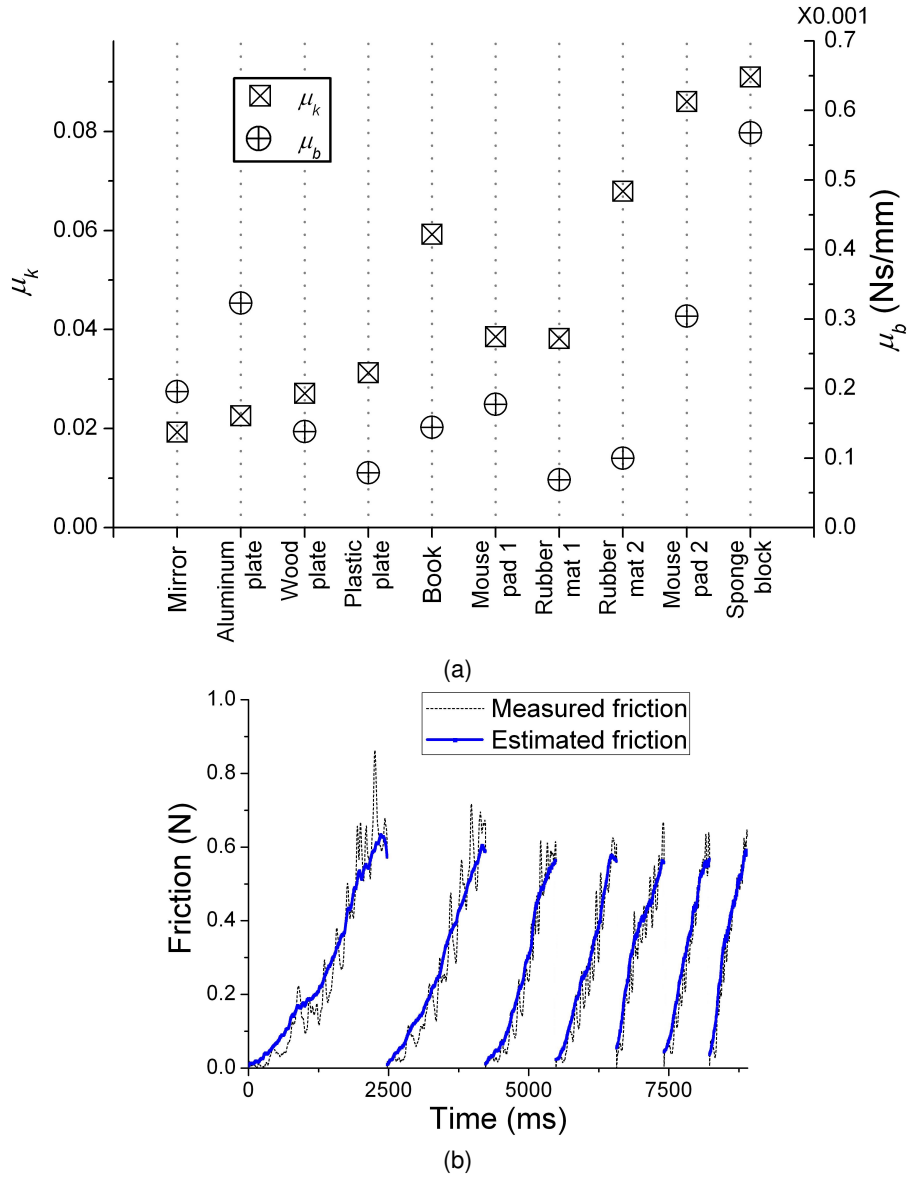


Fig. 4.6 Identification results of the ball bearing friction. (a) Identified friction parameters for ten real objects. The objects are sorted in the decreasing order of stiffness. (b) Comparison of the measured and estimated frictions for rubber mat 1.

of friction models). More complex models such as the LuGre model [30], Leuven model [97], Elasto-plastic model [32], and Generalized Maxwell-slip model [2] may show better

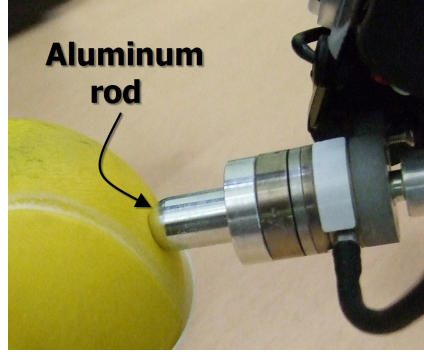


Fig. 4.7 Aluminum rod tool tip.

performance. Their focuses, however, were on the friction of mechanical systems that usually consist of hard materials. For deformable objects, their performances have not been verified and may not be quite different from that of the Dahl model. We confirmed by empirical identification test that more complex models significantly increased the complexity of the identification process without much performance increment.

The Dahl model is expressed by the differential equation:

$$\frac{df_{rd}^t}{dx^t} = \sigma \left(1 - \frac{f_{rd}^t}{f_c} \text{sgn}(v^t) \right)^\alpha, \quad (4.12)$$

where f_{rd}^t is friction magnitude derived by the Dahl model, x^t is the displacement of the tip along the tangential direction, σ is the stiffness coefficient for tangential displacement, α defines the shape of the tangential displacement-force curve, and f_c is a Coulomb friction force level that can be expressed by

$$f_c = \mu_k f_r^n, \quad (4.13)$$

where μ_k is the Coulomb friction coefficient. We take $\alpha = 1$ in this article, which is widely used value for α in the literatures [79]. Then, the model has the time domain representation such that (adapted from [79])

$$f_{rd}^t(t+1) = f_c(t) \text{sgn}(v^t(t)) + (f_{rd}^t(t) - f_c(t) \text{sgn}(v^t(t))) e^{-\frac{\sigma}{f_c(t)} |x_i^t - x^t(t)|}, \quad (4.14)$$

where x_i^t is an initial relative displacement between the two contacting objects, which is reset to $x^t(t)$ when the velocity is zero. Since the original Dahl model does not consider the viscous friction, we add the viscous friction term in our implementation:

$$f_r^t(t) = f_{rd}^t(t) + \mu_b v^t(t), \quad (4.15)$$

where μ_b is a viscous friction coefficient.

The three parameters, $\{\mu_k, \sigma, \mu_b\}$, are identified in an off-line process as follows. The first step is dedicated to measuring true data for $\{x^t(t), v^t(t), f_r^n(t)\}$, and corresponding true friction $f_r^t(t)$. Note that we use the same hardware setup to the rendering for the data acquisition, which increases the usability. To measure the true data, the geometry information, especially the data of true surface normal vector, \mathbf{u}^n , is necessary. We manually construct a geometric model along small path on the real object. The positions of the points on an object surface are densely sampled by lightly tapping on the object with the PHANToM. Contacts are detected using our collision detection algorithm. During this procedure, the up-down movements of the tool tip in the height direction are actively controlled to remain constant. Thus, only horizontal movements (left-right and front-back) are allowed, resulting in a 2D scanning line. Gaps between the sampled points are interpolated using the clamped cubic splines. To find the true normals, we search the nearest point on an object surface represented by the spline model from the position of the tool tip. The vector from the tool tip to the closest point are regarded as a true normal.

After the geometry is measured, we gather 4-tuples of true data, $\{x^t(t), v^t(t), f_r^n(t), f_r^t(t)\}$, using a manual stroking on the modeled path. We do not apply an automatic controlled data collection procedure. In our haptic AR system we use a PHANToM model with a gimbal encoder to allow for natural user interaction. The PHANToM, however, has no actuators for orientation control, which makes automatic data collection infeasible. While stroking, the measures true data is pass to a parameter identification module.

In the parameter identification module, we apply “divide and conquer” approach to deal with the nonlinearity of the model and facilitate the procedure. In general, the friction response of the presliding regime (when the velocity is near to zero) is quite different from

that of the sliding regime (when the velocity is large), and thus two regimes should be described differently in a friction model. The Dahl model deals with this difference by observing the tangential displacement of the tip, $|x_i^t - x^t(t)|$ in (4.14). For example, as $|x_i^t - x^t(t)|$ becomes larger, the second term of (4.14) converges to zero, and the estimated friction force converges to the simple Coulomb friction depicted in (4.13). On the other hand, the response is dominated by the second term in (4.14) when the displacement is near to zero, and σ determines the slope of the tangential force vs. tangential displacement curve at the origin. This characteristic of the model enables to divide the nonlinear form of the model into two linear forms in terms of the operating regime.

In our implementation, each 4-tuple true data is classified into two bins; data with large tangential displacement and data with near-zero tangential displacement. We use data in $|x_i^t - x^t(t)| > 3$ mm for the former, and $0.5 \text{ mm} > |x_i^t - x^t(t)| > 0$ mm for the latter. The parameters, μ_k and μ_b are identified using the first bin via a linear identification technique, i.e., linear recursive least-square algorithm [47]. Using the second data bin, the slope of the tangential force vs. tangential displacement curve at the origin, σ , is identified via the same linear identification technique. While the direct nonlinear identification generally needs more input data and is less stable than linear identification, this “divide and conquer” approach for the friction model identification can be more suitable for our haptic AR system.

The data gathering procedure lasted until the model parameters are converged. We decide that the parameter estimates have converged if the gradients of all parameter estimates become smaller than predefined thresholds. This identification procedure takes 10–20 seconds in our haptic AR system.

If the solid rod tip is used, the parameter identification procedure is an off-line processing necessary for each real object in our framework. This may reduce the usability of the system, but 10–20 seconds of preprocessing can be compared to using markers on real objects for the registration in visual AR. The friction parameters of each object in an environment are identified prior to the main interaction using the haptic interface. The parameters are used during the user’s interaction in the environment using the same hardware. We guess this preprocess is acceptable in most applications.

In order to validate our model acquisition algorithm, we compared the measured true friction with the estimated one from the identified model for the four objects shown in Fig. 4.3. Fig. 4.8 shows the results on the foam ball as an example. Note that the absolute magnitude of friction in Fig. 4.8 is much higher than that with the ball bearing in Fig. 4.6b (compare the y-axis scale of the two graphs). Since higher absolute magnitude on the friction produces larger error on the direction estimation under the same error rate, the friction should be more accurately estimated in the second approach in order to fulfill the performance requirement.

We gathered the true and estimated friction forces by manually stroking the four objects with various velocities and normal forces. The true values were derived by the same procedure used in the model identification procedure. Then, we calculated the ratio of the estimation error over the true value for each data and averaged them. The averaged ratios of the error were 8%, 7%, 10%, and 15% for the sponge cut, foam ball, rubber ball, and silicone rest, respectively, which indicate that the Dahl friction model moderately explained the friction responses, but with some errors. The silicone rest showed the worst performance. Small stick-slip behavior was frequently observed on the silicone rest, which was not properly captured by the Dahl model. In the performance evaluation section (Sec. 4.4.3), the effect of these errors on the estimation of the direction is investigated through an experiment with real samples.

4.4.2 Rendering

During rendering, $\mathbf{f}_r^t(t)$ is computed by decomposing it to

$$\mathbf{f}_r^t(t) = -f_r^t(t)\mathbf{u}^t(t), \quad (4.16)$$

where $f_r^t(t)$ is the friction magnitude estimated by the above two approaches and $\mathbf{u}^t(t)$ is a tangent vector at $\mathbf{p}(t)$ for the friction direction (see Fig. 4.1b). We first estimate $\mathbf{u}^t(t)$ as follows. Projecting $\Delta\mathbf{p}(t) = \mathbf{p}(t) - \mathbf{p}(t-1)$ onto \mathbf{u}^n gives

$$\Delta\mathbf{p}^n(t) = \{\Delta\mathbf{p}(t) \cdot \mathbf{u}^n(t)\}\mathbf{u}^n(t). \quad (4.17)$$

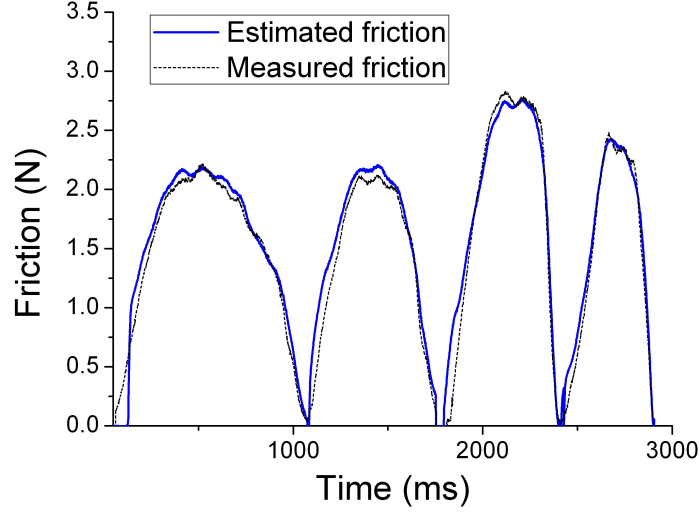


Fig. 4.8 Identification results of the friction between solid rod tool tip and the foam ball.

Then, the tangential component of $\Delta \mathbf{p}(t)$ is derived by

$$\Delta \mathbf{p}^t(t) = \Delta \mathbf{p}(t) - \Delta \mathbf{p}^n(t). \quad (4.18)$$

We approximate \mathbf{u}^t as the direction of $\Delta \mathbf{p}^t(t)$ such that

$$\mathbf{u}^t(t) = \frac{\Delta \mathbf{p}^t(t)}{|\Delta \mathbf{p}^t(t)|}. \quad (4.19)$$

Here, to compute (4.19), the current normal vector $\mathbf{u}^n(t)$ must be used in (4.17). Since $\mathbf{u}^n(t)$ is unknown at this step, we replace it as $\mathbf{u}^n(t) = \mathbf{u}^n(t-1)$. This simple prediction leads to quite good performance since the change rate of true $\mathbf{u}^n(t)$ is much slow compared to the very short rendering period (1 ms in our system). Then, $f_r^t(t)$ can be calculated by (4.11) or (4.15), where

$$f_r^n(t) = \mathbf{f}_r(t) \cdot \mathbf{u}^n(t), \quad v^t(t) = \mathbf{v}(t) \cdot \mathbf{u}^t(t). \quad (4.20)$$

In this equation, $\mathbf{u}^n(t)$ is replaced with $\mathbf{u}^n(t-1)$ again, and the velocity $\mathbf{v}(t)$ of the tool tip is derived by the first-order adaptive windowing filter [53]. As a result, we can determine $\mathbf{f}_r^t(t)$ in (4.16), and thus $\mathbf{u}^n(t)$ in (4.10). In our implementation, a second-order Butter-

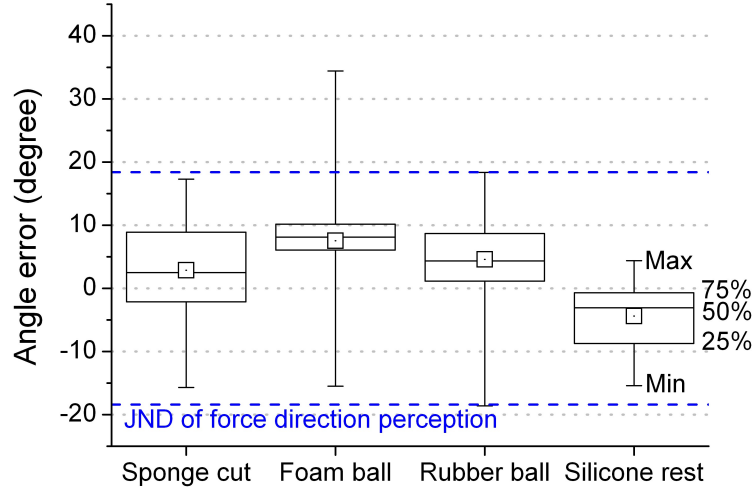


Fig. 4.9 Distributions of the deformation direction estimation errors for each object using the ball bearing tool tip. Small squares represent the mean values.

worth low-pass filter with a 70-Hz cutoff frequency was applied to the normal estimates to suppress the effect of force sensor noises.

4.4.3 Performance Evaluation

We performed experiments to assess the accuracy of deformation direction estimation, $\mathbf{u}^n(t)$ in (4.10), with the four real objects shown in Fig. 4.3. The accuracy was then compared with the performance requirement defined in Section 4.2.

Approach Using Ball Bearing Tool Tip

To obtain the accuracy of estimates, the geometric models of the real objects were necessary. We used the same procedure for the real geometry modeling described in Section 4.4.1.

Then, the experimenter scanned object surfaces 80 times per object from right to left. The lateral scanning velocity varied in 50–200 mm/s, and the normal force varied in 2–6 N. The scanning length ranged in 50–100 mm depending on the object. To find the true normals, we searched the nearest point on an object surface represented by the spline model from the position of the tool tip. The vector from the tool tip to the closest point was regarded as

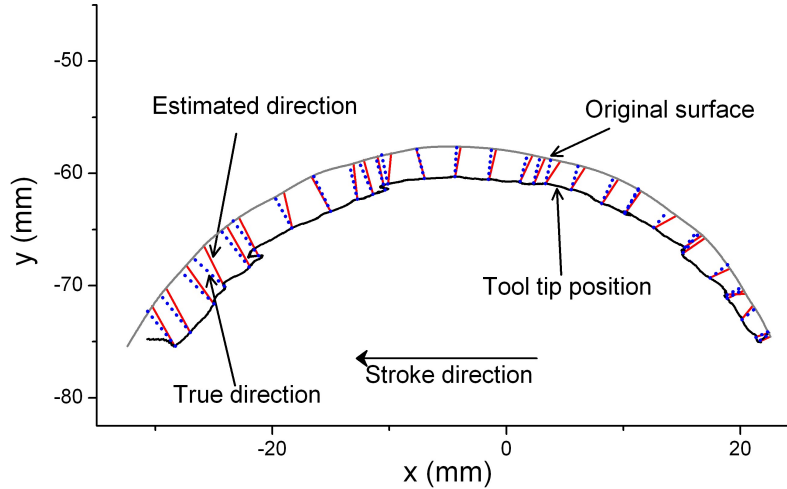


Fig. 4.10 Estimated and true deformation directions collected from the foam ball using the ball bearing tool tip.

a true normal. An angle difference between this true normal and an estimated normal was used as an error metric.

The error distributions of deformation direction estimation are shown in Fig. 4.9 for each object. To see the perceptual significance of the errors, we compared them with the human discriminability of force direction reported in Section 4.2. The JND is 18.4° , which is indicated by blue dashed lines in Fig. 4.9. It can be seen that most estimation errors were well below the JND, demonstrating that our algorithm for deformation direction estimation has appropriate performance in terms of perception.

As an example, Fig. 4.10 shows the true and estimated deformation directions for the foam ball. The estimated normals of the foam ball were biased from the true normals in one direction. This resulted from the use of constant friction parameters regardless of real objects. If a friction value used for normal estimation is smaller than the true friction, the estimated normal lags behind the true normal. To see this, one can reduce the magnitude of \mathbf{f}_r^t in Fig. 4.1b, find $\mathbf{f}_r - \mathbf{f}_r^t$, and then plug this in (4.10). The sponge cut, foam ball, and rubber ball corresponded to this case. Otherwise, the estimated normal leads the true normal, on the contrary to Fig. 4.10. An example is the silicone rest that had a negative

mean in Fig. 4.9. Despite these biased estimates, the error ranges were bounded within the JND of force direction discrimination.

Approach Using Solid Rod Tool Tip

The process and method of the experiment were similar to the process described in the previous section, except for the separate parameter identification for each object. The error distributions of deformation direction estimation for the four objects are shown in Fig. 4.11. The overall amount of the estimation errors was not much different from the result of the approach using the ball bearing (compare the results of Fig. 4.11 with Fig. 4.9). This is remarkable since the second approach suffers from higher absolute magnitude of friction and larger averaged error on friction estimation (7% for the first approach and 10 % for the second approach). It is due to the separate identification of the model parameters for each object. The advantage of the separate identification can be clearly seen in Fig. 4.11, where no bias in the estimated normal is observed for the all objects. We also compared the error with the JND of force direction that is indicated by blue dashed lines in the figure. Most estimation errors were well below the JND even for the silicone rest, demonstrating that the second approach also fulfills the performance requirement.

We also tested our algorithm on very sticky object that shows large stick-slip behavior in their friction response. Large error was observed in the direction estimation, and the abrupt changes in the normal direction due to the error results in unstable response of the haptic interface. More sophisticated friction algorithm or another new approach is needed to deal with such imperfection.

4.5 Estimation of Deformation Displacement

The next step is to estimate the displacement of a tool tip, $x(t)$, to account for the amount of deformation. A straightforward way to determine $\mathbf{p}_c(t)$ without the geometry model of a real object is a recursive estimation using $\mathbf{u}^t(t)$ obtained in (4.19), such that

$$\mathbf{p}_c(t) = \mathbf{p}_c(t-1) + \{\Delta\mathbf{p}(t) \cdot \mathbf{u}^t(t)\}\mathbf{u}^t(t) \quad (4.21)$$

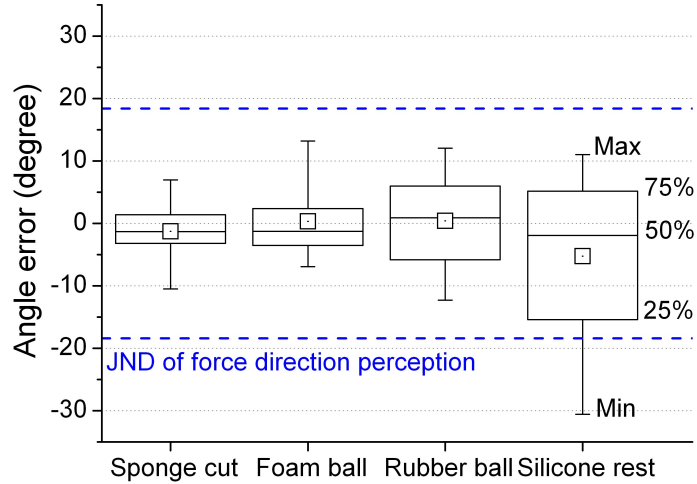


Fig. 4.11 Distributions of the deformation direction estimation errors using the solid rod tool tip.

where $\mathbf{p}_c(0) = \mathbf{p}(0)$ (also see Fig. 4.1b). An advantage of this method is no need of preprocessing for the geometry or elasticity of the real object. However, an estimate of $\mathbf{u}^n(t)$ needed to compute $\mathbf{u}^t(t)$ contains errors, which is accumulated in the recursive estimation. Thus, $\mathbf{p}_c(t)$ tends to diverge over time. The accumulated error cannot be canceled off in our framework due to the absence of true data on the surface normal.

Instead, we identify and simulate a dynamics response of a real object and use it to find the deformation displacement. In general, large-scale contact simulation techniques for deformable objects e.g., those described in [78, 52, 77] are necessary to explain the deformation behaviors of a broader class of real objects with high fidelity. However, they require an exhaustive identification procedure with a special hardware setup and a large amount of preprocessing, and real-time haptic simulation of such models is a quite challenging issue. An alternative is to use a constant dynamics model for different contact locations. The assumption of homogeneity made in Section 4.1 allows this simpler approach. We adapted a model frequently used for impedance control in robotics [33].

4.5.1 Contact Dynamics Model Acquisition

The most common model is the Kelvin-Voigt model that uses the dynamics of a linear spring-damper system [35]. The model, however, exhibits physical and energetic inconsistencies in its behavior such as force discontinuity at a contact and negative force prediction at a load removal [41]. We confirmed by implementation that these inconsistencies lead to large incorrect estimations of $x(t)$ at the instants of impact and load removal. Moreover, this linear model is not suitable for describing large deformations in rubber-like real objects that exhibit apparently nonlinear impedances.

In our current haptic AR system, we use the nonlinear Hunt-Crossley model [50]. This model can adequately account for the nonlinear viscoelastic contact dynamics of a deformable object without the problems present in the Kelvin-Voigt model [41, 11]. It has been adopted in several recent studies in robotics [80, 31, 44]. In particular, [105] confirmed by an experimental evaluation of seven dynamics models that the Hunt-Crossley model was the best to describe the properties of soft deformable object such as a phantom tissue made of silicone. The Hunt-Crossley model has a form of

$$f_r^n(t) = K_e \{x(t)\}^m + B_e \{x(t)\}^m \dot{x}(t), \quad (4.22)$$

where K_e and B_e are the stiffness and damping parameters of an object, respectively, and m is a constant exponent (usually between 1 and 2) that depends on the material and geometric properties of the object and a contactor. There exist more complex nonlinear dynamics models with higher modeling power such as the Hammerstein model [51] and the quasi-linear model [34], but identification of their parameters requires exhaustive data collection and fitting procedures. In contrast, the Hunt-Crossley model has reasonably high accuracy, and its parameter identification can be fairly quick, as demonstrated in Section 4.5.3. Therefore, it can be an adequate choice for haptic AR.

To identify the parameters of the Hunt-Crossley model, we use an algorithm proposed by Haddadi and Hashtrudi-Zaad [44]. In their method, the Hunt-Crossley model is linearized under a reasonable assumption, and then the parameters are found by the recursive least square estimation. To obtain reliable parameter estimates using the method, a large amount

of true data for $\{x(t), \dot{x}(t), f_r^n(t)\}$ is still necessary. For this, a user repeatedly pushes the haptic tool to a real object and pulls it back until the model parameters are converged. Lateral movements are prohibited during this process to obtain accurate displacement data. We decide that the parameter estimates have converged if the gradients of all parameter estimates become smaller than predefined thresholds. This identification procedure takes 10–20 seconds in our system.

A critical factor affecting the performance of deformation displacement estimation is how well the Hunt-Crossley model used in our framework predicts the dynamic responses of real objects. Even though the literature has agreed that the Hunt-Crossley model has quite acceptable performance [105, 80, 31], we needed to reconfirm it in our implementation for haptic AR. Thus, we performed model validation tests with the four real samples. The results presented in Fig. 4.12 demonstrate that the model well describes the nonlinear responses of the four real objects, with slight errors in viscosity estimation (see differences in the amounts of hysteresis). The average prediction error was approximately 12% of the measured force value. Most evident discrepancies between the measured and simulated curves were observed during contact relaxations. With real objects, since no force data can be collected after a contact is released, such data could not be included for model fitting. This appears to a major reason for the modeling errors. We will discuss the effect of the errors on displacement estimation in the performance evaluation section (Section 4.5.3).

4.5.2 Rendering

During haptic rendering, the estimated parameters are used to find the deformation displacement by

$$x(t) = \left\{ \frac{f_r^n(t)}{K_e + B_e \dot{x}(t)} \right\}^{\frac{1}{m}}, \quad (4.23)$$

where $f_r^n(t)$ and $\dot{x}(t)$ are already found in (4.20). In implementation, a Butterworth low-pass filter with a 60 Hz cut-off frequency was applied on $f_r^n(t)$ to suppress the effect of sensor noises.

The parameter identification of the Hunt-Crossley model is an off-line processing necessary for each real object in our framework. To remove this off-line procedure, we tested

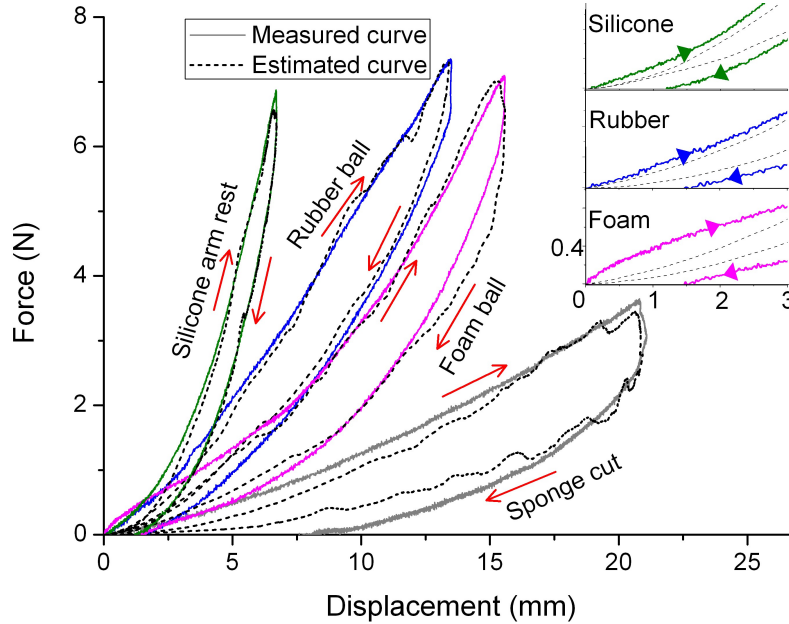


Fig. 4.12 Measured and estimated displacement-force curves of the four real objects. Insets are magnified graphs around zero displacement for a detailed view.

various on-line parameter estimation techniques both for the parametric and non-parametric models. However, they commonly require a large number of samples well distributed in $\{x(t), \dot{x}(t), f_r^n(t)\}$ to obtain reliable parameter estimates, but it turned out that collecting such data is impossible when a user freely interacts with a real object. As a result, all real-time estimation techniques we tried showed poor performance for estimating $x(t)$, thus resulted in rather erratic force rendering. The current identification procedure is the least to be included for convincing displacement estimation.

4.5.3 Performance Evaluation

We experimentally estimated the deformation displacements using the four real objects and the two deformation direction estimation methods. The procedures to obtain the geometric models of the real objects and the way of stroking the object surfaces were the same as those described in Section 4.4.1. The strokes were repeated 20 times for each object and for

each direction estimation method. The true displacement was regarded as the distance from the tool tip to the nearest point on the object surface. The displacement error was defined as the difference between the true and estimated displacements.

The overall distributions of the displacement estimation errors are shown in Fig. 4.13. In addition, Fig. 4.14 depicts reconstructed surfaces using the estimated displacements in comparison to the non-deformed object surfaces. In Fig. 4.13, 50% of the estimation errors were within 1 mm and the most errors were less than 2 mm both for the two direction estimation method, except for the sponge cut. Even for the sponge cut, nearly 70% of the errors stayed below 2 mm. We also computed the ratio of the displacement estimation errors to the true displacements. When the ball-bearing-tip direction estimation method was used, the averages for the sponge cut, foam ball, rubber ball, and silicone arm rest were 16.31%, 20.86%, 15.05%, and 32.84%, respectively, and when the off-line friction identification method was used, they were 27.34%, 17.94%, 14.93%, and 16.62%. Their medians were 14.31%, 13.09%, 10.25%, and 12.68% for the ball-bearing-tip method, and 17.73%, 14.45%, 11.03%, and 10.5 % for the off-line friction identification method. To test the significance of the error, the error ratios were compared to the Weber fraction of stiffness perception as mentioned in Section 4.2. The Weber fraction ranged from 0.08 to 0.12 in the literatures, which is slightly smaller than the measured error ratios. This indicates that the stiffness error due to the displacement error can slightly be perceivable to a user.

But we speculate that this error is perceptually acceptable due to the following two reasons. First, such small difference between the error ratio and the Weber fraction is negligible in practice considering that the Weber fraction was measured in a laboratory with extremely attentive subjects. Second, Figures 4.14a–4.14d suggest that most large errors occurred when contacts were released (see inside the red circles in the figures). This can be explained based on the complex relaxation characteristics of the real objects. In Fig. 4.12, the sponge cut exhibited very slow relaxation at the contact release (note zero force point at a positive displacement). The other objects also showed such patterns (see the insets in Fig. 4.12). These plastic-like responses cannot be properly caught by the Hunt-Crossley model. In contrast, the displacement estimation errors during contact initiation and stroking

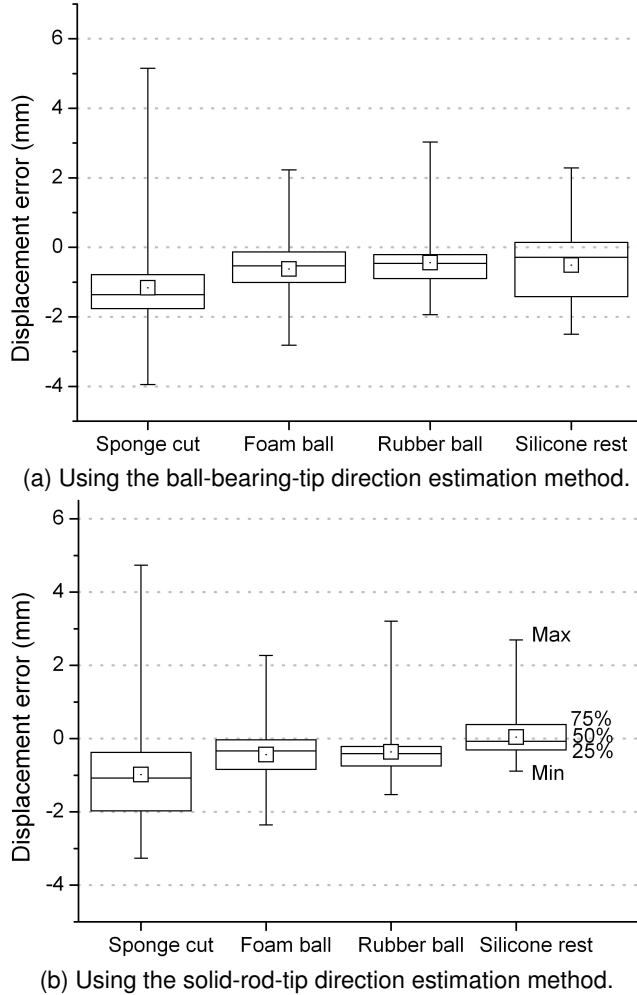


Fig. 4.13 Distribution of the deformation displacement estimation errors for each object and for each deformation direction estimation method.

were significantly smaller. This is also reflected in the medians of the estimation errors all smaller than the averages. It is well known that the human relies more on the rate of initial force changes for hardness perception [70], and stimuli during contact releases have less implications. Thus, we conjecture that the displacement estimation errors are perceptually insignificant, which is also confirmed in our psychophysical experiment in Section 4.7.

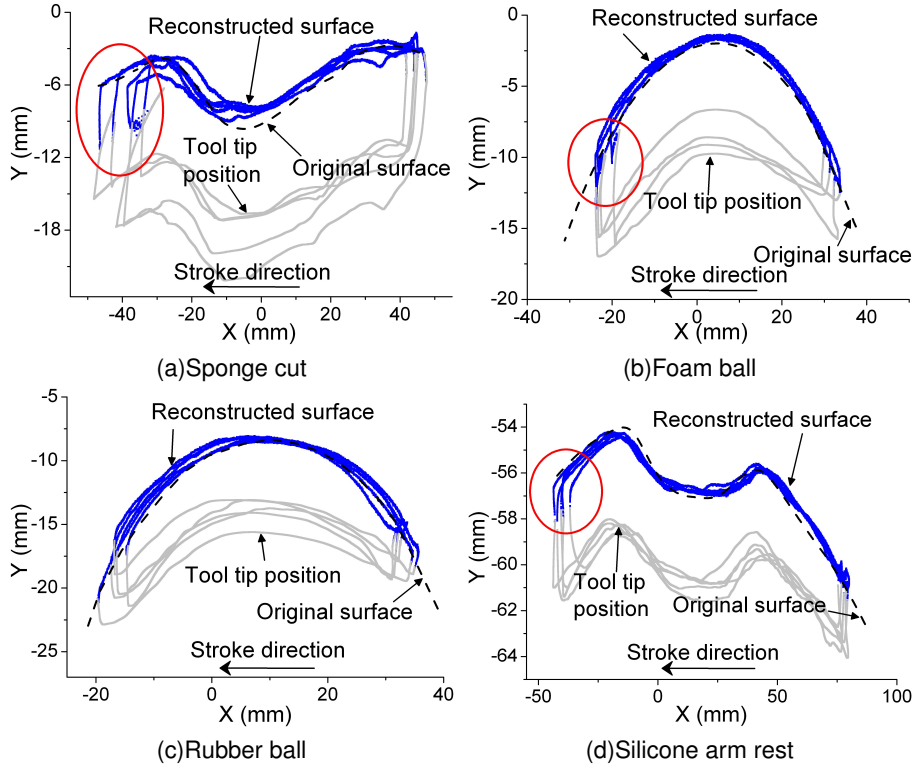


Fig. 4.14 Tool tip positions and object surfaces reconstructed using the estimated displacements. Object surfaces without deformation obtained in preprocessing are also shown in the dashed lines.

4.6 Force Control

Using the algorithms presented so far, the desired device force $\tilde{\mathbf{f}}_d(t)$ can be determined by (4.4). The last step is to control the force produced by the haptic interface, $\mathbf{f}_d(t)$, to faithfully follow $\tilde{\mathbf{f}}_d(t)$.

4.6.1 Algorithm

We use a closed-loop force control slightly modified from method described in Chapter 3.3 to deal with the 3D interaction, such that

$$\mathbf{f}_c(t) = \mathbf{f}_c(t-1) + K_p \mathbf{f}_e(t) + K_d \frac{d\mathbf{f}_e(t)}{dt}, \quad (4.24)$$

where $\mathbf{f}_c(t)$ is a force command to be sent to the haptic interface, $\mathbf{f}_e(t) = \tilde{\mathbf{f}}_d(t) - \mathbf{f}_d(t)$ is a force rendering error, and K_p and K_d are proportional and derivative gains, respectively. To measure $\mathbf{f}_d(t)$, an additional force sensor needs to be installed to the haptic interface, e.g. between the gimbal encoder of the PHANToM and the grip of the stylus in Fig. 4.2. Instead of adding another expensive instrument, we use a heuristic observer: $\mathbf{f}_d(t) = \mathbf{f}_c(t - 1)$. Due to the fast sampling rate, the observer is enough for stiffness modulation, as demonstrated in the previous chapter.

We also consider the structural stiffness of a haptic interface for force control. The haptic interface is usually assumed to be ideally rigid for virtual object rendering. In reality, the joints and links of the haptic interface deform, and the amount of deformation is expressed by the structural stiffness [95]. The device deformation cannot be seen by the encoders at the joints, and this causes errors in the measurement of the tool position. The position sensing error increases with device-exerting force, and this can be an important error source for stiffness rendering. Specifically, the true position of the tool $\mathbf{p}(t)$ in a steady state is

$$\mathbf{p}(t) = \mathbf{p}_s(t) + \frac{\mathbf{f}_d(t)}{k_s}, \quad (4.25)$$

where $\mathbf{p}_s(t)$ is the tool tip position computed from the joint encoders and k_s is the structural stiffness of the haptic interface. $\mathbf{p}_e(t) = \mathbf{f}_d(t)/k_s$ corresponds to the position sensing error due to the structural stiffness. We use this $\mathbf{p}(t)$ for all equations presented in the previous sections.

The significance of $\mathbf{p}_e(t)$ is often neglected in usual haptic rendering. However, the error can be quite large and problematic in cases where exact displacement information is necessary. For example, the nominal structural stiffness of the PHANToM 1.5 High Force model is 3.5 N/mm, and its maximum force output is 37.5 N. Thus, this PHANToM may produce nearly 1 cm errors in position measurements, which can be quite significant for stiffness rendering.

We estimated the structural stiffness as follows. When a user taps on a virtual wall with desired stiffness \tilde{k} , the actual displacement is

$$x(t) = x_s(t) + \frac{\tilde{k}x_s(t)}{k_s}. \quad (4.26)$$

This model was used to estimate k_s . While tapping on virtual walls placed at various positions and orientations, we collected data of $x(t)$ and $x_s(t)$. The true displacement $x(t)$ can be measured using an external displacement sensor. We used a LVDT (linear variable differential transformer) with an accuracy of $30 \mu\text{m}$. k_s was then estimated by fitting the model to the collected data (2.537 N/mm for the PHANToM 1.5 High Force).

For simplicity, our current algorithm uses a constant value for the structural stiffness. In general, the structural stiffness depends on the position and orientation of the device tip, and it should be expressed by a stiffness field in the 6D configuration space. Building such a stiffness field corresponds to an extensive calibration of a haptic interface, and we leave it as a future work. We nonetheless note that using the constant structural stiffness still provides convincing stiffness modulation in our current haptic AR system.

4.6.2 Performance Evaluation

The physical performance of the force control algorithm was tested with the four real objects. We measured the forces rendered to the user's hand while stroking the four real objects with five desired stiffness values (0.2, 0.7, 1.2, 1.7, and 2.2 N/mm). Recall that the structural stiffness of the PHANToM 1.5 High Force was measured to be 2.537 N/mm. The object stiffness (see Fig. 4.3 for representative values) added by the structural stiffness is the maximum desired stiffness for each object. Due to the absence of additional force sensor at the grip, we used (4.1) with $\mathbf{f}_d(t) = \mathbf{f}_c(t - 1)$ to estimate $\mathbf{f}_h(t)$. The gains of the PD controller were tuned using the Ziegler-Nichols method [108] followed by fine tuning.

The measured hand forces with respect to the displacements are presented in Fig. 4.15. The figure shows scatter plots, thus the stability of rendering can be assessed from the variance of the points. In the graph, a softer object showed worse stability, which is to be expected. In general, a softer object shows smaller response forces, which inevitably decreases the signal-to-noise ratio in the estimates of deformation direction and displacement. As the estimates become noisier, rendering stability is adversely affected.

In order to clearly measure the range of achievable stiffness, we examined the range by a real stroking experiment on the four real objects and two haptic interfaces, PHANToM

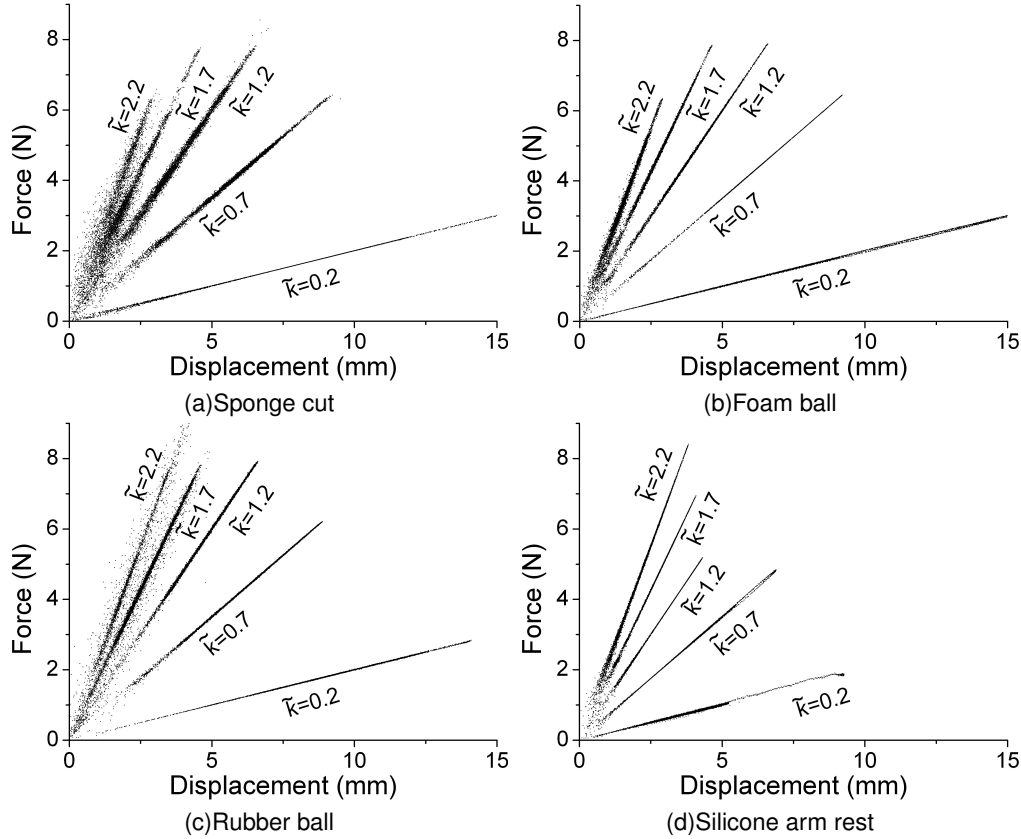


Fig. 4.15 Displacement-force curves. Displacements for plotting are derived from the displacement estimation algorithm.

Premium 1.0 and PHANToM Premium 1.5 high force model. A subject repeatedly stroked the surface of the object. The maximum pressing force was controlled to be lower than 4 N by visually displaying a warning signal if the pressing force exceeded 4 N. The PD control gains were tuned separately for each object and haptic interface. The desired stiffness, $\tilde{k}(t)$, was systematically changed; it was increased until unstable oscillations began, and decreased until the lower bound was met. The results are represented in the box plots in Fig. 4.16.

The circled crosses in the figure mark the representative stiffness of the corresponding real objects. Overall, the measured range of stably renderable desired stiffness allows the haptic AR system to modulate the stiffness of a real object to feel very softer or quite

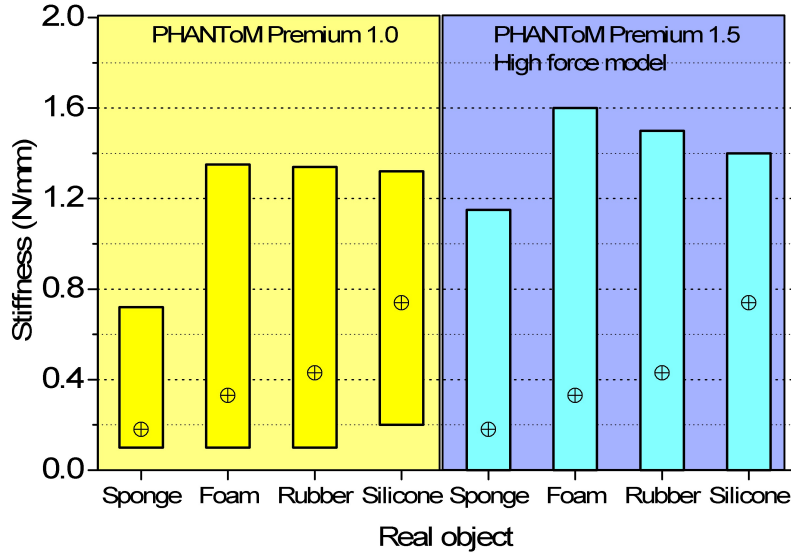


Fig. 4.16 Ranges of stiffness values stably modulated in our 3D stiffness modulation system.

harder. We note that the ranges in our previous system for 1D interaction were much wider in Fig. 3.10 than the range for 3D interaction in Fig. 4.16. An important difference is that the algorithm for 3D interaction takes into account the position measurement errors due to the structural stiffness of a haptic interface, while the algorithm for 1D interaction did not (see Section 3.3 for the 1D case). The actually rendered stiffness values in Section 3.3 can be much lower than the reported numbers. For example, in Fig. 3.10, the upper bounds of stably rendered stiffness using the PHANToM 1.5 high force model for the four real objects were about 10 N/mm with 4 N of pressing force. If we take into account the structural stiffness of the PHANToM 1.5 high force model ($= 2.537$ N/mm), the position sensing error would be as large as 1.576 mm ($= 4/2.537$) according to (4.25). Then, the true displacement becomes 1.976 mm ($= 4/10+1.576$). Thus, the actually rendered stiffness is 2.024 N/mm ($= 4/1.976$), which is not very different from the results reported in Fig. 4.16.

Nevertheless, the upper bounds of the ranges are still lower than the 1D case even if the structural stiffness is considered. It is beneficial to examine the reason of this performance degrade for further improvement. In the 3D stiffness modulation, most unstable responses

were observed when the displacement and the reaction force were quite small (see large variances of the points around the origins of each graph in Fig. 4.15), which often determined the upper bound of the range. This is partially due to our displacement estimation method. Our method utilizes the inverse of the Hunt-Crossley model to estimate the displacement as depicted in Sec. 4.5. Due to the exponential part of the model (the exponent ranges from 1 to 2 in general), small changes in the reaction force, $f_r^n(t)$, make relatively large changes in the displacement estimate when the displacement is small. Refer to Fig. 4.12 for example. For the curve of the sponge cut in the figure, the force increment from 0 to 0.5 N increases the displacement estimate from 0 to 5 mm when pushing. This results in noise in the force measurements to be amplified in the displacement estimates when the magnitude of the force measurements are relatively small.

From this fact, we can infer that the exponent parameter of the Hunt-Crossley model is one of the main factors, which determines the range. The larger exponent value usually decreases the stability at the small displacement. For example, the exponent parameter of the model for the sponge cut is the highest (= 2.1) among the four objects (the exponent parameters for other objects ranged from 1.3 to 1.7). The results in Fig. 4.16 confirm that the stably rendered range for the sponge cut was the narrowest among the four objects. In addition, little difference between the results of the two haptic interfaces is also the consequence of this characteristic of our algorithm. The noise amplification dominated the difference of the performances of the haptic interfaces. Note that we already apply a low-pass filter to the force measurement to suppress the noise (see Sec. 4.5.3). But further improvement would be possible by applying an adaptive low-pass filter that changes the cut-off frequency according to the magnitude of the force measurement and the value of the exponent.

We also tested our AR system on largely inhomogeneous real objects, e.g., the human arm. As expected, large errors were observed in the displacement estimation. The Hunt-Crossley model is unsuitable to accommodate complex dynamics such as the bone under the skin and the stiffness changes depending on contact locations. In addition, real objects with very complex geometry can lead to unstable force rendering. For an object surface

with high curvature variations, significant instability was observed when the tool tip passed through ridges and valleys on the surface. It is due to the PHANToM that exhibits severe instability for force commands containing abrupt directional changes [25].

4.7 Psychophysical Experiment

In this section, we perceptually evaluate our 3D stiffness modulation system through a psychophysical experiment. Analogous to the psychophysical experiment for 1D haptic AR (Section 3.4), the experiment measured the Points of Subjective Equality (PSEs) of perceived stiffness altered by our system under various conditions, and compared them to desired stiffness values.

4.7.1 Methods

Apparatus

For a haptic interface, the experiment used a PHANToM 1.5 high force model instrumented with a NANO17 force sensor and a contactor assembly as depicted in Fig. 4.2. We used the ball bearing for the interaction tool tip and corresponding deformation direction estimation algorithm (see Section 4.4). As depicted in Section 4.4.3 and Section 4.4.3, deformation estimation performance using ball bearing tool tip is not quite different from, or a little bit inferior to that using solid tool tip, which would make a more challenging situation for our system to be assessed. A real object was placed in front of the PHANToM (see Fig. 4.17).

Subjects

Twelve subjects (S1 – S12; 19 – 30 years old with the average of 23.5) participated in the experiment, and were compensated for their help. All subjects were right-handed by self-report, and four of them were females. Six of them had participated in haptic perception experiments prior to the present experiment but were not experienced users of a force-feedback device. The other subjects had not been exposed to any haptic interfaces prior to the present experiment. No subject was informed of the goals of the experiment.

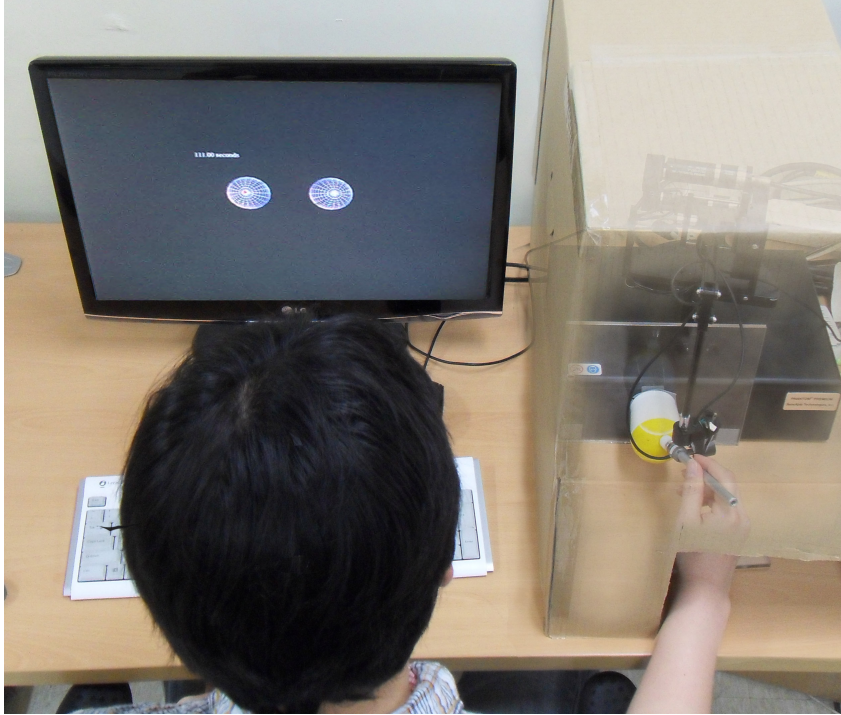


Fig. 4.17 Experimental environment. The blurred scene inside the paper box is for illustration, and was not seen by the subjects in the experiment. The haptic interface point and the wire-frame models for the two objects were visualized in 3D on the monitor in order to guide the subject's interaction. They were disappeared when the tool is in contact with one of the two objects.

Stimuli

In each trial, the subject was presented with reference and comparison stimuli in a pair. For the reference stimulus, a real object is placed on the 70 mm left of the origin position of the PHANToM, and its stiffness was modulated to be a desired value by our haptic AR system. For the comparison stimulus, a usual elastic virtual object that has the same shape to the reference object was placed on the 70 mm right from the origin position of the PHANToM and rendered by the PHANToM only. The subject was allowed to freely change the object to be felt in a trial. The task given to the subject was to feel both stimuli by poking, pressing,

and stroking and answer whether the comparison is harder than the reference.

In order for the subjects to use only the haptic cue, visual or auditory cues were tried to be precluded. A paper box, shown semi-transparently in Fig. 4.17, enclosed the PHANToM and a real object, eliminating any visual cues. Since the two comparing objects were also invisible, visual information of the location of the two objects and the tool tip was shown in the monitor for guiding the subject's interaction during the object change. A point representing the tool tip and two 3D objects having the same shape to the reference object were visually rendered as shown in Fig. 4.17. Wire-frame was chosen for the 3D objects rendering in order to prohibit the subject from being influenced by the visual surface texture of the 3D model. In addition, the visual information was disappeared when the contact is occurred in order to prevent the subject from judging the displacement by visual cue. Auditory cues were also precluded by an earplug worn by the subject.

Experimental Conditions

Two independent variables were defined. One was the kind of real objects used for a reference stimulus. The sponge cut (representative stiffness = 0.18 N/mm) and the foam ball (representative stiffness = 0.33 N/mm) were selected, representing real objects with low and medium stiffness values, respectively. The other variable was the target stiffness of a reference stimulus, i.e., the desired stiffness of a real object to be modulated by the haptic AR system. It was either 0.3 N/mm or 0.8 N/mm. The factorial combinations of the two independent variables led to four experimental conditions.

Procedures

For each experimental condition, the PSE of the reference stimuli against the comparison stimuli was estimated using the two-interval, forced-choice adaptive method [40]. In this method, each trial consisted of two intervals. One interval presented a reference stimulus, and the other a comparison stimulus. The two intervals were spatially ordered by placing the comparison stimulus on the right of the reference stimulus.

In each experimental condition, the initial stiffness of a comparison stimulus (virtual

object) was much higher (= 1.4 N/mm and 0.7 N/mm for the target stiffness 0.8 N/mm and 0.3 N/mm, respectively) than the desired stiffness of a reference stimulus for stiffness modulation. This stiffness was large enough to make the comparison stimulus obviously be felt harder than the reference stimulus. After each trial, the stiffness was decreased for every response of “The object on the right (comparison stimulus) felt harder” or increased for “The object on the right (the comparison stimulus) felt softer” with a predefined step size. The step size was initially set to 0.1 N/mm for fast convergence, and it was reduced to 0.02 N/mm after the first four reversals (a case where a decreasing stiffness sequence was changed to an increasing one, and vice versa) for accurate estimation. This procedure allows efficient estimation of a discrimination threshold corresponding to the 50% percentile point on a psychometric function. A session was terminated after 15 reversals. Most sessions consisted of 30–60 trials.

In each trial, the subject was presented with a pair of spatially ordered reference and comparison stimuli. The subject freely changed the stimulus one object to another in a trial. Since the current haptic AR framework only uses the displacement-force relationship for stiffness alteration, the effect of contact transient cues had to be minimized in the experiment. For this, the repeated tapping of the objects, which may produce tactile contact cues, was minimized by discarding and repeating a trial that has an object change with more than 3 new contacts. For the same reason, a trial that has a contact with high contact velocity (= 50 mm/sec) was also discarded and repeated. In order to include enough amount of lateral movement during stroking, a trial with less than 60 mm of lateral movement for each object was also discarded and repeated. After perceiving both stimuli, the subject was asked to enter one of two answers: “The object on the right felt harder” by pressing the ‘1’ key and “The object on the right felt softer” by pressing the ‘2’ key. This completed one trial, and a next trial followed immediately with the stiffness of comparison stimuli adjusted by a predetermined step size.

Prior to the experiment, each subject went through a training session to become familiar with the experimental procedures. In the training session, the aforementioned restrictions on the number of new contact, contact velocity, and lateral movement were strictly taught

through instructions and practice with warning signals showing the information regarding them on the monitor. The number of repeated trials due to the violation of the restrictions was about 5 per a condition for each subject in the main experiment. One experimental condition took 10 – 15 minutes to complete, and the whole experiment about 1 hour. The subjects were required to take a rest after finishing one experimental condition, and could take a break whenever needed.

Data Analysis

We explain the method used to compute the PSE in the stiffness of the comparison stimuli using Fig. 4.18. In the figure, the comparison stiffness changes of a subject in each trial is shown for the foam ball – 0.3 N/mm experimental condition. In each experimental condition, we recorded the stiffness values at which 15 response reversals occurred (e.g., the grey squares and circles in the figure). The stiffness values at the first three reversals (e.g., the grey square in the figure) were discarded due to the large step sizes. The mean of the stiffness values of the last 12 reversals was considered as the PSE of the experimental condition. The PSE computed in this way represents the stiffness of a comparison stimulus (virtual object) perceived to be equally stiff to the reference stimulus (real object with modulated stiffness).

4.7.2 Results

Fig. 4.19 shows the PSEs and the differences between the PSEs and the desired stiffness values of the reference stimuli, both averaged across the subjects for the four experimental conditions. The error bar represents the standard error. The results clearly show that the PSEs were very different from the stiffness values of the real objects (0.18 N/mm for the sponge and 0.33 N/mm for the rubber ball) and close to the desired stiffness values of stiffness modulation, demonstrating the effectiveness of our haptic AR system. However, the PSEs were slightly larger for ‘Sponge03’, and smaller for ‘Ball08’ and ‘Sponge08’ than the desired values, as magnified in Fig. 4.19b. This suggests that the real objects augmented by our haptic AR system felt differently from the desired stiffness to some degree.

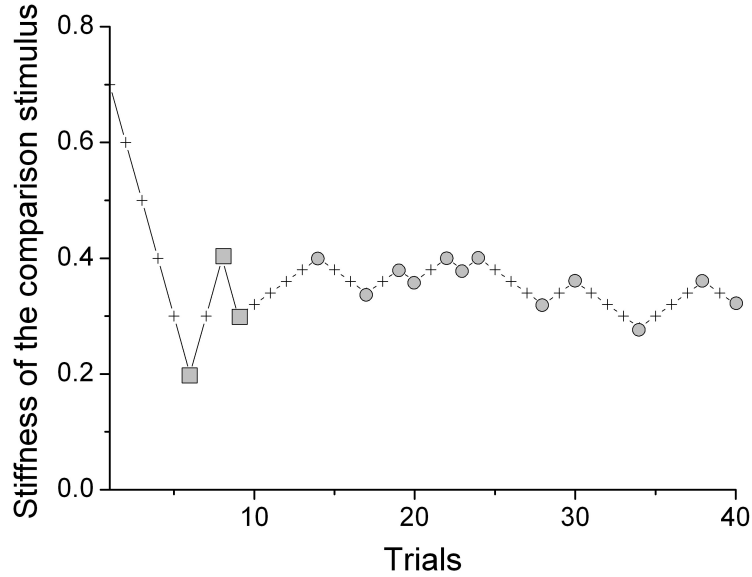


Fig. 4.18 Sample results of the foam ball - 0.3 N/mm condition.

Here again, to examine the significance of the PSE errors in terms of stiffness perception, the errors were compared to the difference thresholds (or difference limens; DLs) of stiffness perception. As aforementioned in Section 3.4.2, the difference thresholds were taken from [39], where the Weber fractions ranged from 0.08 – 0.12 for reference stiffness values in 0.3 – 1.2 N/mm. The corresponding Weber fractions for our reference stiffness values (0.3 and 0.8 N/mm) were both 0.09. Using the Weber fraction, we computed DLs and specified them in Fig. 4.19b. The PSE errors were smaller than or comparable to the corresponding DLs, except for ‘Sponge08.’ PSE error of ‘Sponge08’ was smaller than DL by 0.013 N/mm. We speculate that such small stiffness differences are negligible in practice considering that the DLs were measured in a laboratory with extremely attentive subjects. Thus, the stiffness modulation errors in our haptic AR system were marginally perceptible.

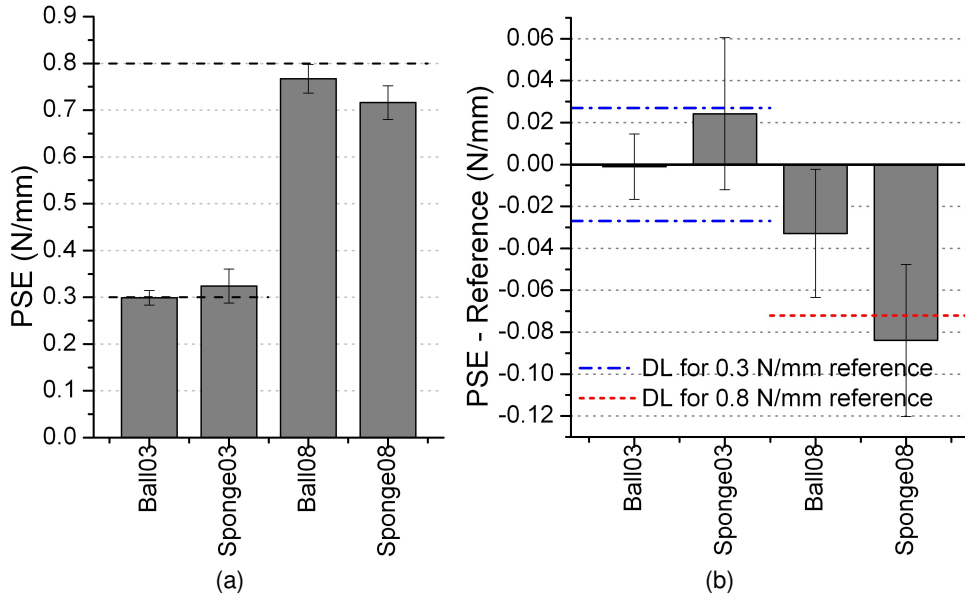


Fig. 4.19 Experimental results averaged across the subjects. (a) PSEs for the four conditions. (b) Differences between the PSEs in (a) and the stiffness values of the reference stimuli. The dotted-lines in (b) represents difference thresholds taken from [39]. Each experimental condition is denoted by combining the kind of a real object and the desired stiffness value for stiffness modulation used in the condition.

4.7.3 Discussion

The results in the previous section confirmed that our haptic AR system can adequately modulate the stiffness of a real object with perceptually negligible errors. But the stiffness modulation is still biased to some degree, and it is beneficial to identify the sources of the bias.

The main cue for the stiffness perception in this experiment was the displacement-force relation. Note that in our system the most significantly affecting computational module to this relation is the displacement estimation algorithm. In the displacement estimation algorithm, there is a systematic tendency on the actually rendered stiffness related to the model identification accuracy. We use Fig. 4.20 to explain this tendency. The figure shows three simulated displacement-force curves. Let the curve at the center be the measured true curve representing the exact response of the real object. Due to some reasons, our

algorithm incorrectly identifies the Hunt-Crossley model as depicted by “Underestimated curve” and “Overestimated curve” in the figure. Suppose that the reaction force at a certain time instance is 2 N. Our algorithm determines the displacement by finding a point in x-axis that corresponds to the measured reaction force in the identified curve. In the figure, if the curve is underestimated compared to the real curve (see “Underestimated curve” in the figure), the estimated displacement would be (c), which is larger than the true displacement, (b). If the desired stiffness to be rendered is set to the line named “Desired stiffness,” then our desired force calculation in (4.4) gives an additional force same as (e) for the desired force. Finally, actually rendered stiffness at the user’s hand would be the line named “Rendered stiffness (underestimate case)” at that time instance. If the identified model is overestimated (see “Overestimated curve”), similar induction gives us the actually rendered stiffness same as the line “Rendered stiffness (overestimate case).” In summary, the actually rendered stiffness would increase if the identified model is underestimated, or vice versa. This interpretation gives us a clue that explains the cause of the PSE error.

The PSE error is more significant on the sponge cut than the foam ball. Usually, the response of a soft sponge begins with a very gentle slope in displacement-force curve, but it exhibits a very sudden steep curve after a certain displacement. This characteristic is well shown in the dotted-curve in Fig. 4.21. Note that this graph includes much higher force range than the graph of the sponge cut in Fig. 4.12. When the sponge is compressed enough to have little air inside the body, the hard support plays a significant role on the response, and thus the stiffness increases rapidly. These two distinctive responses are not properly captured in one model. When identifying the Hunt-Crossley model, the system tries to fit both responses to one model, and the result exhibits errors in both response regions. The estimated force curve in Fig. 4.21 shows these errors. Note that in the performance evaluation for the displacement estimation in Sec. 4.5.3, the sponge cut showed the worst estimation performance among the four objects (see Fig. 4.13, and also compare the medians of the ratio of the errors).

Since the stimuli during contact release have less implications on the human hardness perception [70], we focus on the pushing phase. In Fig. 4.21, the curve is overestimated

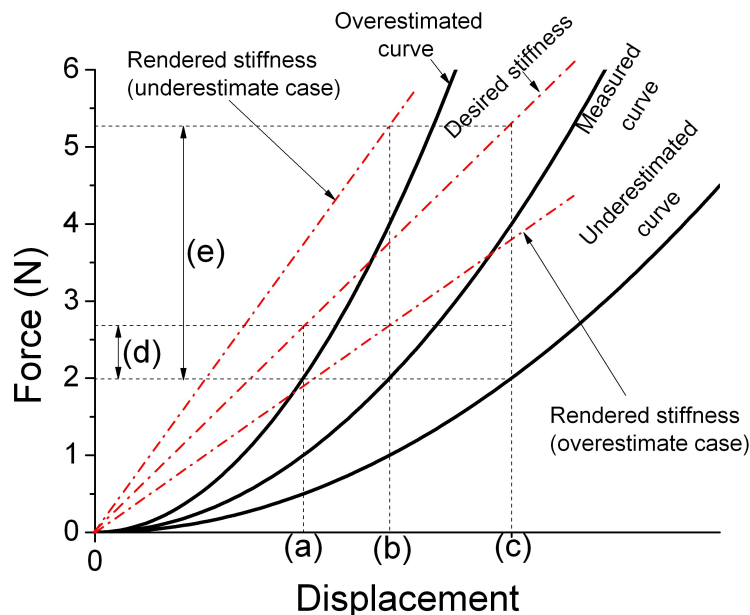


Fig. 4.20 An example showing the effect of underestimated or overestimated dynamics model on the rendered stiffness.

if the displacement is less than 25 mm, and it is underestimated if the displacement is higher than 25 mm. Considering the average peak pressing force to be 14 N (measured in pilot studies), the displacement usually does not exceed 25 mm for the 0.8 N/mm reference stiffness ($0.8 \times 25 = 20$), and thus the force is usually overestimated. We speculate that this is the reason of the negative PSE error on the 'Sponge08' condition. For the 0.3 N/mm reference stiffness, in contrast, the pressing displacement often exceeds 25 mm ($0.3 \times 25 = 7.5$). Thus, the force is underestimated at the force peak on which human often relies when perceiving stiffness, and the PSE error was positive in 'Sponge03' condition. To confirm this, we derive the actually rendered stiffness at the user's hand using Fig. 4.21. Consider that the reference stiffness is 0.8 N/mm, and the true displacement is 20 mm. Due to the identification error, our algorithm estimates displacement as 18.2 mm. To render 0.8 N/mm stiffness, the system exerts force to makes the user perceiving force 14.56 N ($= 0.8 \times 18.2$). Then, the actual stiffness rendered at the user's hand becomes 0.728 N/mm ($= 14.56/20$),

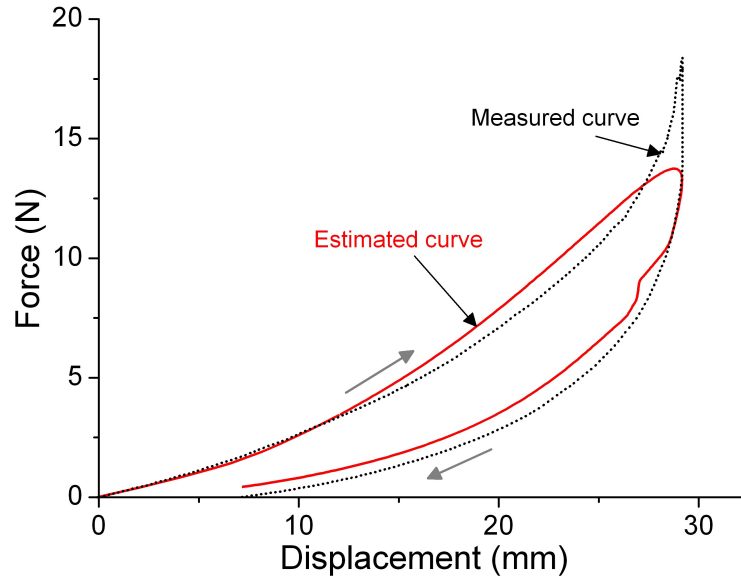


Fig. 4.21 The displacement-force curves for measured values and estimated values.

which is quite comparable to the PSE of ‘Sponge08’ condition.

It is also important that the palpation for the data gathering during the model identification must cover appropriate displacement ranges and velocity ranges that are expected in the interaction of intended usage. The model identified by inappropriately gathered data may exhibit more estimation errors in the displacement estimation. We speculate that the errors even in the foam ball cases were due to this inappropriate data gathering. According to our induction using Fig. 4.20 and the experimental results, the model for foam ball was overestimated for small displacement (see ‘Ball08’), while it was well estimated for the large displacement (see ‘Ball03’). We can expect that during the model identification, the palpation covered large displacement more than small displacement.

4.8 General Discussion

The psychophysical experiment showed that the haptic AR system was quite effective for the stiffness modulation of real objects despite the errors in deformation estimation. In this section, we address several important research issues encountered during the investigation.

First of all, we must admit that the design of our interaction tool may produce undesired torque at the user's hand. We assumed in our algorithms that the points of application of all the forces in the system lie on the same position. In reality, the force application point that the real object applies to (the tool tip) differs from the point that the haptic interface applies to (the point where the three axes of the gimbal encoder meet). This discrepancy makes undesired torque to the tool if the two force vectors do not lie on a same line. With our current tool setup, it was nearly impossible to make the two force application points identical since a force sensor must be installed between the gimbal joint and the tip. Instead, we tried to minimize the distance between the two points as short as possible. Adapting a haptic interface having 6 DOF force feedback capability can be a solution, but complex torque control would be a challenging issue.

Second, the haptic interfaces used in the experiments (PHANToM 1.0 and 1.5 high force), which were originally designed for interaction with virtual objects, are not the best choices for haptic AR that deals with real objects as well. It was observed that the position sensing resolution of the interfaces (= 0.03 mm nominal) is too coarse to adequately quantize the tiny deformation of stiff real objects such as the wood plate, and makes the augmented haptic rendering very unstable. Haptic interfaces with much higher position resolution, e.g., the ministick with 1 μm resolution [99], can be more appropriate to haptic AR. In addition, haptic interfaces with large force outputs are desired in order to handle real objects of high stiffness. The current desktop interfaces, such as the PHANToM 1.5 high force model with the maximum force of 37.5 N, may suffice, but this could not be confirmed due to the position sensing resolution problem. Haptic AR dealing with real objects requires a haptic interface with very fine position sensing resolution, large force output, and, preferably, large workspace. Apparently, developing such a force-feedback haptic interface can be a very challenging task.

Even with the "dream" haptic interface, relying on a displacement-force relationship for stiffness modulation may not be the most effective strategy. In general, the human relies on both kinesthetic and tactile sensory cues for hardness perception [96]. The displacement-force relation described in this paper is the key sensory information for the kinesthetic chan-

nel. The literature also reported several important tactile cues, including vibratory tactile transients that occur at contact and last a short period of time (typically less than 100 ms) [70, 64], static pressure distribution on the contacted skin [96], and contact area spread rate [14]. In the tool-mediated exploration employed in current haptic interfaces, modulating the contact transients can be another promising approach to control the perceived hardness of a real object [68], especially for stiff objects. Algorithms for the approach may require a substantially higher haptic rendering rate than 1 kHz (e.g., 5 kHz was used in [64]), which is another cost-increasing factor. Simpler but effective algorithms such as “stiffness shifting” introduced in [45] can be an alternative.

In addition to the stiffness modulation, a number of research issues need to be considered in order for haptic AR to be widely applied in various fields. First, other salient haptic properties, friction and texture, should also be considered for haptic AR. Modulating friction can be relatively easy if the 3D geometry can be reliably augmented. Changing the perceived quality of textures, however, appears to be a formidable task, due to the difficulty of sensing the micro-scale features of a real object surface as well as the multi-dimensional and non-orthogonal structure of a perceptual space in haptic texture perception [49]. Second, to maximize the usability of haptic AR, haptic augmentation needs to be combined with other sensory modalities, especially with visual feedback. This requires procedures to register visual and haptic coordinate frames and algorithms to match visually and haptically augmented contents. The former topic has been intensively studied in the haptics and AR communities as introduced earlier in Section 2, but the latter topic needs considerable attention. We focus on this issue in Chapter 6. Third, for medical applications, our linear stiffness model for force rendering should be extended so as to describe human soft tissues. This requires more complex model such as a nonlinear visco-elastic model and a general impedance model for force rendering. Our initial trial for the medical application in Chapter 5 clearly shows the advantage of using a nonlinear visco-elastic model for rendering of virtual tumor. Another important issue for medical applications is to provide bare-hand interaction with real objects. The form factor of the sensing and actuation system would be the main hurdle to overcome. Even the simplest step, augmenting a kinesthetic feed-

back only while preserving real tactile feedback, requires a force sensor small enough to be attached at the fingertip while not hindering real tactile feedback. Moreover, the augmentation (or modulation) of the tactile feedback on a bare-hand skin will need completely new sensors and actuators. It will be very hard but ambitious task.

Chapter 5

A Case Study: Haptic Simulation of Breast Cancer Palpation

This chapter presents our effort to demonstrate the potential of haptic AR. We apply the haptic AR system to one of the most prospective application area of AR, medical training with breast cancer screening as a representative example.

For a medical simulator, AR technology has been utilized mainly for visualization; virtual organs constructed from preprocessed radiological data are overlaid on the real operating scene for surgical navigation [67]. On the other hand, supporting for haptic modality in medical simulator is still in an infant stage. One of the common obstacles for the haptic feedback is the lack of easy and practical rendering methods for realistic simulation of human soft tissues [22, 21, 5, 62]. Haptic rendering of a deformable object based on VR, in general, requires a huge amount of precomputation for geometric elements, as well as a high-performance system to fulfill real-time constraints. This led us to simplify the simulation of a real response to some extent. As an alternative, we focus on the unique advantages of AR; ease of constructing a highly realistic and flexible environment without an extensive preprocessing of real environment modeling.

This chapter introduces AR-based simulation methods for the haptic response of a tumor surrounded by soft tissues as a case study for breast cancer palpation training. In the training of breast cancer palpation, haptic realism of the environment, in particular for a re-

alistic tumor inside a breast, is known to be highly correlated to the performance a training [21]. To achieve high-fidelity touch feedback, a real breast model made of soft silicone is augmented with a harder virtual tumor rendered inside. The real silicone model produces natural haptic feedback of the breast tissue deformation, while our AR system is responsible for the tumor simulation. For the reproduction of the tumor response, we use a contact dynamics model identified using position and force data measured from a real breast model containing an actual tumor lump. In particular, our framework requires no preprocessing for the geometric model of the breast, preserving a crucial advantage of AR. A subjective evaluation confirmed that our system can provide realistic behavior close to the real counterparts.

5.1 Interaction Model

The goal of the presented system is to modulate the stiffness of a real breast model as if a stiffer tumor were placed inside. The behavior of the breast model silicone is highly homogeneous, thus facilitating the model-based estimation of the dynamic response of the tumor.

Our system is configured as shown in Fig. 5.1. The response force from the real breast model at time t , $\mathbf{f}_r(t)$, is what the user perceives if no virtual tumor is rendered. The goal is to alter the force delivered to the user's hand, $\mathbf{f}_h(t)$, from $\mathbf{f}_r(t)$ to

$$\mathbf{f}_h(t) = \mathbf{f}_r(t) + \mathbf{f}_t(t), \quad (5.1)$$

where $\mathbf{f}_t(t)$ is the force that the haptic interface produces to represent the virtual tumor. The realism of the tumor simulation relies on the recreation accuracy of $\mathbf{f}_t(t)$ according to the user's interaction.

A key idea of our approach is to derive $\mathbf{f}_t(t)$ based on a nonlinear dynamics model identified using data measured from a breast mock-up containing a real tumor. This allows us to minimize the preprocessing for the breast geometric model and the tumor response while preserving plausible simulation realism. We use the Hunt-Crossley model again, which can account for the nonlinear viscoelastic contact dynamics of a deformable object

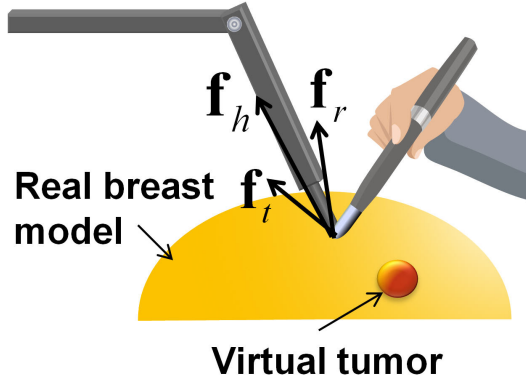


Fig. 5.1 System configuration.

such as human tissues [50, 105], to describe the responses of the tumor and silicone models. It has the form of

$$f(t) = K_e \{x(t)\}^m + B_e \{x(t)\}^m \dot{x}(t), \quad (5.2)$$

where $x(t)$ and $\dot{x}(t)$ are the displacement and velocity of the haptic device tip, respectively, K_e is object stiffness, and m is a constant exponent (usually between 1 and 2).

Variables necessary to derive $\mathbf{f}_t(t)$ are defined in Fig. 5.2. In our current model we assume that the tumor has a spherical shape. \mathbf{p}_t is the position of the tumor sphere, and \mathbf{p}_{ts} is the closest point on the original non-deformed breast surface from \mathbf{p}_t . Both values are known at the start, and our algorithm assumes that they are constant over time. The effect of tumor movements on $\mathbf{f}_t(t)$ is, however, still captured in the response model obtained in the preprocessing step and is thus included in $\mathbf{f}_t(t)$. Let the line segment $\overline{\mathbf{p}_{ts}\mathbf{p}_t}$ be l_0 . We first identify the Hunt-Crossley model that describes the force response of the tumor along l_0 in the preprocessing (see Section 5.2). This is the only information that our algorithm needs in advance. Then, using this identified information we approximate $\mathbf{f}_t(t)$ at positions not on l_0 and render the virtual tumor based on this approximation (see Section 5.3).

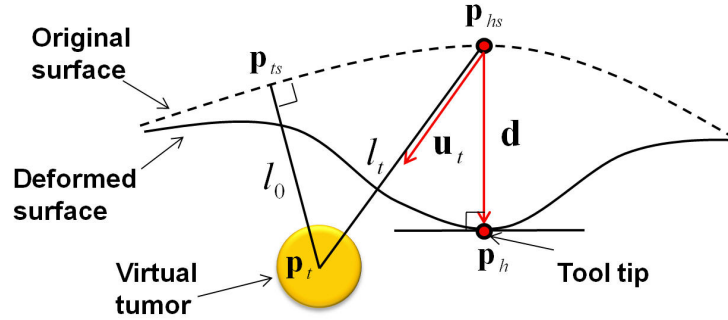


Fig. 5.2 Definition of variables.

5.2 Preprocessing Tumor Response

To identify the Hunt-Crossley model describing the tumor's response along l_0 , we use data collected from two real breast models; one with a real tumor model of higher stiffness included and one without. The two breast models were made by casting a mixture of Ecoflex 0030 (SmoothOn Inc.) and silicone thinner into a breast-shaped mold (half sphere of 55 mm radius). The no-tumor model had uniform elasticity, and its linear stiffness measured at 10 mm displacement was 0.13 N/mm. The tumor-embedded model had the same stiffness except for a 12.5 mm-radius, harder tumor (stiffness of 0.54 N/mm) at 25 mm below the surface.

The hardware configuration is shown in Fig. 5.3. We use a PHANToM 1.5 high force model for the haptic interface, which is capable of 3DOF force feedback and 6DOF pose sensing. A 6D NANO17 force sensor is attached at the end of the interaction tool to measure the reaction force from a real object.

Using this setup, we palpated the two models and collected a set of data triples (reaction force, deformation displacement, and velocity) for each model. We denote the data triple for the no-tumor model as (x_1, \dot{x}_1, f_1) and that for the tumor-embedded model as (x_2, \dot{x}_2, f_2) . When palpating the tumor-embedded model, special care was taken to press along l_0 by carefully selecting the contact point and the pressing direction. Then, we estimated the Hunt-Crossley model parameters for the no-tumor model using (x_1, \dot{x}_1, f_1) ,

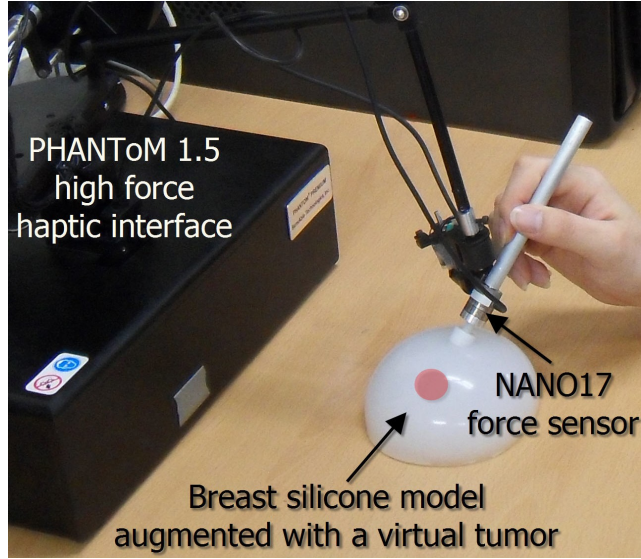


Fig. 5.3 Hardware configuration.

which is denoted by $H_1(x, \dot{x})$. This represents the magnitude of $\mathbf{f}_r(t)$ in (5.1). Since f_2 values measured from the tumor-embedded model include both $\mathbf{f}_r(t)$ and $\mathbf{f}_t(t)$, the magnitude of $\mathbf{f}_t(t)$ can be extracted by subtracting f_1 from f_2 . To this end, we passed all data pairs of (x_2, \dot{x}_2) to $H_1(x, \dot{x})$ and computed the differences by

$$f_t(x_2, \dot{x}_2) = f_2 - H_1(x_2, \dot{x}_2). \quad (5.3)$$

By identifying the Hunt-Crossley model again using the data of (x_2, \dot{x}_2, f_t) , the response of only the tumor along l_0 was derived. This model is denoted by $H_t(x, \dot{x})$. The parameters of the Hunt-Crossley model were identified using the recursive least-square estimation proposed in [44].

5.3 Rendering

The palpation begins with touching the breast model using the haptic tool. The time instance when the tool collides with the breast surface is detected by our algorithm in Chapter 4. After the contact, the haptic interface exerts forces for virtual tumor rendering.

Suppose that a user makes a deformation of $\mathbf{d}(t)$ at time t in Fig. 5.2. $\mathbf{d}(t)$ is directed from $\mathbf{p}_{hs}(t)$ to $\mathbf{p}_h(t)$, where $\mathbf{p}_h(t)$ is the haptic tool position, and $\mathbf{p}_{hs}(t)$ is the closest point from $\mathbf{p}_h(t)$ on the non-deformed breast surface. To determine $\mathbf{p}_{hs}(t)$, we use an estimation method described in Chapter 4, instead of a geometric model of the breast.

Then, the tumor response force $\mathbf{f}_t(t)$ is determined by

$$\mathbf{f}_t(t) = f_t(t) \frac{\mathbf{p}_h(t) - \mathbf{p}_t}{|\mathbf{p}_h(t) - \mathbf{p}_t|}. \quad (5.4)$$

$\mathbf{f}_t(t)$ is directed from \mathbf{p}_t (tumor position) to $\mathbf{p}_h(t)$ (tool tip position) with magnitude $f_t(t)$.

To estimate $f_t(t)$, we use the following algorithm. Let $l_t(t)$ be a line segment $\overline{\mathbf{p}_{hs}(t)\mathbf{p}_t}$. Then, we can project the tool position $\mathbf{p}_h(t)$ to $l_t(t)$ as

$$x_{l_t}(t) = \mathbf{d}(t) \cdot \mathbf{u}_t(t), \quad (5.5)$$

where $\mathbf{u}_t(t)$ is a unit vector from $\mathbf{p}_{hs}(t)$ to \mathbf{p}_t . $x_{l_t}(t)$ represents the deformation caused by the virtual tumor reflected in $\mathbf{d}(t)$.

From $x_{l_t}(t)$, we determine $f_t(t)$ using the Hunt-Crossley model of the tumor obtained by the preprocessing, $H_t(x, \dot{x})$. $H_t(x, \dot{x})$ represents the exact response dynamics of the tumor when a user presses along l_0 . Under the homogeneity assumption, the tumor response along $l_t(t)$ can be described by $H_t(x, \dot{x})$ if the length of l_0 is identical to the length of $l_t(t)$. But in general, $|l_0| \leq |l_t(t)|$, thus we use the following approximation:

$$x(t) = x_{l_t}(t) \frac{|l_0|}{|l_t(t)|}, \quad (5.6)$$

where $x(t)$ is a linearly-normalized deformation magnitude in relation to the reference deformation along l_0 . Then, the force magnitude due to the virtual tumor is estimated as

$$f_t(t) = H_t(x(t), \dot{x}(t)). \quad (5.7)$$

This algorithm is a plausible approximation to the real physical responses, designed for real-time rendering while avoiding the need of geometric models of real objects. We confirmed in a subjective evaluation reported in Section 5.5 that virtual tumors rendered using this algorithm are perceptually similar to real cases. We note that the algorithm may not be applicable to the cases where body parts surrounding a tumor are highly inhomogeneous.

5.4 Physical Performance Evaluation

In this section, the physical performance of our approach is evaluated. We measured the forces at the user's hand when palpating an augmented breast using our algorithm, and compared them with the force data measured using tumor-embedded breast model.

We used two tumor-embedded breast models and one no-tumor model. The surroundings of the three models were identical in shape and stiffness (= 0.13 N/mm at 10 mm displacement). The first tumor-embedded model had a harder real tumor model inside, and its stiffness measured at 10 mm displacement was 0.54 N/mm. The second tumor-embedded model had a little bit softer tumor model inside (= 0.21 N/mm) but it is still harder than the surrounding breast silicone. The radius of the two tumors was 12.5 mm. We identified the responses of the two tumors using the procedure depicted in 5.2, and used them for rendering the virtual tumor in the no-tumor breast model.

Three locations on the breast model were chosen for measuring data to be compared. They were the closest point from the tumor (\mathbf{p}_{ts} in Fig. 5.2), 10 mm left from \mathbf{p}_{ts} , and 20 mm left from \mathbf{p}_{ts} . The three locations on the two tumor-embedded models were manually pressed on without any virtual force, and the displacement-force data was measured. Only vertical movements were allowed and the lateral movements were constrained via active position control using the haptic interface. The same locations on the no-tumor model were pressed on with the virtual force of the identified tumor. Note that the force at the user's hand for the augmented breast was the sum of reaction force from the force sensor and the force exerted by the haptic interface. The maximum pressing force (= 8 N) and the pressing velocity (0 – 100 mm/sec) were tried to be controlled via manual adjustment of palpation using the pressing force and velocity information displayed on the monitor.

Fig. 5.4 shows the displacement-force curves along the vertical direction (y-axis direction) for each location and tumor. The curves for the augmented breast are coincided with that for the tumor-embedded breast quite well. Especially, rendering errors when palpating \mathbf{p}_{ts} (left column in the figure) are quite small, which confirms that the Hunt-Crossley model and our identification method properly capture the response of tumor. On the other hand,

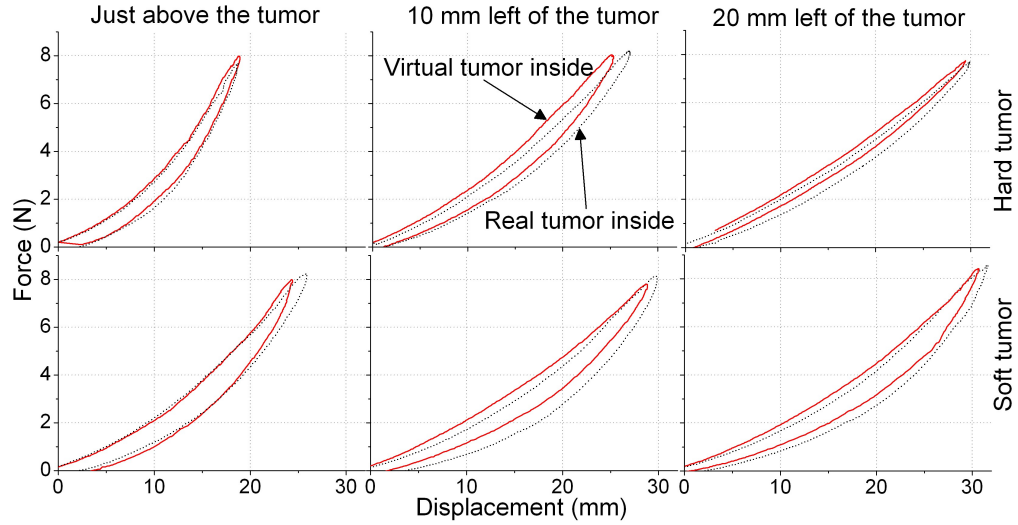


Fig. 5.4 Displacement-force curves at the user's hand. Curves were measured by vertically pressing the hard-tumor-embedded breast model (upper row) and the soft-tumor-embedded breast model (lower row). The pressing locations also varied by the closest surface point from the tumor (left column), 10 mm left from the tumor (middle column), and 20 mm left from the tumor (right column). In each graph, red solid-curve represents data measured from the breast model augmented with a virtual tumor, and the black dotted-curves from the breast with real tumor model.

errors become larger when palpating a little bit away from the tumor (middle column in the figure) but become smaller again when palpating further away from the tumor (left column in the figure). This tendency is due to the approximation on the tumor response applied in our rendering algorithm. As the palpation point moves away from \mathbf{p}_{ts} , the effect of the approximation (and the error due to it), becomes larger (e.g., curves in the middle column). But the point moves further away, eventually, the force from the tumor becomes very weak, and the surrounding silicone dominates the response (e.g., curves in the right column). To reveal the effect of the error on perception, we evaluated the realism of our algorithm in the next section.

5.5 Assessing Realism

Haptic realism of our breast cancer palpation system is assessed via a perception experiment. In the experiment, we measured the perceptual similarity between a breast model with a real tumor model inside and a breast model augmented with a virtual tumor.

5.5.1 Methods

Apparatus In the experiment, we used the same hardware depicted in Fig. 5.3 for augmenting the real silicone breast model.

Subjects Twelve subjects (22–31 years old with average of 25.5) participated in the experiment and were compensated for their help. Two of them were females, and all of them were not experienced users of a force feedback device.

Stimuli There were four tumor presenting methods in the experiment. In all of them, the breast model with the same shape (half sphere of 55 mm radius) and same stiffness (= 0.13 N/mm at 10 mm displacement) surrounded a real or a virtual tumor. The first method presented a harder real tumor model inside the breast model (denoted by Rh). The tumor's stiffness measured at 10 mm displacement was 0.54 N/mm. The second method also had a real tumor model inside the breast silicone, but its stiffness was softer (= 0.21 N/mm) than Rh case (denoted by Rs). In the third method, a virtual tumor rendered by our algorithm was presented with the surrounding breast silicone. Its response was identified using Rh (denoted by Vh). The last one presented a virtual tumor identified using Rs (denoted by Vs).

In each session, the subject was presented with the two breast models in a pair. Both of the models have a tumor inside, but the presenting methods of each tumor were changed according to the experimental condition. The position of the tumor is randomly changed around the center of the breast model. In order for the subjects to use only the haptic cue, visual or auditory cues were tried to be precluded. A white paper box, shown semi-transparently in Fig. 5.5, enclosed the PHANToM and a real object, eliminating any visual

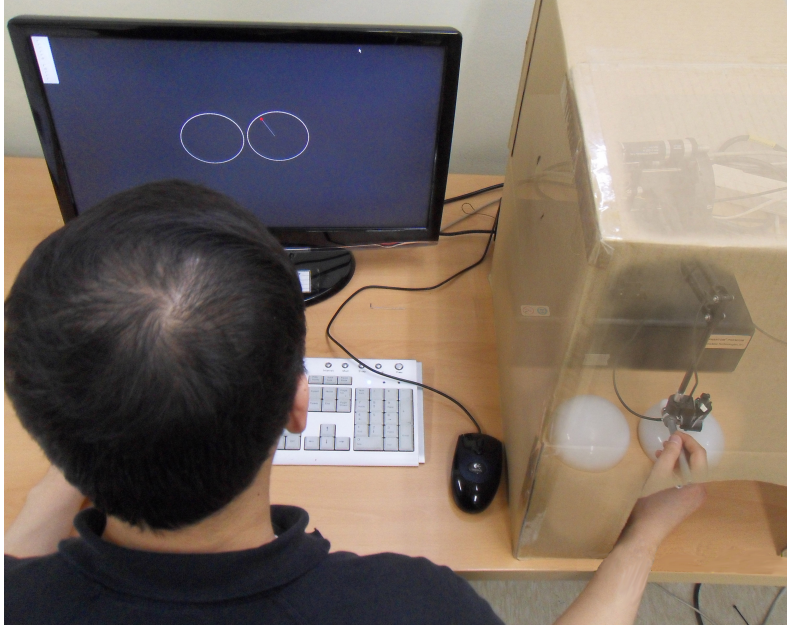


Fig. 5.5 Experimental environment. The blurred paper box is for illustration, and the subject could not see the scene inside during the experiment. To guide the subject's interaction, the haptic interface point and the 2D circles locating the two breast models were shown in the monitor.

cues. Since the location of the two breast models is also invisible during the palpation, two 2D circles representing the two breast models and a point representing the tool tip were visually rendered on the monitor to guide the subject's interaction as depicted in Fig. 5.5. Auditory cues were also precluded by an earplug worn by the subjects.

Experimental Conditions The experiment had four conditions in terms of the combination of the four tumor presenting methods. The first condition presented Rh and Rh in a pair (RhRh). This condition played a role of an upper baseline of the similarity point. The second condition was the Rh and Rs pair (RhRs), which is for the reference of the lower similarity point. The third condition presented Rh and Vh in a pair (RhVh), and the last one for Rs and Vs (RsVs). The last two conditions were the main conditions that the performance of the tumor rendering can be assessed.

With the four conditions, the experiment used a within-subject design. To avoid any order effects, the order of experimental conditions was balanced across the subjects using the Latin Square method [103].

Procedures Prior to the experiment, each subject went through a training session to become familiar with the tumor finding task. In particular, the subject experienced the two reference conditions (RhRh and RhRs) in the training session in order to decide his/her perceptual basis and scale for the similarity score. One experimental condition lasted for 5–7 minutes and the whole experiment took 40 minutes.

Four main sessions for the four experimental conditions followed the training session. For each condition, the subject was asked to repeatedly palpate the two breast models using the haptic tool and to locate the position of the tumors in each model. To ensure that the subject did find the tumor and to measure the time taken to find, the subject was asked to place the tool tip on the tumor position and press a space bar as soon as possible if he/she found a tumor in one stimulus. The subject pressed a space bar again when the tumor in the other stimulus was found. Also, the subject asked to rate, on a scale from 0 to 100, the haptic similarity of the two stimuli, especially for the haptic attributes of the tumors, e.g., size, stiffness, and shape. Point 0 represented that the two stimuli were completely different, and point 100 that the two were exactly the same. The subject was allowed to spend additional time after finding the two tumors if he/she needed time for speculating the similarity score. After each main session, the subject was asked to fill the questionnaire with the similarity score and the comment regarding the reason of the score.

Data Analysis The similarity scores written on the questionnaire were used for the statistical analysis.

To find the time taken to find the tumor, we summed up the time for the tool tip in contact with the breast model until the subject pressed a space bar. Each condition gives two time measurements for the two stimuli, and one subject gives four measurements for Rh, two for Rs, and one for Vh and Vs, respectively (see experimental condition). The

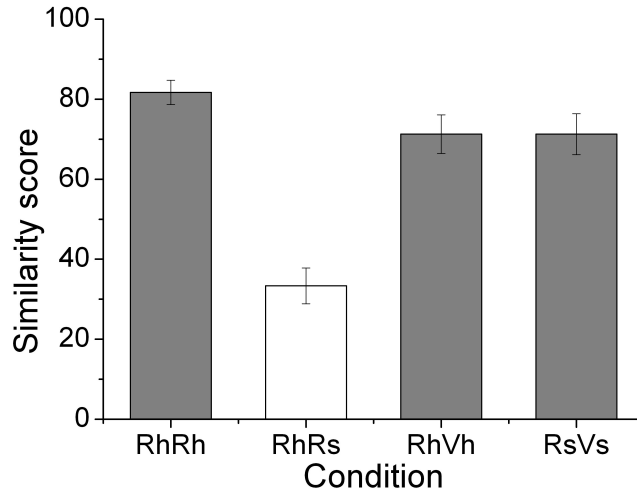


Fig. 5.6 Similarity scores averaged across the subjects. The error bars represent the standard errors. The shades of the bars indicate the result of the Student-Newman-Keuls grouping test. Bars with the same shade were grouped together.

measurements for Rh and Rs were averaged separately, and the time measurements for each tumor presenting method can be derived for each subject.

5.5.2 Results

The means of the original similarity scores over each condition is shown in Fig. 5.6. The scores for RhVh and RsVs conditions are 71.25 for both cases, which are quite close to to the score of RhRh condition (= 81.66). To see the statistical meaning of the results, the one-way within-subject ANOVA test was conducted. The results revealed statistically significant differences among the four conditions ($F_{3,33} = 49.73$, $p < 0.0001$). For post hoc comparison, the Student-Newman-Keuls grouping test was performed ($\alpha = 0.05$). RhRh, RhVh, and RsVs were grouped together, while RhRs made another group. This confirms that the perceptual feeling of the augmented tumor rendered by our algorithm is not quite different from the real counterparts.

This results are further assisted by the measurements of the time taken to find a tumor for each tumor presenting method. Fig. 5.7 reports the means of the time averaged over each

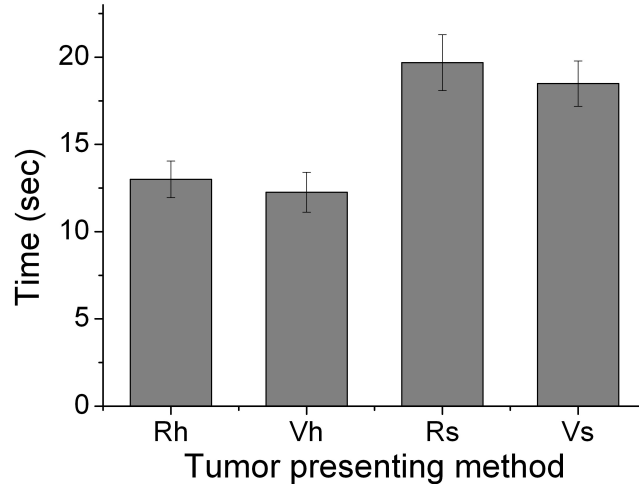


Fig. 5.7 The time taken to find tumor for each tumor presenting method. The error bars represent the standard errors.

tumor presenting method. The averaged time for Vh is very close to that for Rh, and that for Vs is also close to that for Rs. The paired t-test between Vh and Rh revealed that there is no significant difference between them ($p = 0.59$), and the same test between Vs and Rs also reported the same result ($p = 0.35$). These similarities on the tumor locating time represent that the perceptual characteristics of haptic attributes used to find the augmented tumor is quite similar to those used to find the real tumor model.

5.5.3 Discussion

The experimental results confirm that our algorithm successfully recreates the haptic feeling of the tumor, which is very close to the real counterparts. Nevertheless, the scores for the augmented tumor were slightly lower than that for the upper baseline. According to the subject's comments, the most frequent reason for the lower scores of RhVh and RsVs conditions was the dissimilarity of the internal friction between the tumor and the surrounding silicone when rubbing the tumor; the augmented tumor was more slippery than the real one. This was expected since the frictional responses were not dealt in our algorithm. The difficulty of measuring that kind of lateral force and the complex characteristics of the friction

prevents us from introducing appropriate method of dealing with this. Nevertheless, this subjective comment is beneficial to improve our algorithm.

The second frequent reason was the difference of the sizes of the two tumors; augmented tumor was felt smaller. The subject usually perceived the size of the tumor by poking and laterally rubbing the tumor. Here again, the frictional force affected size perception of the tumor. The literature reported that a surface with lower friction is perceived as if it has higher curvature than a true value [26]. In general, a sphere-like object having higher curvature is smaller than that having lower curvature. This fact well agrees with the subject's comment.

To our knowledge, most VR-based tumor palpation simulators lack proper evaluation of the realism of their systems. In most cases, the evaluation focused on the computational efficiency of their soft tissue simulation algorithm [22] and the human performance of detecting and locating the tumor [21, 5, 62]. One work that assessed the realism of the AR-based laparoscopic simulator exists [17], but the system was compared with a virtual counterpart. There is no literature that directly compared the realism of the palpation simulation with real counterparts. In that sense, our assessment of simulator realism compared with a real mock-up amply shows the advantage of AR-based simulator over VR-based one.

5.6 General Discussion

The system achieves excellent realism with minimal complexity of system, which well demonstrates the potential of haptic AR. In particular, no need of real object geometry model is a tangible advantage of our system for practical applications.

Nevertheless, this system is an initial try, and several issues should be investigated prior to the application of the system to real situation. First, the internal friction issue should be investigated for a better realism. Parametric model-based friction identification and rendering can be one solution. Second, a multi-touch interaction should be provided for the better training performance of cancer palpation. More natural way of perceiving the size and shape of the tumor is to seize or grab the tumor with two fingers. The simplest solution will be the connection of two haptic interfaces. For more than two fingers, dedicated ex-

oskeleton haptic interface (e.g., CyberGrasp [98]) or finger tip haptic display (e.g., [73]) can be used. Presumably more important issue is bare-hand interaction. Palpation usually done with a bare hand, and tactile cues such as pressure distribution, degree of sheer in finger tip play great role for the tumor perception [62]. As aforementioned in Section 4.8, bare-hand interaction with augmented object will be very challenging task in terms of hardware and rendering algorithms.

Chapter 6

Visuo-Haptic Augmented Reality

The last chapter is devoted to developing a visuo-haptic AR system covering the whole reality-virtuality continuum of AR for vision and touch. For the efficiency of the development, we adapted a current state-of-the-art visual AR framework instead of developing our own one, and integrated our haptic AR algorithms into the system. We have chosen the visuo-haptic AR system at ETH for the integration, which provides the highly stable and accurate registration [46]. The final result of this chapter enables the augmentation of both the real visual and haptic environment seamlessly with virtual information, while maintaining full functionality. The functionality is demonstrated by applying the system to the example of tumor palpation developed in Chapter 5.

6.1 Visuo-Haptic AR System at ETH

Most previous attempts to construct a visuo-haptic AR system is categorized in 'visual mixed reality-haptic virtuality' (see Chapter 2 for review). Although the early pioneering studies in this category have shown the potential of the visuo-haptic AR system [1, 107, 101, 81], they lack the appropriate concerns on tracking lag reduction, exact alignment of real and virtual coordinate frame both for visual and haptic stimuli, and registration error minimization. Registration errors and latencies in haptic and visual feedback can lead to the loss of spatial and temporal synchronization making the interaction disturbingly unnatural.

Among the recent studies in this category, ETH's visuo-haptic system shows remarkable performance [46]. It has an efficient calibration procedure for visuo-haptic integration, a hybrid tracking technique for stable registration of the augmentation, and a distributed framework ensuring low latency and component synchronization. Their system shows an accuracy of about 1 mm for the haptic feedback, 1-2 pixels for visual feedback for a moving camera, a visual end to end delay of 66 ms, and a temporal accuracy of 1 ms for the synchronized data streams. In particular, they made much effort for the calibration of haptic device integrated in the system, which is the most attracting factor for the integration of our haptic AR algorithms.

The ETH's system is configured as shown in Fig. 6.1. In order to provide enough computational resources, the system is constructed in a distributed framework. The vision part is responsible for the visual augmentation with stereoscopic visual display, real-virtual ob-

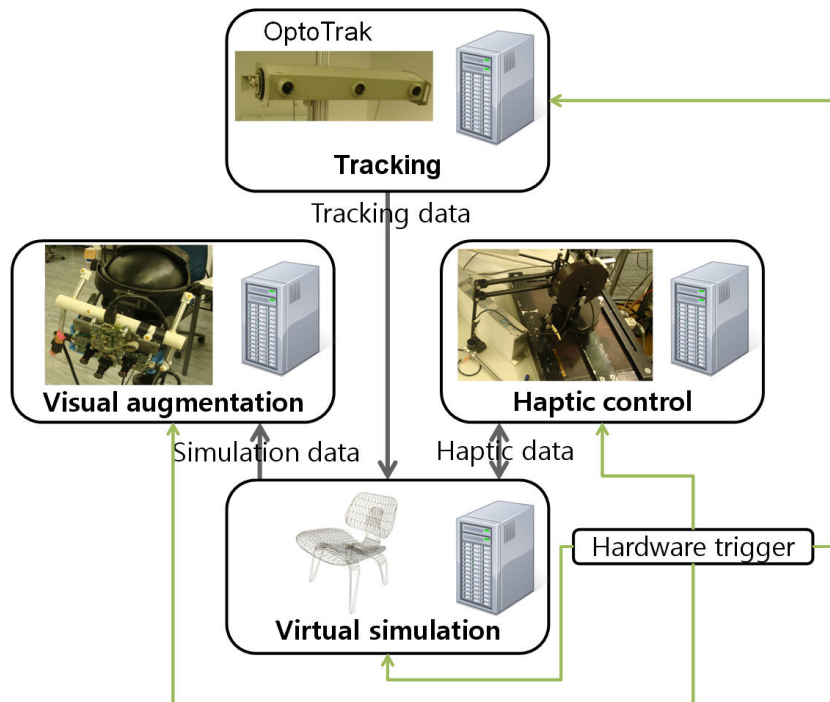


Fig. 6.1 System configuration of ETH's visuo-haptic framework.

ject occlusion, and synthetic shadow (see [63] for more details). The haptic part controls the PHANToM haptic interface to render haptic feedback of virtual objects overlaid on the visual scene. The haptic device is collocated with the visual augmentations by using a two staged calibration procedure and an external optical tracker. Physical simulation of virtual objects is processed in a dedicated simulation machine, and the simulation results are shared with both the haptic and visual part. Data among the system parts is synchronized using a hardware trigger.

6.2 System Integration

The ETH's system only provided virtual haptic feedback for the haptic rendering, which was one of limiting factors of the system for practical application, such as medical training system shown in Chapter 5. Reasonably accurate virtual haptic simulation of deformable soft tissues required a dedicated machine for simulation, which increased the overall complexity of the system as shown in Fig. 6.1. By integrating our haptic AR, we can bypasses this problem by simulating the virtual object only partially, while the real surrounding is incorporated if a virtual representation is not possible or its fidelity is insufficient. This aspect also reduces efforts for precise geometric modeling and visual rendering of the interacting

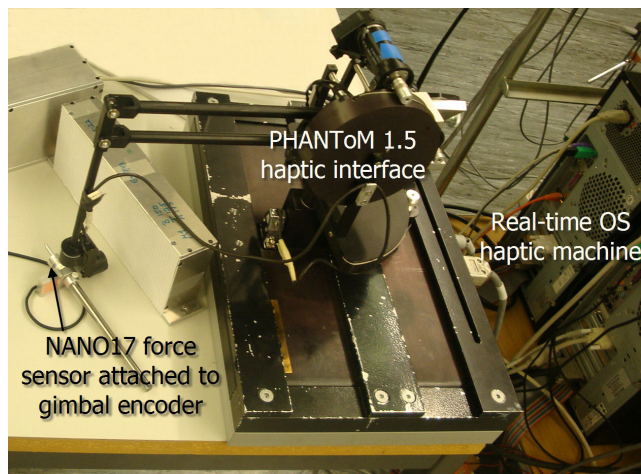


Fig. 6.2 Haptic system for the haptic augmentation.

objects. By employing ‘self-visible’ and ‘self-touchable’ real objects, the system does not have to care about computationally expensive visual rendering such as shading for lighting effects, simulation for deformation rendering.

We supply algorithms for augmenting the haptic response of real objects with virtual force feedback, while ETH provides its collocated visuo-haptic AR environment. Our haptic AR algorithm is directly integrated into the haptic machine in Fig. 6.1. Since their haptic machine is operated by the real-time OS (RTOS), our algorithms are modified to incorporate with it. Also, the original system does not have a force sensor, and the haptic tool is modified to instrument a NANO17 force sensor. The final haptic system is shown in Fig. 6.2.

6.3 Example of Breast Cancer Palpation

We apply the integrated system to breast cancer palpation introduced in Chapter 5 as an example. We visualize the virtual tumor using the vision system to help trainees to understand the tumor movement according to the interaction.

We use the same algorithm described in Chapter 5 to simulate the force feedback of a virtual tumor. Since the tumor position is assumed constant in the algorithm, the tumor movement is simulated, only for visualization, using simple linear spring-damper model. Although this simple simulation does not agree with the real physical responses, we guess it can still demonstrate the potential of the system and give some insight to understand the basic response of the tumor in accordance with trainee’s interaction.

Our algorithm simplifies the tumor dynamics such that the tumor is a massless point connected to its initial position (tumor position without any external force) by an extension spring with a damper and connected again to the interaction tool tip by a compression spring with a damper as shown in Fig. 6.3. Our homogeneity assumption enables us to use the same linear stiffness and damping parameters for the two connections. The tumor movement vector, $\mathbf{d}_t(t)$, can be derived as follows. The movement can be decomposed to

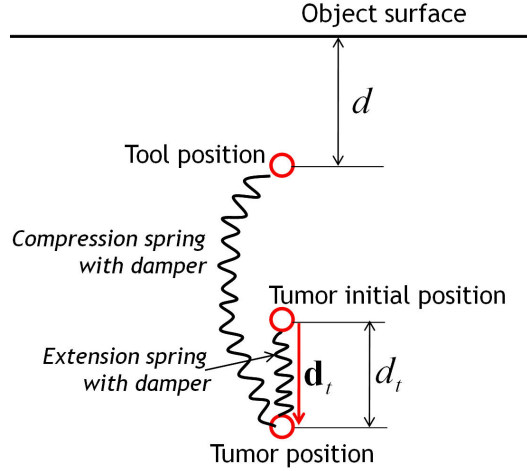


Fig. 6.3 Terms for tumor visualization.

its magnitude and a unit vector directing the movement by

$$\mathbf{d}_t(t) = d_t(t)\mathbf{u}_t(t). \quad (6.1)$$

$\mathbf{u}_t(t)$ can be directed from the tool tip position to the tumor initial position.

The magnitude of the movement, $d_t(t)$, can be derived as follows. Let the displacement of the tool tip be $d(t)$ in the figure, which can be estimated using our algorithm introduced in Chapter 4. Due to the forces from the two spring-damper systems, the forces at the tumor are in an equilibrium state at time t such that:

$$K\{d(t) - d_t(t)\} + B\{\dot{d}(t) - \dot{d}_t(t)\} = Kd_t(t) + B\dot{d}_t(t), \quad (6.2)$$

where K and B are the stiffness and damping parameters of the two springs, respectively. Rearranging the equation to get $d_t(t)$ gives

$$d_t(t) = \frac{d(t)}{2} + \frac{B\dot{d}(t)}{2K} - \frac{B\dot{d}_t(t)}{K}. \quad (6.3)$$

Since $\dot{d}_t(t)$ is unknown at this step, we replace it as $\dot{d}_t(t) = \dot{d}_t(t-1)$, which does not seriously affect the simulation due to short rendering period (1 ms).

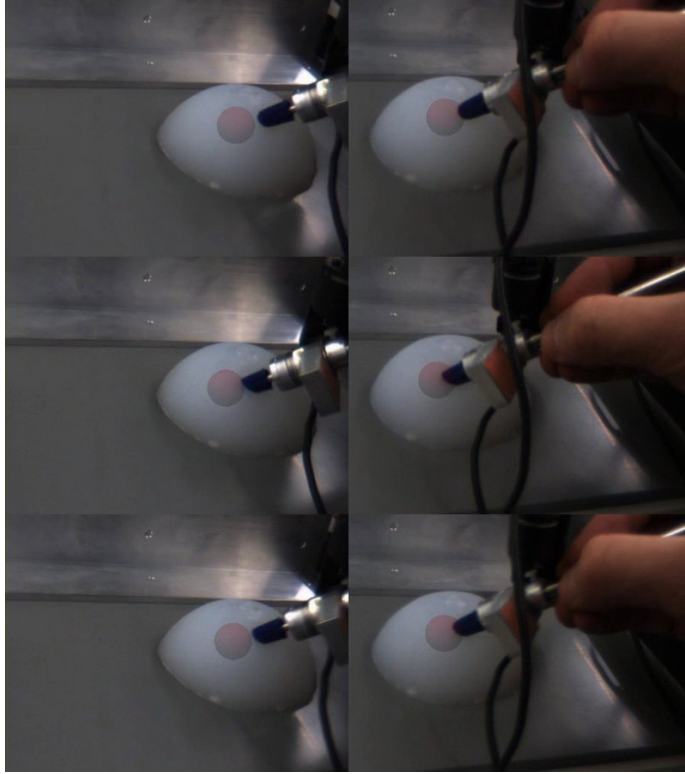


Fig. 6.4 Visualizing tumor movement. The image sequence is directly displayed through the head-mounted display. Two images in a row are for stereoscopic vision.

In rendering, we used 0.45 N/mm for K and 0.004 Ns/mm for B , which were found by empirical tuning to show realistic movement. The example image sequence of this simulation is shown in Fig. 6.4. Note that ETH's previous open surgery training system [46] needed a dedicated machine for haptic and visual simulation of soft tissues (the virtual simulation part in Fig. 6.1). On the other hand, our AR-based algorithm in Chapter 5 is simple enough to be directly embedded into the haptic machine without the need of additional hardware.

6.4 Discussion

In this chapter, our stiffness modulation algorithms are smoothly integrated into a visual AR framework, showing the competence of haptic AR for practical applications. In particular, it is shown that our algorithms are developed so as to be easily incorporated with any other visual-haptic AR framework. This aspect agrees with our goal of this research; building a toolkit for a general haptic AR. The work in this dissertation will be the first building block towards this goal.

Conclusions

Haptic AR is an emerging research area that holds great promise to turn real environments that we live in to augmented environments where “impossible-in-real” things are doable. This dissertation establishes and proves the concept of this exciting technology of haptic AR, opening a new possibility for this field. Beginning with proposing the taxonomy of haptic AR, we construct two haptic AR systems that can change the stiffness of a real object to a desired value. All required modules for the stiffness modulation are developed, while keeping minimal complexity in both hardware and software. The performance of each module was empirically evaluated, followed by a psychophysical experiment that proved the competency of our system in terms of the human perception. In addition, several research issues critical for further improvements are discussed. The rest of the dissertation is devoted to prove the potential of the haptic AR by a case study of breast cancer palpation. Realistic rendering of a virtual tumor surrounded by real breast phantom confirms the applicability of the haptic AR technology. The whole haptic AR system is integrated into a state-of-the-art visuo-haptic framework, completing the whole reality-virtuality continuum for both vision and touch.

The author’s effort in dissertation is the first step along the long way towards our broad goal; building a toolkit for a general haptic AR. The author will continue to explore the remaining issues towards this goal. Modulating contact transient vibration will be the last

target for the hardness modulation of a real object. Next step will be the modulation of the friction, which will raise new challenging research issues. Another important issue for the practical application is to provide multi-touch and bare-hand interaction. It is our hope that this dissertation would prompt more interest in the promising field of haptic AR from the research community, and our effort would be applied to various practical fields such as rehabilitation, surgical training, sensorimotor skill transfer, and entertainment.

요약문

햅틱 증강현실: 실제 물체의 강도 변경

햅틱증강현실이란 가상과 실제의 촉각정보를 혼합하여 사용자에게 제공함으로써 증강된 실제 환경을 만들어 내는 기술이다. 예를 들어, 햅틱증강현실은 의학도들의 암 진단 훈련을 위해 실제 마네킹 내부에 가상의 종기를 만들어 낼 수 있고, 학생들이 시간적 공간적 제약 없이 이를 촉진하면서 훈련을 수행할 수 있게 한다. 그러나 햅틱 증강현실의 큰 가능성에도 불구하고 지금까지 이러한 기능을 수행하기 위한 일반적이고 체계적인 방법론은 거의 제시되지 않았다. 본 연구는 햅틱증강현실을 위한 일반적이고 체계적인 방법론, 즉 “햅틱 AR Toolkit”, 을 개발하는 것을 최종 목표로 삼는다. 본 연구에서는 우선 아직 개념조차 정립되지 않은 햅틱증강현실 연구 분야를 명확히 하고 햅틱증강현실 시스템의 분류를 위한 분류법을 제안하였다. Milgram이 제안한 시각을 위한 실제-가상 수직선 (Reality-Virtuality Continuum)을 촉각으로 확장하여 시-촉각 수직선을 만들고, 이를 이용해 기존의 햅틱증강현실 관련 문헌 및 시스템을 분류, 분석하고 관련 연구 이슈들을 도출하였다. 분석 결과, 햅틱증강현실을 현실화하기 가장 필요한 기능은 가상의 햅틱 피드백을 이용해 실제 물체의 햅틱 속성(강도, 마찰력 등)을 변경해 주는 기능이라는 것을 알 수 있었다. 이 개념의 실현가능성을 보기 위해 우선 본 연구에서는 가장 중요한 촉감속성중의 하나인 강도 (Stiffness)를 선택하고 실제물체의 강도를 변경시키는 방법을 개발하였다. 이를 위해 상용 햅틱 장치에 힘 측정 장치를 달고, 실제물체와 햅틱장치 끝단과의 충돌검사, 실제물체의 기하학적인 정보 없이 물체 변형정도 추정, 원하는 강도를 렌더링 하기 위

해 햅틱장치가 내야 하는 힘 계산 및 햅틱장치의 제어 등을 위한 알고리즘들을 개발하였다. 각각은 난이도에 따라 단계적으로 개발되었는데, 우선 간단한 1차원 두드리기 동작을 위한 알고리즘을 개발하고 이를 굽기, 윤곽 따라가기 등의 3차원 동작을 지원하는 시스템으로 확장하였다. 특히, 모든 알고리즘들은 증강현실 시스템의 적용 가능성을 높이기 위해 실제 환경 모델링을 위한 전처리 과정을 최소화 하는 방향으로 설계되었다. 다양한 실제 물체에 대해서 각각의 알고리즘들의 물리적인 성능 평가가 수행되었고, 전체 시스템의 인지적인 평가를 위해 사용자를 대상으로 한 정신물리학 실험이 수행되었다. 성능평가 결과 본 시스템은 인지적으로 충분히 만족할만한 성능이라는 것이 검증되었다. 다음으로, 햅틱증강현실의 적용 가능성을 알아보기 위해 전술한 의학도를 위한 유방암 검사 훈련에 강도변경 시스템을 적용하였다. 실제 실리콘으로 만들어진 유방 모형 안에 실제 종기모형의 촉감 데이터를 기반으로 렌더링 된 가상의 딱딱한 종기를 제공함으로써 훈련 시스템의 사실성을 높였다. 훈련시스템의 사용성 평가 결과 본 시스템은 실제 연습용 모형을 사용하는 훈련 시스템과 성능 적으로 차이가 없으면서 좀 더 유연한 환경을 사용자에게 제공할 수 있었다. 최종적으로 본 햅틱증강현실 기술은 기존의 시각증강현실 시스템과 통합되어 시-촉각 증강현실 시스템을 구성하고, 이를 위의 가상의 종기모형을 가시화 하는데 응용되었다.

Bibliography

- [1] M. Adcock, M. Hutchins, and C. Gunn. Augmented reality haptics: Using AR-ToolKit for display of haptic applications. In *Proceedings of Augmented Reality Toolkit Workshop*, pages 1–2, 2003.
- [2] F. Al-Bender, V. Lampaert, and J. Swevers. The generalized Maxwell-slip model: A novel model for friction simulation and compensation. *IEEE Transactions on Automatic Control*, 50(11):1883–1887, 2005.
- [3] B. Armstrong-Hélouvry, P. Dupont, and C. C. de Wit. A survey of models, analysis tools and compensation methods for the control of machines with friction. *Automatica*, 30(7):1083–1138, 1994.
- [4] R. Azuma, Y. Baillot, R. Behringer, S. Feiner, S. Julier, and B. MacIntyre. Recent advances in augmented reality. *IEEE Computer Graphics & Applications*, 21(6):34–47, 2001.
- [5] S. Baillie, A. Crossan, S. Brewster, D. Mellor, and S. Reid. Validation of a bovine rectal palpation. In *Studies in Health Technology & Informatics*, pages 33–36, 2005.

-
- [6] F. Barbagli, K. Salisbury, C. Ho, C. Spence, and H. Z. Tan. Haptic discrimination of force direction and the influence of visual information. *ACM Transactions on Applied Perception*, 3(2):125–135, 2006.
- [7] B. Bayart, J. Y. Didier, and A. Kheddar. Force feedback virtual painting on real objects: A paradigm of augmented reality haptics. *Lecture Notes in Computer Science (EuroHaptics 2008)*, 5024:776–785, 2008.
- [8] B. Bayart, A. Drif, A. Kheddar, and J. Y. Didier. Visuo-haptic blending applied to a tele-touch-diagnosis application. *Lecture Notes in Computer Science (Eurohaptics 2007)*, 4563:617–626, 2007.
- [9] B. Bayart and A. Kheddar. Haptic augmented reality taxonomy: Haptic enhancing and enhanced haptics. In *Proceedings of EuroHaptics*, pages 641–644, 2006.
- [10] E. Bennett and B. Stevens. The effect that the visual and haptic problems associated with touching a projection augmented model have on object-presence. *Presence: Teleoperators and Virtual Environments*, 15(4):419–437, 2006.
- [11] L. Biagiotti and C. Melchiorri. Environment estimation in teleoperation systems. In M. Ferre, M. Buss, R. Aracil, C. Melchiorri, and C. Balaguer, editors, *Advances in Telerobotics*. Springer-Verlag, 2006.
- [12] G. Bianchi, C. Jung, B. Knoerlein, G. Székely, and M. Harders. High-fidelity visuo-haptic interaction with virtual objects in multi-modal AR systems. In *Proceedings of the IEEE and ACM International Symposium on Mixed and Augmented Reality*, pages 187–196, 2006.
- [13] G. Bianchi, B. Knoerlein, G. Székely, and M. Harders. High precision augmented reality haptics. In *Proceedings of EuroHaptics*, pages 169–168, 2006.

-
- [14] A. Bicchi, E. P. Scilingo, and D. D. Rossi. Haptic discrimination of softness in teleoperation: The role of the contact area spread rate. *IEEE Transactions on Robotics and Automation*, 16(5):496–504, 2000.
- [15] M. Billinghurst, H. Kato, and I. Poupyrev. The MagicBook – Moving seamlessly between reality and virtuality. *IEEE Computer Graphics & Applications*, 21(3):6–8, 2001.
- [16] C. W. Borst and R. A. Volz. Evaluation of a haptic mixed reality system for interactions with a virtual control panel. *Presence: Teleoperators and Virtual Environments*, 14(6):677–696, 2005.
- [17] S. M. B. I. Botden, S. N. Buzink, M. P. Schijven, and J. J. Jakimowicz. Augmented versus virtual reality laparoscopic simulation: What is the difference? *World Journal of Surgery*, 31:764–772, 2007.
- [18] S. M. B. I. Botden, S. N. Buzink, M. P. Schijven, and J. J. Jakimowicz. ProMIS augmented reality training of laparoscopic procedures face validity. *Simulation in Healthcare: The Journal of the Society for Simulation in Healthcare*, 3(2):97–102, 2008.
- [19] S. M. B. I. Botden and J. J. Jakimowicz. What is going on in augmented reality simulation in laparoscopic surgery? *Surgical Endoscopy*, 23(8):1693–1700, 2008.
- [20] L. N. Brown and R. S. Sainsbury. Hemispheric equivalence and age-related differences in judgments of simultaneity to somatosensory stimuli. *Journal of Clinical and Experimental Neuropsychology*, 22(5):587–598, 2000.

- [21] G. Burdea, G. Patounakis, V. Popescu, and R. E. Weiss. Virtual reality-based training for the diagnosis of prostate cancer. *IEEE Transactions on Biomedical Engineering*, 46(10):1253–1260, 1999.
- [22] H. Chen, W. Wu, H. Sun, and P.-A. Heng. Dynamic touch-enabled virtual palpation. *Computer Animation and Virtual Worlds*, 18:339–348, 2007.
- [23] J. Cheon, I. Hwang, K. Han, and S. Choi. Haptizing a surface height change with varying stiffness based on force constancy: Extended algorithm. In *Proceedings of the Symposium on Haptic Interfaces for Virtual Environment and Teleoperator Systems*, pages 193–200, 2008.
- [24] S. Choi and H. Z. Tan. Perceived instability of virtual haptic texture. I. Experimental studies. *Presence: Teleoperators and Virtual Environment*, 13(4):395–415, 2004.
- [25] S. Choi and H. Z. Tan. Perceived instability of virtual haptic texture. II. Effects of collision detection algorithm. *Presence: Teleoperators and Virtual Environments*, 14(4):463–481, 2005.
- [26] C. G. Christou and A. M. Wing. Friction and curvature judgement. In *Proceedings of EuroHaptics*, pages 36–40, 2001.
- [27] J. E. Colgate and G. G. Schenkel. Passivity of a class of sampled-data systems: Application to haptic interfaces. *Journal of Robotic Systems*, 14(1):37–47, 1997.
- [28] E. Costanza, A. Kunz, and M. Fjeld. Mixed reality: A survey. In *Human Machine Interaction: Research Results of the MMI Program*, pages 47–68. Springer Verlag: Berlin, 2009.

- [29] P. R. Dahl. A solid friction model. Technical report, Aerospace corp el segundo CA, 1968.
- [30] C. C. de Wit, H. Olsson, K. Astrom, and P. Lischinsky. A new model for control of systems with friction. *IEEE Transactions on Automatic Control*, 40(3):419–425, 1995.
- [31] N. Diolaiti, C. Melchiorri, and S. Stramigioli. Contact impedance estimation for robotic systems. *IEEE Transactions on Robotics*, 21(5):925–935, 2005.
- [32] P. Dupont, V. Hayward, B. Armstrong, and F. Altpeter. Single state elastoplastic friction models. *IEEE Transactions on Automatic Control*, 47:787–792, 2002.
- [33] D. Erickson, M. Weber, and I. Sharf. Contact stiffness and damping estimation for robotic systems. *The International Journal of Robotics Research*, 22(1):41–57, 2003.
- [34] W. N. Findley, J. S. Lai, and K. Onaran. *Creep and Relaxation of Nonlinear Viscoelastic Materials*. Dover Publications, 1989.
- [35] W. Fluegge. *Viscoelasticity*. Blaisdell Pub. Co, 1967.
- [36] A. Freudenthal, E. Samset, B. Geršak, J. Declerck, D. Schmalstieg, S. Casciaro, O. Rideng, and J. V. Sloten. Augmented reality in surgery ARIS*ER, research training network for minimally invasive therapy technologies. *Endoscopic Review*, 10(23):5–10, 2005.
- [37] R. M. Friedman, K. D. Hester, B. G. Green, and R. H. LaMotte. Magnitude estimation of softness. *Experimental Brain Research*, 191(2):133–142, 2008.
- [38] G. Geffen, V. Rosa, and M. Luciano. Sex differences in the perception of tactile simultaneity. *Cortex*, 36:323–335, 2000.

- [39] G. D. Gersem. *Kinaesthetic feedback and enhanced sensitivity in robotic endoscopic telesurgery*. PhD thesis, Katholieke Universiteit Leuven, 2005.
- [40] G. A. Gescheider. *Psychophysics: The Fundamentals*. Lawrence Erlbaum, 3rd edition, 1997.
- [41] G. Gilardi and I. Sharf. Literature survey of contact dynamics modeling. *Mechanism and Machine Theory*, 37(10):1213–1239, 2002.
- [42] N. Gurari, K. J. Kuchenbecker, and A. M. Okamura. Stiffness discrimination with visual and proprioceptive cues. In *Proceedings of the World Haptics Conference*, pages 121–126, 2009.
- [43] T. Ha, Y. Chang, and W. Woo. Usability test of immersion for augmented reality based product design. *Lecture Notes in Computer Science (Edutainment 2007)*, 4469:152–161, 2007.
- [44] A. Haddadi and K. Hashtardi-Zaad. A new method for online parameter estimation of Hunt-Crossley environment dynamic models. In *IEEE/RSJ International Conference on Intelligent Robots and Systems*, pages 981–986, 2008.
- [45] G. Han, S. Jeon, and S. Choi. Improving perceived hardness of haptic rendering via Stiffness Shifting: An initial study. In *Proceedings of the ACM Symposium on Virtual Reality Software and Technology*, pages 87–90, 2009.
- [46] M. Harders, G. Bianchi, B. Knoerlein, and G. Székely. Calibration, registration, and synchronization for high precision augmented reality haptics. *IEEE Transactions on Visualization and Computer Graphics*, 15(1):138–149, 2009.
- [47] M. H. Hayes. *Statistical Digital Signal Processing and Modeling*. Wiley, 1996.

- [48] R. Hoever, G. Kosa, G. Székely, and M. Harders. Data-driven haptic rendering – From viscous fluids to visco-elastic solids. *IEEE Transactions on Haptics*, 2:15–27, 2009.
- [49] M. Hollins, R. Faldowski, S. Rao, and F. Young. Perceptual dimensions of tactile surface texture: A multidimensional scaling analysis. *Perception & Psychophysics*, 54(6):697–705, 1993.
- [50] K. Hunt and F. Crossley. Coefficient of restitution interpreted as damping in vibroimpact. *ASME Journal of Applied Mechanics*, 42:440–445, 1975.
- [51] K. Hunt, M. Muni, N. Donaldson, and F. Barr. Investigation of Hammerstein hypothesis in the modeling of electrically stimulated muscle. *IEEE Transactions on Biomedical Engineering*, 45(8):998–1009, 1998.
- [52] D. L. James and D. K. Pai. A unified treatment of elastostatic contact simulation for real time haptics. *Haptics-E: Electronic Journal of Haptics Research*, 2(1), 2001.
- [53] F. Janabi-Sharifi, V. Hayward, and C. S. J. Chen. Discrete-time adaptive windowing for velocity estimation. *IEEE Transactions on Control Systems Technology*, 8(6):1003–1009, 2000.
- [54] S. Jeon. Friction identification and its application to haptic AR. Technical Report JSH-HAR-02, Pohang University of Science and Technology, 11 2009.
- [55] S. Jeon and S. Choi. Haptic augmented reality: Taxonomy and an example of stiffness modulation. *Presence: Teleoperators and Virtual Environments*, 18(5):387–408, 2009.

- [56] A. Johnson, D. Sandin, G. Dawe, T. DeFanti, D. Pape, Z. Qiu, and D. P. S. Thongrong. Developing the PARIS: Using the CAVE to prototype a new VR display. In *Proceedings of the ACM Symposium on Immersive Projection Technology*, 2000.
- [57] L. A. Jones and I. W. Hunter. A perceptual analysis of stiffness. *Experimental Brain Research*, 79(1):150–156, 1990.
- [58] H. Kajimoto, N. Kawakami, S. Tachi, and M. Inami. SmartTouch: Electric skin to touch the untouchable. *IEEE Computer Graphics & Applications*, 24(1):36–43, 2004.
- [59] E. Karadogan, R. L. Williams II, J. N. Howell, and R. R. Conatser Jr. A stiffness discrimination experiment including analysis of palpation forces and velocities. In *Proceedings of the International Meeting on Simulation in Healthcare*, 2009.
- [60] H. Kato and M. Billinghurst. Marker tracking and HMD calibration for a video-based augmented reality conferencing system. In *Proceedings of the IEEE and ACM International Workshop on Augmented Reality*, pages 85–94, 1999.
- [61] S. Kim, J. Cha, J. Kim, J. Ryu, S. Eom, N. P. Mahalik, and B. Ahn. A novel test-bed for immersive and interactive broadcasting production using augmented reality and haptics. *IEICE Transactions on Information and Systems*, E89-D(1):106–110, 2006.
- [62] S.-Y. Kim, K.-U. Kyung, J. Park, and D.-S. Kwon. Real-time area-based haptic rendering and the augmented tactile display device for a palpation simulator. *Advanced Robotics*, 21(9):961–981, 2007.
- [63] B. Knoerlein, G. Székely, and M. Harders. Enhanced visual depth cues for collocated visuo-haptic augmented reality. In *Proceedings of the International Conference in*

- Central Europe on Computer Graphics, Visualization and Computer Vision*, pages 197–204, 2010.
- [64] K. J. Kuchenbecker, J. Fiene, and G. Niemeyer. Improving contact realism through event-based haptic feedback. *IEEE Transactions on Visualization and Computer Graphics*, 12(2):219–230, 2006.
- [65] Y. Kurita, A. Ikeda, T. Tamaki, T. Ogasawara, and K. Nagata. Haptic augmented reality interface using the real force response of an object. In *Proceedings of the ACM Virtual Reality Software and Technology*, pages 83–86, 2009.
- [66] K.-U. Kyung and J.-Y. Lee. Ubi-Pen: A haptic interface with texture and vibrotactile display. *IEEE Computer Graphics and Applications*, 29(1):24–32, 2009.
- [67] P. Lamata, W. Ali, A. Cano, J. Cornella, J. Declerck, O. J. Elle, A. Freudenthal, H. Furtado, D. Kalkofen, E. Narum, E. Samset, P. Sánchez-Gonzalez, F. M. Sánchez-Margallo, D. Schmalstieg, M. Sette, T. Stedeli, J. V. Sloten, and E. J. Gómez. Augmented reality for minimally invasive surgery: Overview and some recent advances. In S. Maad, editor, *Augmented Reality*, pages 73–98. In-Tech, 2010.
- [68] R. H. LaMotte. Softness discrimination with a tool. *The Journal of Neurophysiology*, 83(4):1777–1786, 2000.
- [69] R. Lapeer, M. Chen, and J. Villagrana. An augmented reality based simulation of obstetric forceps delivery. In *Proceedings of the IEEE and ACM International Symposium on Mixed and Augmented Reality*, pages 1–2, 2004.
- [70] D. A. Lawrence, L. Y. Pao, A. M. Dougherty, M. A. Salada, and Y. Pavlou. Rate-hardness: A new performance metric for haptic interfaces. *IEEE Transactions on Robotics and Automation*, 16(4):357–371, 2000.

- [71] S. J. Lederman and R. L. Klatzky. Hand movements: A window into haptic object recognition. *Cognitive Psychology*, 19(3):342–368, 1987.
- [72] C. Lee, B. D. Adelstein, and S. Choi. Haptic weather. In *Proceedings of the Symposium on Haptic Interfaces for Virtual Environments and Teleoperator Systems*, pages 473–474, 2008.
- [73] R. Leuschke, E. K. T. Kurihara, J. Doshier, and B. Hannaford. High fidelity multi finger haptic display. In *Proceedings of the WorldHaptics Conference*, 2005.
- [74] F. L. Lewis, C. T. Abdallah, and D. M. Dawson. *Control of Robot Manipulators*. MacMillan Publishing Company, 866 Third Avenue, New York, NY, 1993.
- [75] L. Ljung. *System Identification: Theory for the User*. Prentice Hall, Upper Saddle River, NJ, USA, second edition, 1999.
- [76] C. Luciano, P. Banerjee, L. Florea, and G. Dawe. Design of the ImmersiveTouch: A high-performance haptic augmented virtual reality system. In *Proceedings of the International Conference on Human-Computer Interaction*, 2005.
- [77] Q. Luo and J. Xiao. Modeling complex contacts involving deformable objects for haptic and graphic rendering. In *Robotics: Science and Systems I*. Cambridge, MA, 2005.
- [78] M. Mahvash and V. Hayward. High fidelity haptic synthesis of contact with deformable bodies. *IEEE Computer Graphics and Applications*, 24(2):48–55, 2004.
- [79] M. Mahvash and A. M. Okamura. Friction compensation for a force-feedback telerobotic system. In *Proceedings of the IEEE International Conference on Robotics and Automation*, pages 3268–3273, 2006.

- [80] D. W. Marhefka and D. E. Orin. A compliant contact model with nonlinear damping for simulations of robotic systems. *IEEE Transactions on Systems, Man, and Cybernetics, Part A*, 29(6):566–572, 1999.
- [81] L. Martorella, G. D. Pietro, G. Docile, and M. Bergainasco. Hand—A haptic system for analysis and driving of hand movements in augmented reality environment. In *Proceedings of the IEEE International Workshop on Robot and Human Interactive Communication*, pages 171–174, 2003.
- [82] P. Milgram and H. Colquhoun Jr. A taxonomy of real and virtual world display integration. In Y. Tamura, editor, *Mixed Reality – Merging Real and Virtual Worlds*, pages 1–16. Springer Verlag: Berlin, 1999.
- [83] T. Nojima, D. Sekiguchi, M. Inami, and S. Tachi. The SmartTool: A system for augmented reality of haptics. In *Proceedings of the IEEE Virtual Reality Conference*, pages 67–72, 2002.
- [84] A. M. Okamura, M. R. Cutkosky, and J. T. Dennerlein. Reality-based models for vibration feedback in virtual environments. *IEEE/ASME Transactions on Mechatronics*, 6(3):245–252, 2001.
- [85] R. Ott, D. Thalmann, and F. Vexo. Haptic feedback in mixed-reality environment. *The Visual Computer: International Journal of Computer Graphics*, 23(9):843–849, 2007.
- [86] D. K. Pai, K. van den Doel, D. L. James, J. Lang, J. E. Lloyd, J. L. Richmond, and S. H. Yau. Scanning physical interaction behavior of 3D objects. In *Proceedings of the Annual Conference on Computer Graphics and Interactive Techniques*, pages 87–96, 2001.

- [87] X. D. Pang, H. Z. Tan, and N. I. Durlach. Manual discrimination of force using active finger motion. *Perception and Psychophysics*, 49(6):531–540, 1991.
- [88] Reachin Technology. Reachin display. <http://www.reachin.se/>.
- [89] P. Rhiemora, K. Gajananan, P. Haddawy, S. Suebnukarn, M. N. Dailey, E. Supataratarn, and P. Shrestha. Haptic augmented reality dental trainer with automatic performance assessment. In *Proceeding of the International Conference on Intelligent User Interfaces*, pages 425–426, 2010.
- [90] S. Salcudean and T. Vlaar. On the emulation of stiff walls and static friction with a magnetically levitated input/output device. *Journal of Dynamic Systems, Measurement, and Control*, 119(1):127–132, 1997.
- [91] C. Sandor, S. Uchiyama, and H. Yamamoto. Visuo-haptic systems: Half-mirrors considered harmful. In *Proceedings of the World Haptics Conference*, pages 292–297, 2007.
- [92] C. Scharver, R. Evenhouse, A. Johnson, and J. Leigh. Designing cranial implants in a haptic augmented reality environment. *Communications of the ACM*, 47(8):32 – 38, 2004.
- [93] SenseGraphics. 3D-IW. <http://www.sensegraphics.se/>.
- [94] T. Sielhorst, T. Obst, R. Burgkart, R. Riener, and N. Navab. An augmented reality delivery simulator for medical training. In *Proceedings of the International Workshop on Augmented Environments for Medical Imaging*, pages 11–20, 2004.
- [95] M. W. Spong and M. Vidyasagar. *Robot Dynamics and Control*. John Wiley and Sons, 1989.

- [96] M. A. Srinivasan and R. H. LaMotte. Tactual discrimination of softness. *Journal of Neurophysiology*, 73(1):88–101, 1995.
- [97] J. Swevers, F. Al-Bender, C. G. Ganseman, and T. Prajogo. An integrated friction model structure with improved presliding behavior for accurate friction compensation. *IEEE Transactions on Automatic Control*, 45(4):675–686, 2000.
- [98] C. Systems. Cybergrasp.
- [99] H. Z. Tan, B. D. Adelstein, R. Traylor, M. Kocsis, and E. D. Hirleman. Discrimination of real and virtual high-definition textured surfaces. In *Proceedings of the International Symposium on Haptic Interfaces for Virtual Environment and Teleoperator Systems*, pages 3–9, 2006.
- [100] H. Z. Tan, N. I. Durlach, G. L. Beauregard, and M. A. Srinivasan. Manual discrimination of compliance using active pinch grasp: The roles of force and work cues. *Perception and Psychophysics*, 57(4):495–510, 1995.
- [101] J. R. Vallino and C. M. Brown. Haptics in augmented reality. In *Proceedings of the IEEE International Conference on Multimedia Computing and Systems*, pages 195–200, 1999.
- [102] V. Virsu, H. Oksanen-Hennah, A. Vedenpää, P. Jaatinen, and P. Lahti-Nuutila. Simultaneity learning in vision, audition, tactile sense and their cross-modal combinations. *Experimental Brain Research*, 186(4):525–537, 2008.
- [103] B. J. Winer, D. R. Brown, and K. M. Michels. *Statistical Principles in Experimental Design*. McGraw-Hill, 3rd ed. edition, 1991.

- [104] K. Worden, C. Wong, U. Parlitz, A. Hornstein, D. Engster, T. Tjahjowidodo, F. Al-Bender, D. Rizos, and S. Fassois. Identification of pre-sliding and sliding friction dynamics: Grey box and black-box models. *Mechanical Systems and Signal Processing*, 21:514–534, 2007.
- [105] T. Yamamoto, B. Vagvolgyi, K. Balaji, L. L. Whitcomb, and A. M. Okamura. Tissue property estimation and graphical display for teleoperated robot-assisted surgery. In *Proceedings of the IEEE International Conference on Robotics and Automation*, pages 3117–3123, 2009.
- [106] H.-Y. Yao, V. Hayward, and R. E. Ellis. A tactile magnification instrument for minimally invasive surgery. *Lecture Notes on Computer Science (MICCAI)*, 3217:89–96, 2004.
- [107] G. Ye, J. Corso, G. Hager, and A. Okamura. VisHap: Augmented reality combining haptics and vision. In *Proceedings of the IEEE International Conference on Systems, Man and Cybernetics*, pages 3425–3431, 2003.
- [108] J. G. Zeigler and N. B. Nichols. Optimum settings for automatic controllers. *Journal of Dynamic Systems, Measurement, and Control*, 115:220–222, 1993.
- [109] F. Zhou, H.-L. Duh, and M. Billinghurst. Trends in augmented reality tracking, interaction and display: A review of ten years of ISMAR. In *Proceedings of the IEEE/ACM International Symposium on Mixed and Augmented Reality*, pages 193–202, 2008.

감사의 글

저의 20대를 바쳤던 포항도 이제 저의 제 2의 고향이 되었습니다. 포항생활을 마치고 좀 더 넓은 곳으로 갈 수 있게 해 주신 고마운 분들을 일일이 열거하기에는 지면이 부족한 것 같습니다. 먼저, 지금의 저를 있게 해 주시고 저를 끝까지 믿어주신 최승문 교수님께 무한한 감사를 드립니다. 부족함이 많은 제자였기에 죄송스럽기만 합니다. 그리고 학문적, 인격적으로 스승의 본보기를 보여주셨던 김정현 교수님께도 감사의 말씀을 올립니다. 교수님의 열정을 항상 마음속에 간직하고 있겠습니다. 또한, 바쁜 시간을 내셔서 흔쾌히 논문 심사를 해 주신 유지환, 한준희, 이승용 교수님께 감사를 드립니다.

그 동안 많은 분들이 지금의 저를 만들어 주셨습니다. 우선, 지금까지 저의 정신적, 학문적 지주로써 앞으로도 올바른 선배의 길을 보여주실 성길이형에게 감사를 드립니다. 근 7년 동안의 대학원생활을 동고동락하면서 많은 도움을 준 종현이, 선배로써 많은 가르침을 주신 남규형, 진석이형, 재인이형, 상윤이형, 건이형, 태용이형, 보현이형, 형진누님께 감사의 말씀을 전합니다. 또한, 연구실에 생활하면서 항상 도움을 받기만 한 동기, 후배님들인 진욱이형, 광훈이형, 유진이, 용진이, 재영이, 재훈이, 채현이, 재봉이, 저도 이제 보답하겠습니다. 앞으로 선배를 뛰어넘을 우리 후배님들, 성훈, 인, 인욱, 갑종, 건혁, 종만, 명찬, 경표, 호진에게 큰 도움을 주지 못해 미안했다는 말을 전하고 싶고 앞으로 남은 대학원 생활 행운이 있길 기원합니다.

마지막으로, 항상 죄송스러운 부모님께 이 논문을 바칩니다. 항상 마음속으로만 생각하던 말을 이 기회에 해보고 싶습니다. 어머니, 아버지, 사랑합니다. 항상 마음속에 든든한 버팀목이었던 형과 형수님에게도 감사드립니다. 그리고 아직 성숙하지 못한 저를 계속 믿고 따라준 인생의 동반자 정민이에게 고맙고 사랑한다는 말을 전하고 싶습니다.

Curriculum Vitae

Name : Seokhee Jeon
Date of Birth : 1979. 05. 21
Present Address : 대구광역시 수성구 매호동 동서타운 102동 1001호

Education

1998–2002 : B.S. in Computer Science and Engineering, POSTECH
2003–2010 : Ph.D. in Computer Science and Engineering, POSTECH
Thesis Title :
햅틱 증강현실: 실제 물체의 강도 변경(Haptic Augmented Reality: Modulating Real Object Stiffness)
Advisor: Prof. Seungmoon Choi

Publications

International Journals

1. **Seokhee Jeon** and Seungmoon Choi, "Haptic Augmented Reality: Taxonomy and Example of Stiffness Modulation," *Presence: Teleoperators and Virtual Environments*, vol. 18, no. 5, pp. 387-408, 2009.
2. **Seokhee Jeon**, Jane Hwang, Gerard J. Kim, and Mark Billinghurst, "Interaction with Large Ubiquitous Displays Using Camera-Equipped Mobile Phones," *Personal and Ubiquitous Computing*, vol. 12, no. 2, pp. 83-94, 2010.
3. **Seokhee Jeon**, Hyeongseop Shim, and Gerard J. Kim, "Viewpoint Usability for Desktop Augmented Reality," *International Journal of Virtual Reality*, vol. 5, no. 3, pp. 33-39, 2006.

International Conferences

1. **Seokhee Jeon** and Seungmoon Choi, "Stiffness Modulation for Haptic Augmented Reality: Extension to 3D Interaction," In *Proceedings of the IEEE Haptics Symposium*, pp. 273-280, 2010 (Recipient of Best Demo Award).

2. Gabjong Han, Jaebong Lee, In Lee, **Seokhee Jeon**, and Seungmoon Choi, "Effects of Kinesthetic Information on Memory Chunking in 2D Sequential Selection Task," In *Proceedings of the IEEE Haptics Symposium*, pp. 43-46, 2010 (Oral presentation; Extended abstract; Acceptance rate = 18.7%).
3. Gabjong Han, **Seokhee Jeon**, and Seungmoon Choi, "Improving Perceived Hardness of Haptic Rendering via Stiffness Shifting: An Initial Study," In *Proceedings of the ACM Symposium on Virtual Reality Software and Technology*, pp. 87-90, 2009 (acceptance rate = 23.7%).
4. **Seokhee Jeon** and Seungmoon Choi, "Modulating Real Object Stiffness for Haptic Augmented Reality," *Lecture Notes on Computer Science (EuroHaptics 2008)*, vol. 5024, pp. 609-618, 2008 (Acceptance rate = 36%).
5. **Seokhee Jeon** and Gerard J. Kim, "Providing a Wide Field of View for Effective Interaction in Desktop Tangible Augmented Reality," In *Proceedings of the IEEE Virtual Reality*, pp. 3-10, 2008 (Acceptance rate = 25%).
6. **Seokhee Jeon**, Gerard J. Kim, and Mark Billinghurst, "Interacting with a Tabletop Display Using a Camera Equipped Mobile Phone," *Lecture Notes on Computer Science (HCI International 2007)*, vol. 4551, pp. 336-343, 2007.
7. **Seokhee Jeon**, Jane Hwang and Gerard J. Kim, "Interaction Techniques in Large Display Environments using Hand-held Devices," In *Proceedings of the ACM Symposium on Virtual Reality Software and Technology*, pp. 100-103, 2006.

International Conferences; Nonreferred Papers/Posters/Demonstrations

1. **Seokhee Jeon** and Seungmoon Choi, "Modulating Real Object Stiffness for Haptic Augmented Reality," In *DVD Proceedings of the IEEE Virtual Reality*, 2010 (Demonstration).
2. **Seokhee Jeon** and Seungmoon Choi, "Haptic Augmented Reality: Modulation of Real Object Stiffness," In *DVD Proceedings of World Haptics Conference*, pp. 384-385, 2009 (Demonstration).
3. **Seokhee Jeon** and Gerard J. Kim, "Mosaicing a Wide Geometric Field of View for Effective Interaction in Augmented Reality," In *Proceedings of the IEEE and ACM International Symposium on Mixed and Augmented Reality*, pp. 1-2, 2007 (Poster).
4. Yongjin Kim, Jaehoon Jung, **Seokhee Jeon**, Sangyoon Lee, and Gerard J. Kim, "Telepresence Racing Game," In *proceedings of the ACM SIGCHI International Conference on Advances in Computer Entertainment Technology*, 2005 (Demonstration).
5. Yongjin Kim, Jaehoon Jung, **Seokhee Jeon**, Sangyoon Lee, and Gerard J. Kim, "Telepresence meets Racing Games," In *proceedings of the ACM SIGCHI International Conference on Advances in Computer Entertainment Technology*, 2005 (Poster).

International Publications in Preparation

1. **Seokhee Jeon**, Benjamin Knoerlein, Matthias Harders, and Seungmoon Choi, "Haptic Simulation of Breast Cancer Palpation: A Case Study of Haptic Aug-

mented Reality,” In *Proceedings of the IEEE and ACM International Symposium on Mixed and Augmented Reality*, 2010, submitted.

2. **Seokhee Jeon**, Benjamin Knoerlein, Matthias Harders, and Seungmoon Choi, “Haptic Simulation of Breast Cancer Palpation: A Case Study of Haptic Augmented Reality,” *Transactions on Haptics*, 2010, in preparation.
3. **Seokhee Jeon** and Seungmoon Choi, “Stiffness Modulation for Haptic Augmented Reality: Extension to 3D Interaction,” *Presence: Teleoperators and Virtual Environments*, 2010, in preparation.

Domestic Journals

1. Sangki Kim, Gunhyuk Park, **Seokhee Jeon**, Sunghoon Yim, Gabjong Han, Seungmoon Choi, and Seungjin Choi, “HMM-based Motion Recognition with 3-D Acceleration Signal,” *Journal of th KIISE: Computing Practices and Letters*, vol. 15, no. 3, pp. 216-220, 2009.
2. Yongsung Park, Jungtae Moon, **Seokhee Jeon**, and Sung H. Han, “Usability Evaluation of Button Selection Aids for PDAs,” *Journal of the Ergonomics Society of Korea*, vol. 24, no. 3, pp. 1-10, 2005.

Domestic Conferences

1. Sangki Kim, Gunhyuk Park, **Seokhee Jeon**, Sunghoon Yim, Gabjong Han, Seungmoon Choi, and Seungjin Choi, “HMM-based Motion Recognition with 3-D Acceleration Signal,” In *Proceedings of the KIISE Fall Conference*, pp. 69-70, 2008 (Winner of the best paper award).

2. **Seokhee Jeon**, Sangki Kim, Gunhyuk Park, Gabjong Han, Sungkil Lee, Seungmoon Choi, Seungjin Choi, and Hongjun Eoh, "Motion-Recognizing Remote Controller with Tactile Feedback," In *Proceedings of Human Computer Interaction Korea*, pp. 1-6, 2008 (a final candidate for the best paper award).
3. **Seokhee Jeon** and Gerard J. Kim, "Teaching Molecular Geometry with Immersion," In *Proceedings of Human Computer Interaction Korea*, pp. 32-37, 2007 (a final candidate for the best paper award).
4. Yongsung Park, Jungtae Moon, **Seokhee Jeon**, and Sung H. Han, "Design and Evaluation of Supportive Button Selection Methods on PDA," In *Proceedings of Human Computer Interaction Korea*, 2004.

Intellectual Properties

1. 최승문, 어홍준, 김상기, 정석주, 최승진, 전석희, "적외선 위치추적과 가속도 추적을 결합한 무선 게임 제어장치와, 게임 서버 및 사용자 동작 인식 방법", 10-2007-0140535, 2007.12.28. (출원중).
2. 조선영, 어홍준, 김상기, 박건혁, 전석희, 임성훈, 한갑종, 최승문, 최승진, "동작 인식 방법 및 장치", 10-2008-0130066, 2008.12.19. (출원중).
3. 최승문, 전석희, "햅틱 증강현실 제공 장치 및 방법", 10-2009-0011851, 2009.02.13. (출원중).
4. Seungmoon Choi and **Seokhee Jeon**, "Apparatus and Method for Providing Haptic Augmented Reality," US 12/394,032, 2009.02.26. (US patent applied).